SINGLE- AND TWO-QUBIT OPERATIONS ON AN ATOMIC QUBIT ARRAY

by

Kara Marie Maller

A dissertation submitted in partial fulfillment of
the requirements for the degree of

Doctor of Philosophy

(Physics)

at the

UNIVERSITY OF WISCONSIN–MADISON

2015

Date of final oral examination: April 8, 2015

The dissertation is approved by the following members of the Final Oral Committee:

Mark Saffman, Professor, Physics

Susan Coppersmith, Professor, Physics

Robert McDermott, Professor, Physics

Thad Walker, Professor, Physics

Randall Goldsmith, Assistant Professor, Chemistry

To my parents.

ACKNOWLEDGMENTS

I could have never completed my dissertation without the guidance and support of my research advisor, colleagues, and friends. First and foremost, I would like to express my sincere gratitude to my advisor Prof. Mark Saffman for the continuous support during my PhD and for giving me the opportunity to learn and do research in such as exciting field which will open so many doors for me in the future.

The AQuA experiment was built by a team of hard working, dedicated graduate students and post doctoral researchers who must be acknowledged. As a young graduate student I worked closely with senior graduate student Siyuan Zhang and post doctoral researchers Gang Li, Michal Piotrowicz, and Vladyslav Ivanov in setting up the beginning stages of the AQuA experiment. I would like to give special thanks to Larry Isenhower who I worked very closely with throughout the past five years and who has taught me so much about what it means to be an experimental physicist. Also, special thanks to Martin Lichtman for writing the control software without which there would be no data, Tian Xia for taking the Randomized Benchmarking data and Alex Carr for his theoretical contributions. Although he did not work on AQuA directly, Jonathan Pritchard contributed to many insightful conversations and helped me immensely by reading the editing my thesis.

Finally I want to acknowledge by family and friends for their unconditional support.

DISCARD THIS PAGE

TABLE OF CONTENTS

Page

APPENDICES

DISCARD THIS PAGE

LIST OF FIGURES

Figure Page

Figure Page

Figure Page

Appendix
Figure

ABSTRACT

In this thesis I describe the experimental progress towards the construction of an atomic qubit array. 49 single atom qubits are trapped in a 7×7 array which is then used in quantum logic experiments. I will describe how the atoms are loaded, initialized, measured and used to perform single- and two-qubit operations. We achieve parallel single qubit operations with an average fidelity of 0.9983(14) and single qubit operations on a single site with fidelity equal to 0.9923(7). Interactions between atoms excited to Rydberg states are used for two-qubit operations and two qubit entanglement. We achieve a two atom entanglement fidelity just above threshold and discuss in detail some factors limiting our two-qubit gates.

Chapter 1

Introduction

The rich field of quantum information science has rapidly progressed in the last 25 years. This fact is largely due to the discovery of Shor's algorithm for factoring large numbers in 1994 [3]. Shor's algorithm is just one example of how a quantum computer can outperform a classical supercomputer. Such algorithms along with the discovery of quantum error correction in 1996 [4–6] led to a flurry of proposals for physical implementations many of which are being pursued by experimentalists across the world today.

When discussing the physical implementation of quantum computers, many reference the DiVincenzo criteria [7]. These criteria outline the basic elements a physical system needs to be a viable candidate for quantum computing. The five criteria are:

1. A scalable physical system with well characterized qubits
2. The ability to reliably initialize the state of the qubits
3. Long coherence times, relative to gate operation times
4. A"universal" set of quantum gates
5. State specific qubit measurement

A partial list of physical implementations include trapped ions [8], superconductors [9], semiconductor quantum dots [10], photons [11] and, of course, neutral atoms.

1.1 Neutral atom quantum computers

Neutral atoms are an attractive candidate for quantum computing. The same properties that make atoms good frequency standards and clocks, the long-lived hyperfine states that are robust against decoherence, can be exploited for quantum information processing purposes. Unlike trapped ion systems, a leading candidate in the quantum computing race, the scaling of atomic systems is more straightforward. Optical lattices formed by interfering laser beams are commonly used in atomic physics labs to trap thousands of atoms. When combined with a Bose-Einstein condensate a Mott-insulator regime can be met where the same number of atoms is deterministically loaded across hundreds of sites in a lattice[12]. More recently site-resolved single atom detection has been achieved in such lattices [13].

Unlike two ground state ions who experience a strong Coulomb coupling, ground state neutral atoms couple via the magnetic dipole-dipole interaction which is negligible at the several micron separation needed for individual qubit addressing. Two qubit coupling needed for entanglement can be realized in several ways in neutral atom systems. Proposals for such include short-range electric dipole interactions [14], cold controlled ground state collisions [15], coupling of atoms to photons [16], magnetic dipole-dipole interactions [17], spatially delocalizing qubits [18] and Rydberg mediated interactions [19]. The attractive feature of the latter protocol, which is the approach taken in this thesis, is that at no time are interatomic forces experienced by the atoms. The atoms do not need to be moved around in order to interact and this protocol can be done on μs time scales. Also the interaction is not restricted to nearest neighbor.

1.1.1 The Atomic Qubit Array

The aim of the Atomic Qubit Array (AQuA) is to build an array of neutral atoms qubits. To meet the first of the DiVincenzo criteria, AQuA uses an array of single cesium atoms. The atoms are first laser cooled then loaded into optical dipole traps. The qubit is encoded in the clock states of the hyperfine ground state. We define $|0\rangle = |6s_{1/2}, F = 3, m_f = 0\rangle$ and $|1\rangle = |6s_{1/2}, F = 4, m_f = 0\rangle$. Most of the work presented in this thesis was done with a 49 site array which was scaled up from an original 6 site array. Scaling the array further amounts to adding more traps which is currently limited by the amount of laser power available. The atom cooling and trapping set-up is the subject of Chapter 2 and 3.

Qubit initialization, criterion 2, is achieved using well developed optical pumping techniques [20] and is discussed in Chapter 3. Ground state neutral atoms are known to have long coherence times. Coherence times as long as 58 s have been observed in magnetically trapped atomic ensembles [21]. Our single atom qubits typically have coherence times around 5-10 ms while quantum gates are executed in a few μs for the 2 qubit gate and 50 μs for the single qubit gates thus fulfilling criterion 3.

Quantum computers are, of course, meant to run quantum algorithms. Quantum algorithms are typically specified as a series of unitary transformations acting on a small subset of qubits. A set of gates is universal if any operation acting on any number of qubits can be constructed using that set of gates. For example, in classical computing NOT and AND form a universal set of gates. In order to meet criterion 4, our universal set of quantum gates is composed of the set of all single qubit gates and the two qubit controlled NOT (CNOT) gate. Single qubit gates are simply performed by coherently transferring the population between the two hyperfine states which is the subject of Chapter 4. To implement a CNOT gate we need a way to deterministically control interactions between two qubits. We do this using the Rydberg blockade protocol [19]. Demonstration of the CNOT gate in the array of qubits is the main goal of this thesis and is discussed in great detail in Chapter 5 and 6.

Finally, criterion 5, state specific qubit readout is necessary for knowing the result of a computation. The qubits are read out by collecting fluorescence at the end of an experiment sequence. To readout a specific state a single beam that is resonant with only one of the hyperfine states is turned on which ejects the atoms in that state from the trap. The absence or presence of an atom upon readout then signifies that the atom was in a particular state. The method is destructive and means the traps need to be reloaded every experiment cycle.

1.2 The Rydberg blockade quantum gate

In 2000 the concept of using the Rydberg blockade to perform a 2 qubit gate for qubits separated by more than 1 μm was proposed [19]. The excitation of one atom into a Rydberg excited state, a state with large principle quantum number n, shifts the energy of the Rydberg state of a nearby atom. If the shift is large enough, the excitation of the nearby atom into the Rydberg state is suppressed or blockaded.

The effectiveness of this process depends on the interactions between the two atoms in their various states. As mentioned above, two ground state atoms that are held in neighboring dipole traps separated by several microns interact dominantly through the magnetic dipole-dipole interaction which is roughly $\sim 10^{-5}$ Hz [22] at 10 μm. This interaction is negligible.

The interaction between two atoms excited to Rydberg states approaches the resonant dipole-dipole limit

$$V_{rr} = \frac{(n^2 e a_0)^2}{R^3} \sim 100\text{MHz} \tag{1.1}$$

for $R = 10$ μm and $n \sim 65$ [22]. This value is much larger than the natural line width of typical Rydberg states and is much larger than the typical MHz Rabi rates used to drive the transitions. This means if one atom is excited into the Rydberg state, the corresponding Rydberg state of the neighboring atom will be highly off resonant. Through excitation to the Rydberg state of just one of the atoms in a pair, we can turn on an interaction that is 13 orders of magnitude stronger than the interaction between two ground state atoms.

This Blockade mechanism can be used to implement a controlled-phase gate which can be used to create a CNOT gate and entanglement. Labeling one atom as the ‘control’ and the other as the ‘target’, the control atom is excited to the Rydberg level, $|r\rangle$, via a π-pulse resonant with the $|1\rangle$ to $|r\rangle$ transition. This is followed by a 2π Rydberg pulse on the target atom resonant with $|1\rangle$ to $|r\rangle$. Upon completion of the 2π-pulse, the target atom picks up a π phase shift unless the control atom started in $|1\rangle$ and thus was excited to the Rydberg state. In this case the Rydberg excitation of the target atom is blockaded and its phase remains unchanged. Then a second π-pulse is applied to the control atom, completing its rotation back to the ground state and picking up a phase shift of π.

To see how this is a controlled phase gate consider the two-atom computational basis states, $|ct\rangle$, individually:

$|00\rangle \rightarrow |00\rangle$ Both atoms will be off-resonant with the Rydberg pulses so no excitation occurs; no phase is accumulated.

$|01\rangle \rightarrow -|01\rangle$ The control is off-resonant with the Rydberg pulses so the target can complete a 2π rotation picking up a π phase shift.

$|10\rangle \rightarrow -|10\rangle$ The control completes a 2π picking up a π phase shift while target is off-resonant with the Rydberg pulses.

$|11\rangle \rightarrow -|11\rangle$ The control completes a 2π picking up a π phase and while in the Rydberg state blockades the excitation of the target.

This results in a controlled phase gate

$$C_z = \begin{pmatrix} 1 & 0 & 0 & 0 \\ 0 & -1 & 0 & 0 \\ 0 & 0 & -1 & 0 \\ 0 & 0 & 0 & -1 \end{pmatrix}. \tag{1.2}$$

When the controlled phase gate is sandwiched in between two ground state $\pi/2$ rotations the operation becomes a CNOT gate. This gate can in turn be used to make the two qubit entangled Bell states. In reality, the excitation beam needed for the Rydberg excitation induce additional phase shifts. A detailed analysis of this and its consequences for creating CNOT and Bell states is the subject of Chapter 6.

Much experimental progress has been made exploring this avenue of neutral atom quantum computing. Coherent excitation between ground and Rydberg states of single atoms was first demonstrated in 2008 [23]. Blockade between two single atoms was then demonstrated in 2009 [24, 25]. Finally, two atom entanglement was demonstrated in 2010 [26–28]. More recently two atom entanglement using a Rydberg-dressed ground-state Blockade mechanism was demonstrated [29].

Chapter 2

Experimental Set-up

The main goal of the Atomic Qubit Array (AQuA) experiment is to develop a system capable of performing quantum logic on individually addressable single atoms. As outlined in Chapter 1 the DiVincenzo criteria outlines the basic elements a physical system needs in order to be useful in the context of quantum computing [7]. The five criteria are

1. A scalable physical system with well characterized qubits
2. The ability to reliably initialize the state of the qubits
3. Long coherence times, relative to gate operation times
4. A “universal” set of quantum gates
5. State specific qubit measurement

The aim of this chapter is to describe the experimental apparatus we have built to fulfill these requirements. The experimental apparatus is shown schematically in Fig. 2.1. A hexagonal glass vacuum chamber is at the heart of the experiment. It is here that we load single atoms into an array of dipole traps and use the trapped atoms as quantum bits. We manipulate the qubits using microwaves for global rotations or tightly focused laser beams for single site rotations. We can then readout the state of the atom by collecting fluorescence with the same high numerical aperture lens that is used to tightly focus the trap and excitation beams.

This chapter will explain each of the individual parts of Fig. 2.1. In section 2.1 I will introduce the hexagonal cell and describe the preparation of atoms in the cell to form a cold, dense atomic cloud. This source of cold atoms is needed to load the dipole trap array, the subject of section 2.2.

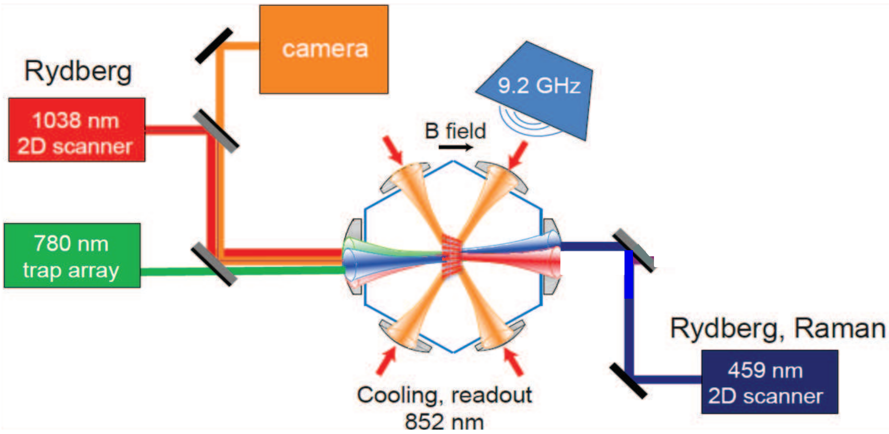

Figure 2.1: Schematic of the AQuA experiment

Once loaded into the array, we have established a scalable physical system of well characterized qubits thus fulfilling the first requirement. The qubit itself is encoded in the clock states of the hyperfine ground state. We define $|0\rangle = |f = 3, m_f = 0\rangle$ and $|1\rangle = |f = 4, m_f = 0\rangle$. The magnetic-field insensitive, $m_f = 0$, Zeeman levels of the long-lived ground state can have very long coherence times if further cooled in the dipole traps fulfilling the third requirement. Discussion of this will be saved for Chapter 4. In section 2.3 I will describe how we image the atoms once they are trapped. In section 2.4 I will describe how we satisfy the second and fifth requirement with our optical pumping and state readout set up. The next goal is qubit manipulation in order to perform a universal set of quantum gates, requirement four. Single qubit operations are performed using the microwave horn for global operations or a tightly focused beams for single site operations. For two qubit gates, long range Rydberg interactions are accessed via two photon transitions. This will be discussed in great detail in the remaining chapters of this thesis. In section 2.5 I will describe the 2D beam scanners needed for aligning to specific qubit sites in the array. The 1038 nm 2D scanner and the 459 nm 2D scanner shown in Fig. 2.1 are used for single qubit and two qubit operations.

2.1 2D/3D Magneto-Optical Trap

As the first step of our qubit experiments, we must load single atoms into an array of dipole traps. The atoms must be sufficiently colder than the depth of the traps for stable and reliable trap loading. Standard laser cooling and magneto-optical trapping (MOT) techniques are used to achieve dense clouds of atom with temperatures around 50 μK or colder suitable for loading into our traps. These techniques were developed in the late 80's [30–33] and are regularly used in atomic physics experiments. There are many good text books and review articles on the theory of laser cooling and trapping [34–36].

The two dimensional array of optical dipole traps are loaded from a three-dimensional magneto-optical trap (MOT). Often, MOTs are loaded from the hot background vapor in a vacuum cell. We require this background to be as low as possible as our imaging techniques described in section 2.3 involve turning on the MOT beams and collecting the fluorescence from the trapped atoms. If this background is to high the single atom signal will not be resolvable above the background. These hot background atoms will also limit the trap lifetime by colliding with the atoms in the trap [37]. However, a low cesium background pressure leads to a long MOT loading time, reducing the data rate. To get the best of both worlds we use a double cell, differentially pumped vacuum system[1]. A 2D-MOT [38] loaded from a hot vapor in the lower chamber creates a high flux beam of cold atoms that is used for loading the 3D-MOT in an upper chamber. A SolidWorks drawing of the cell is found in Fig. 2.2. The bottom half is a square glass cell which houses the 2D-MOT. In this cell a cesium dispenser which is run at a constant 3A creates the hot vapor from which the 2D-MOT is loaded. The 3D-MOT is formed in a hexagonal glass cell. A 750 μm pinhole separates the lower square cell from the vacuum pump which is connected between the two cells. The hexagonal cell is composed of 7.3 mm thick Pyrex windows, and has an internal window to window width of 20 mm. The geometry of the double cell system means that there is no optical axis on the bottom window of the top cell aside from the 750 μm pinhole. Because of this a mirror is placed inside of the bottom of the hexagonal cell 1.5 mm right from center. The mirror is used to create the vertical cooling beam for the 3D-MOT, as seen in Fig. 2.2.

---

[1] custom ColdQuanta vacuum chamber

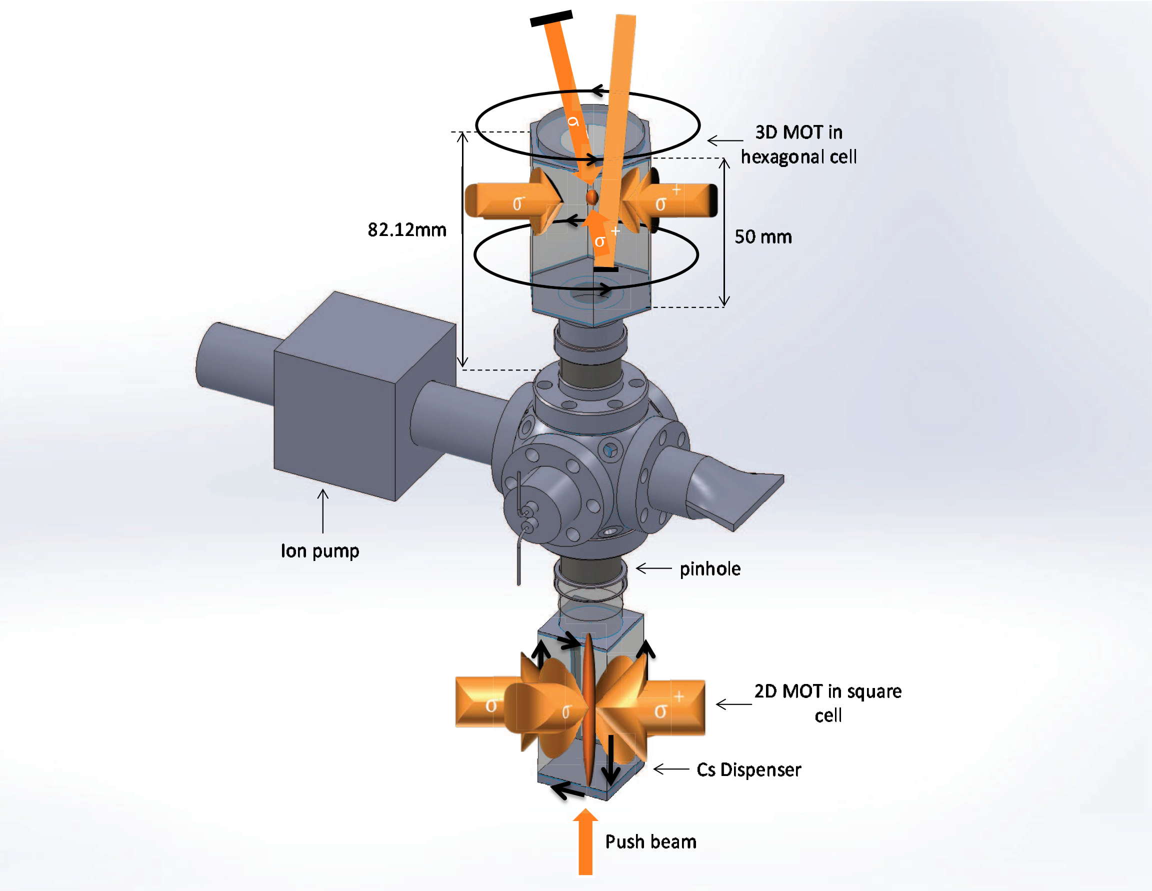

Figure 2.2: Diagram of 2D/3D double MOT set-up

The 2D-MOT is created using two pairs of counter-propagating, circularly polarized, elliptical beams with a 4×6 mm $1/e^2$ radius and 5 mW of 852 nm power in each beam. The two pairs of beams are perpendicular to each other and to the atomic beam axis defined by the vertical line of zero magnetic field. The 20 G/cm magnetic field gradient is produced by two pairs of 84 mm × 48 mm rectangular anti-Helmholtz coils separated by 38 mm. A push beam is aligned along the atomic beam axis and through the aperture which connects the lower square cell to the upper hexagonal cell. The push beam has a waist of 5 mm with 3 mW of power.

The 3D-MOT is formed using three pairs of circularly polarized, counter-propagating beams, with a quadrapole magnetic field that has a gradient of 20 G/cm in the vertical direction. The quadrapole field is formed by a pair of anti-Helmholtz coils. The coils have a diameter of 60 mm and are separated by 60 mm. They are composed of 100 turns of 22 gauge copper wire giving a field strength of 17.8 G/cm/A. The 3D-printed MOT coil holder also houses 4 pairs of shim coils- one for each window pair of the hexagon and one for the vertical direction. The shims are used to null out stray magnetic fields. One pair will also be used as the bias field discussed in section 2.4. Each of the horizontal coil pairs have a diameter of 37.4 mm with a 76.2 mm spacing giving a field strength of 0.6 G/A for 10 turns of the 22 gauge copper wire. The vertical coil pair have a 61.7 mm diameter and 46.4 mm spacing giving 1.8 G/A with 10 turns of the 22 gauge copper wire.

The horizontal 3D-MOT beams each have a waist of 2.5 mm and the vertical pair has a waist of 1.54 mm with a total of 5 mW balanced between the beams to give equal intensity at the atoms. Due to the geometry of the hexagonal cell, the horizontal beams cross at a 60 degree angle. This 2D-MOT to 3D-MOT set-up allows for a MOT loading time less than 500 ms in a very good vacuum less than 10^{-9} torr. This ensures long trap lifetimes on the order of 20 s without sacrificing the data rate. Details of these timings are explained in Chapter 3. In typical experiments we load the MOT for 300 ms and our overall data rate is around 2 Hz.

For laser cooling and trapping in cesium, 852 nm light resonant with the $6s_{1/2}, f = 4 \rightarrow 6p_{3/2}, f' = 5$ cycling transition is needed. Along with this, light resonant with $6s_{1/2}, f = 3 \rightarrow 6p_{3/2}, f' = 4$ is necessary to "repump" the atoms that are depumped into $f = 3$ back into the $f = 4$ so they can interact with the cooling light. A commercial 852 nm laser[2] is used for the 3D-MOT cooling beams. The 4×4 inch temperature-controlled laser module is mechanically robust and includes a distributed Bragg reflector (DBR) laser diode. The output of the laser module is sent to a spectroscopy module[3] which houses a temperature-stabilized cell filled with cesium vapor used for saturated absorption spectroscopy [39]. Using the spectroscopy signal the laser is locked to the $f = 4 \rightarrow f' = 3$ and $f = 4 \rightarrow f' = 5$ cross-over line which is detuned -226 MHz from the $f = 4 \rightarrow f' = 5$ resonance. After the spectroscopy module, part of this light gets picked off for the blow away beam which will be discussed in section 2.4. The rest is sent through a tapered amplifier (TA)[4] to amplify the light to 200 mW. An acousto-optical modulator (AOM) driven by 108 MHz is set up in a double pass configuration to shift the frequency closer to the cycling $f = 4 \rightarrow f' = 5$ transition, resulting in a detuning of -10 MHz or in terms of natural

---

[2] Vescent Photonics D2-100-DBR

[3] Vescent Photonics D2-110

[4] m2k-TA-0850-2000-CM

line width of the $6p_{3/2}$ state, -1.9 Γ. Here the detuning is defined to be the laser frequency, ω_L, minus the atomic resonant frequency, ω_A. The AOM is controlled by a Direct Digital Synthesis (DDS) board which allows us to easily switch between different frequency and amplitude settings during experiments. 1 mW of "repumper" is added to the beams. A second 852 nm laser[5] is used for the repumper light and is locked to the $f = 3 \rightarrow f' = 2$ and $f = 3 \rightarrow f' = 3$ cross-over line. The repumper light is split into two paths. Each path is sent through a single-pass AOM driven by 278.5 MHz which shifts the light to be resonant with the $f = 3 \rightarrow f' = 4$ transition. One of these AOMs is used for the 2D- and 3D-MOTs. The second will be used with the optical pumping described in section 2.4. The AOM for the MOT repumper is also controlled by a DDS board and can be easily switched on and off during experiments. A third 852 nm laser[6] is needed for the 2D-MOT beams. This laser is comprised of a Fabry-Perot laser diode and a grating. The grating is placed less than 1 cm from the diode at a fixed position. An asphere and anamorphic prism produce a circular beam inside the module which is sent to an external isolator before being sent to the spectroscopy module described above. The laser is locked to the D2 $f = 4 \rightarrow f' = 4$ and $f = 4 \rightarrow f' = 5$ cross-over line which is -125.5 MHz detuned from the $f = 4 \rightarrow f' = 5$ resonance. A double-pass AOM driven by 57.75 MHz shifts the frequency closer to the cycling $f = 4 \rightarrow f' = 5$ transition, resulting in a detuning of -10 MHz or -1.9 Γ. This AOM is driven by a voltage controlled oscillator (VCO) and remains fixed through out the experiment. 150 μW of repumper light is also added to the 2D-MOT beams. The repumper light is shared by both 2D- and 3D-MOT set-ups. The 2D-MOT is left on during the MOT loading phase of an experiment and is switched off using a mechanical piezo shutter. The 2D-MOT gradient field remains fixed.

All cooling and repumper light are shifted by their respective AOMs then coupled into optical fibers which are sent either directly or indirectly to the experiment. The 3D-MOT cooling and repumper light is first sent to a switch-yard where it is combined and coupled into three different fibers that are then sent to the experiment.

Exactly how we use this set up to load single atoms into the dipole traps is the subject of Chapter 3.

---

[5] Vescent Photonics D2-100-DBR

[6] Vescent Photonics D2-100-CECL

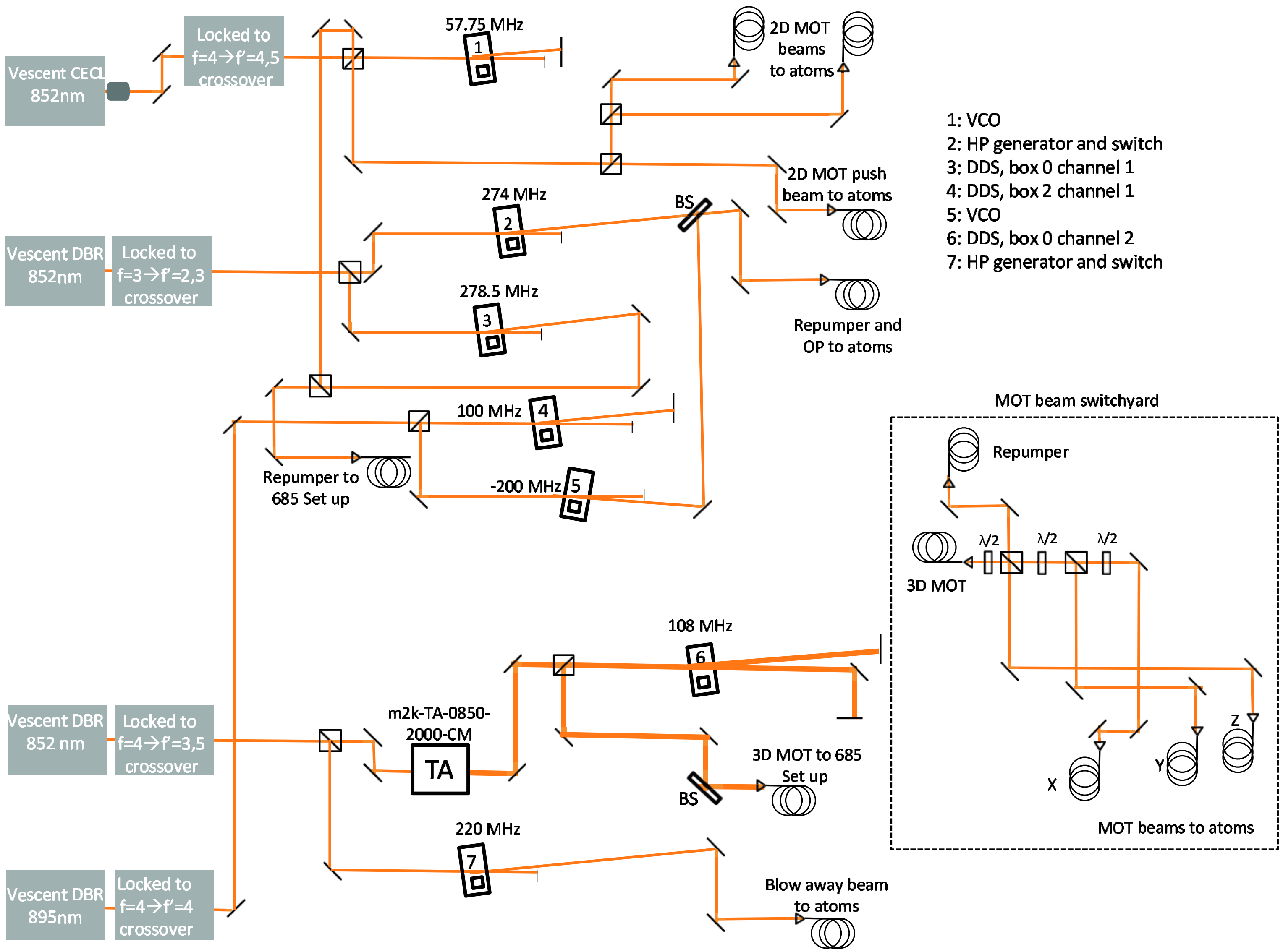

1: VCO
2: HP generator and switch
3: DDS, box 0 channel 1
4: DDS, box 2 channel 1
5: VCO
6: DDS, box 0 channel 2
7: HP generator and switch

Figure 2.3: Layout of the MOT and repumper lasers plus AOMs needed for cooling.

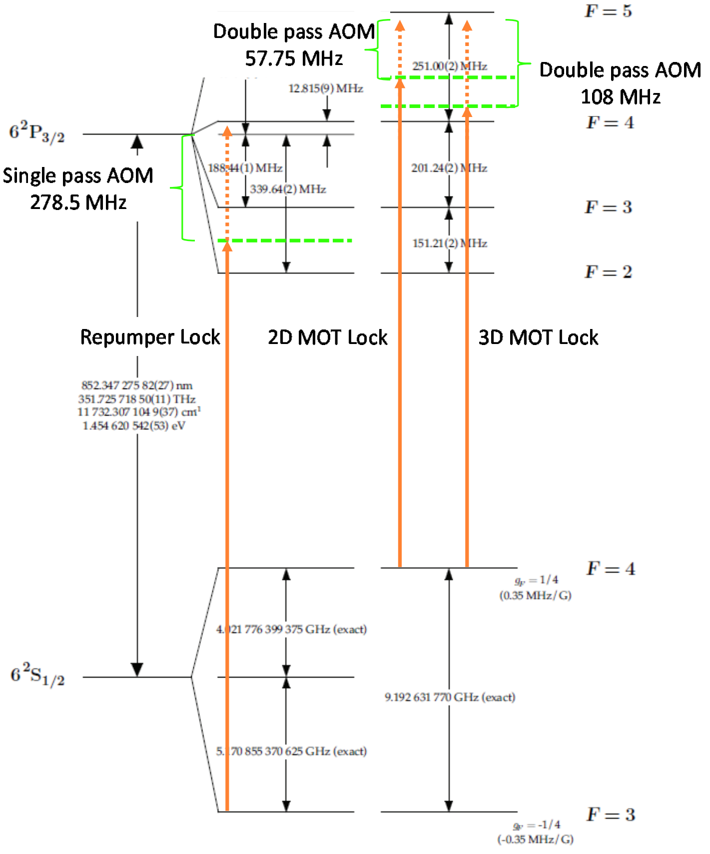

Figure 2.4: $6p_{3/2}$ laser locks plus AOM frequencies needed for laser cooling and repumping in cesium, diagram from [1].

2.2 Dipole traps

Advanced techniques for trapping charged and neutral particles have become routine in atomic physics experiments over the last couple of decades[34]. For charged particles (ions), the Coulomb interaction is routinely used for trapping in electric fields[40]. Neutral atoms, however, must be trapped using much weaker mechanisms than the Coulomb interaction and therefore must be laser-cooled before being trapped. Neutral atoms can be trapped by inducing an atomic dipole moment, by using magnetic fields, or with radiation pressure[36, 41]. Here we use the first method of inducing a dipole moment using far-detuned light.

The trapping potential due to a far off resonant laser field is given by $U_{\text{dip}} = -\frac{1}{4}\alpha|\mathcal{E}|^2$ where α is the polarizability and $\mathcal{E}$ is the electric field amplitude. The polarizability is calculated by accounting for all allowed transitions to excited states which for cesium is dominated by contributions from the first resonance lines. For large detunings this is approximately

$$U_{\rm dip} = \frac{\pi c^2 \Gamma}{2\omega_{\rm a}^3}(\frac{2}{\Delta_{3/2}} + \frac{1}{\Delta_{1/2}})I(\mathbf{r}). \tag{2.1}$$

Here c is the speed of light, $\omega_{\rm a}$ and Γ are the frequency and decay rate of the $6s_{1/2} - 6p_{3/2}$ transition, $\Delta_{3/2(1/2)}$ are the laser detunings from the $6p_{3/2(1/2)}$ states and $I(\mathbf{r})$ is the spatially varying intensity of the trapping field. The detuning is defined as $\Delta = \omega_{\rm dip} - \omega_{\rm a}$ so that if $\Delta < 0$ (red-detuned) the potential is lower where the intensity is higher and therefore the atom is attracted to the region of highest intensity. By engineering the intensity profile we can create arbitrary trapping geometries. The simplest example of this is tightly focused Gaussian beam whose peak intensity with power P and waist w is $I(0) = \frac{2P}{\pi w^2}$ [42].

When $\Delta > 0$ (blue-detuned), the potential increases with increasing intensity and therefore the light repels the atoms. In this case atoms are trapped at the intensity nulls. The high intensities needed for red-detuned traps lead to higher photon scattering rates and light shifts than compared to blue-detuned traps. In addition blue-detuned configurations allow for simultaneous trapping of both Rydberg excited states and ground states[43].

In the context of quantum computing experiments, we require our dipole trap array to have certain characteristics. First, the traps should be inherently scalable to a large number of sites in order to have a large number of qubits. The traps must be small enough to ensure sub-Poissonian single atom loading via light-assisted collisions [44, 45] but have a large enough spacing to have the ability to spatially resolve qubits for readout and single site addressing for qubit manipulation. The sites also need to be sufficiently spaced to make the Rydberg blockade effective, on the order of $\sim$10 μm.

Arrays of dipole traps can be created in a number of ways using microlenses [46], holographic elements [47], or diffractive optics [48]. Another common technique is to create an optical lattice by interfering Gaussian beams in three dimensions [49].

We have demonstrated single atom loading into two different types of projected Gaussian beam trap arrays[2]. The first is a 6 site, half incoherent array. The second a 49 site, fully incoherent array. The meaning of half incoherent and fully incoherence will be made clear in section 2.2.1.

The traps are created with 780 nm light which is blue-detuned for cesium. Atoms are trapped in the intensity nulls in between tightly focused Gaussian beams. Localization in the beam propagation direction is provided by the diffractive spreading of the beams. This approach is more desirable than the optical lattice approach for two reasons. First it is inherently two dimensional which means there is no crosstalk from neighboring planes. Second it does not rely on interference which means it is stable against trap position drifts due to optical phase fluctuations.

2.2.1 Projected Gaussian Beam Array

A single trap is created by weakly overlapping four Gaussian beams each with a waist, w_0, separated by a distance d as shown in Fig. 2.5. The separation to beam waist ratio, $s = d/w_0$, is used to characterize the trap. The phrase "weakly overlapping" is used when $d > w_0$ with $s \approx 2$. In this regime, the overlap of neighboring beams is significant while the overlap of beams at larger distances is negligible.

In the first type of array neighboring beams have orthogonal polarizations so their intensities add. Diagonal beams, separated by $\sqrt{2}d$, have the same polarization so their electric fields add and phase variations between these beams can lead to variations in the trap intensity at the center of each unit cell. This type of array is called "half-incoherent". To calculate the trap depth we need to calculate the intensities at the saddle point and at the trap center. At the saddle point, half way between two beams on the side of a unit cell, the intensity is approximately the sum of intensities from the two nearest beams

$$I_s^H = 2I_o e^{-2(d/2)^2/w_o^2} = 2I_o e^{-d^2/2w_o^2}, \tag{2.2}$$

where I_o is the single beam peak intensity. At the center of the trap, the intensity can be approximated by adding the electric fields of the two diagonal beams which share a polarization and adding the intensities of the two polarization pairs. The electric fields are summed assuming the diagonal beams are in phase and therefore constructively interfere. Then the center intensity is

$$I_c^H = 2I_o(2e^{-(d/\sqrt{2})^2/w_o^2})^2 = 8I_o e^{-d^2/w_o^2}. \tag{2.3}$$

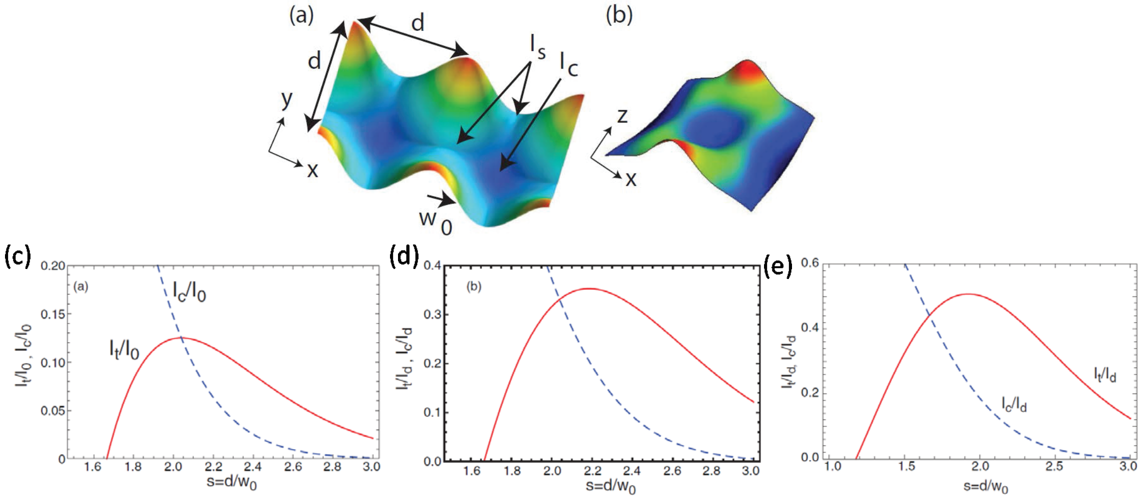

Figure 2.5: Intensity distribution of Gaussian beam array in the x-y (a) and x-z (b) planes. Beams propagate along the z-axis. (c-d) Normalized trapping depth and intensity at trap center versus normalized array period for half-incoherent array. Variation at constant peak intensity I_0 in (c), and variation at constant average intensity I_d in (d). (e)Normalized trapping depth and intensity at trap center versus normalized array period for full-incoherent array at constant average intensity I_d. [2]

The trap depth is then proportional to the difference of the center intensity and the saddle point intensity,

$$I_t^H = I_s^H - I_c^H = 2I_o e^{-d^2/2w_o^2}(1 - 4e^{-d^2/w_o^2}) = 2I_o e^{-s^2/2}(1 - 4e^{-s^2}). \tag{2.4}$$

There is a maximum trap depth when $s_0 = \sqrt{(2\ln 8)} \approx 2.04$. Setting $s = s_o$ we find $I_s^H = I_o/4$, $I_c^H = I_o/8$, $I_t^H = I_o/8$. For fixed optical power and fixed lattice period, d, the average intensity in a unit cell of area d^2 is $I_d^H = \frac{P}{d^2} = \frac{\pi I_0}{2s^2}$. The trap depth as a function of average intensity and waist ratio is

$$I_t = I_d \frac{4s^2 e^{-s^2/2}}{\pi}(1 - 4e^{-s^2/2}). \tag{2.5}$$

This reaches a maximum of $I_t^H/I_d^H = 0.35$ when $s = 2.19$.

We can derive the approximation of the potential at the trap centers which is used to find the effective spring constants of the traps [43]

$$\begin{aligned} \kappa_x &= \frac{32|U_d|}{\pi d^2} s^4 (s^2 - 2) e^{-s^2}, \\ \kappa_y &= \kappa_x, \\ \kappa_z &= \frac{32\lambda^2 |U_d|}{\pi^3 d^4} s^6 (s^2 - 1) e^{-s^2}, \end{aligned} \tag{2.6}$$

where $U_d = \frac{\alpha}{2\epsilon_0 c} I_d$ is the trapping potential which is proportional to the "trap depth intensity", I_d, and α is the atomic polarizability. λ is the trapping wavelength, equal to 780 nm here. The corresponding oscillation frequencies are then $\omega = \sqrt{\kappa / m_a}$ where m_a is the atomic mass. These are measured experimentally in Chapter 3.

The second type of array is designed such that a unit cell is created with four incoherent beams. We call this array "fully-incoherent". All four intensities can be summed together to calculate the saddle and center intensities

$$I_s^F = 2I_0 e^{-s^2/s}, \tag{2.7}$$

$$I_c^F = 4I_0 e^{-s^2}. \tag{2.8}$$

The center intensity is reduced by a factor of two as compared to the half-incoherent case. Since the saddle intensity is unchanged, the trap depth is increased

$$I_t^F = I_d^F \times \frac{4s^2 e^{-s^2/2}}{\pi} (1 - 2e^{-s^2/2}). \tag{2.9}$$

For the same average intensity, the fully-incoherent array has about 30% more trap depth than the half-incoherent. The spring constants can also be derived just as with the half-incoherent case

$$\begin{aligned} \kappa_x &= \frac{32|U_d|}{\pi d^2} s^4 (s^2 - 1) e^{-s^2}, \\ \kappa_y &= \kappa_x, \\ \kappa_z &= \frac{16\lambda^2 |U_d|}{\pi^3 d^4} s^8 e^{-s^2}. \end{aligned} \tag{2.10}$$

2.2.1.1 Implementation

To create the 6 site half-incoherent array, a single Gaussian beam is sent through a diffractive element to create four parallel Gaussian beams separated by d'. The beams are sent through two

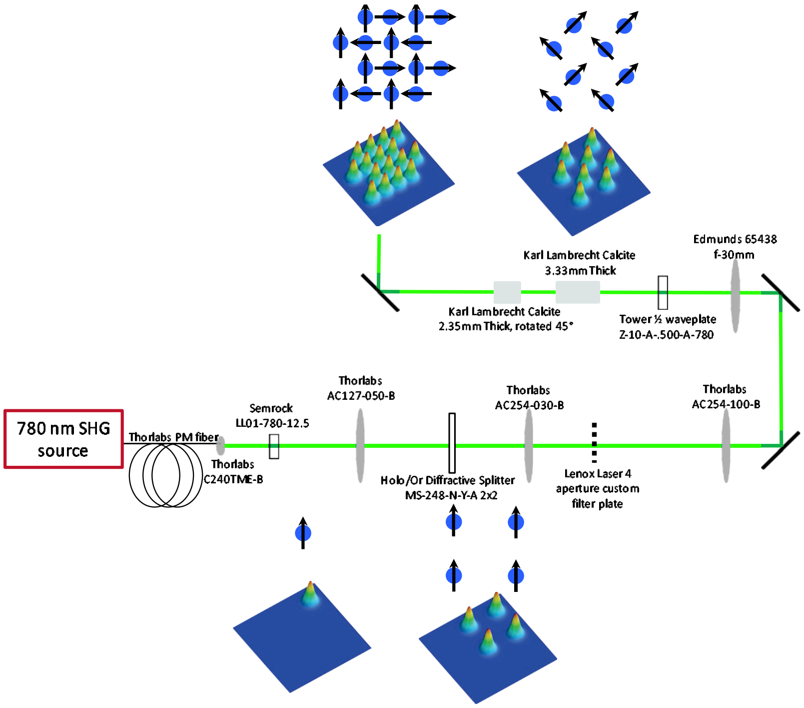

Figure 2.6: Optical set-up used to create the 6 site, half-incoherent array

calcite beam displacers which spatially separate orthogonal polarizations by a fixed amount specified by the thickness of the calcite. The first thicker calcite gives a lateral displacement of $d/\sqrt{2}$. The second thinner calcite is rotated 45 degrees with respect to the first and gives a displacement of $d'/2$. The result is an array of 16 Gaussian beams which can then be imaged onto the cesium MOT with a multi-element high numerical aperture lens. The imaged array is made up of beams with 1.8 μm waists and 3.8 μm spacing. The source of the 780 nm light in this case comes from a 1560 nm Distributed Feedback (DFB) laser[7] which seeds a 20 W 1560 nm fiber amplifier[8]. This light is sent through a 0.5 mm × 5 mm × 50 mm heated Periodically Poled Lithium Niobate (PPLN) crystal set up in a double pass configuration. The process of second harmonic generation (SHG)[50] produces light at 780 nm which is separated from the 1560 nm light via a dichroic. This technique converts 20 W of 1560 nm light into about 6 W of 780 nm light.

---

[7] Optilab DFB-B-20-P-1560

[8] IPG EAR-20K-C-LP-SF

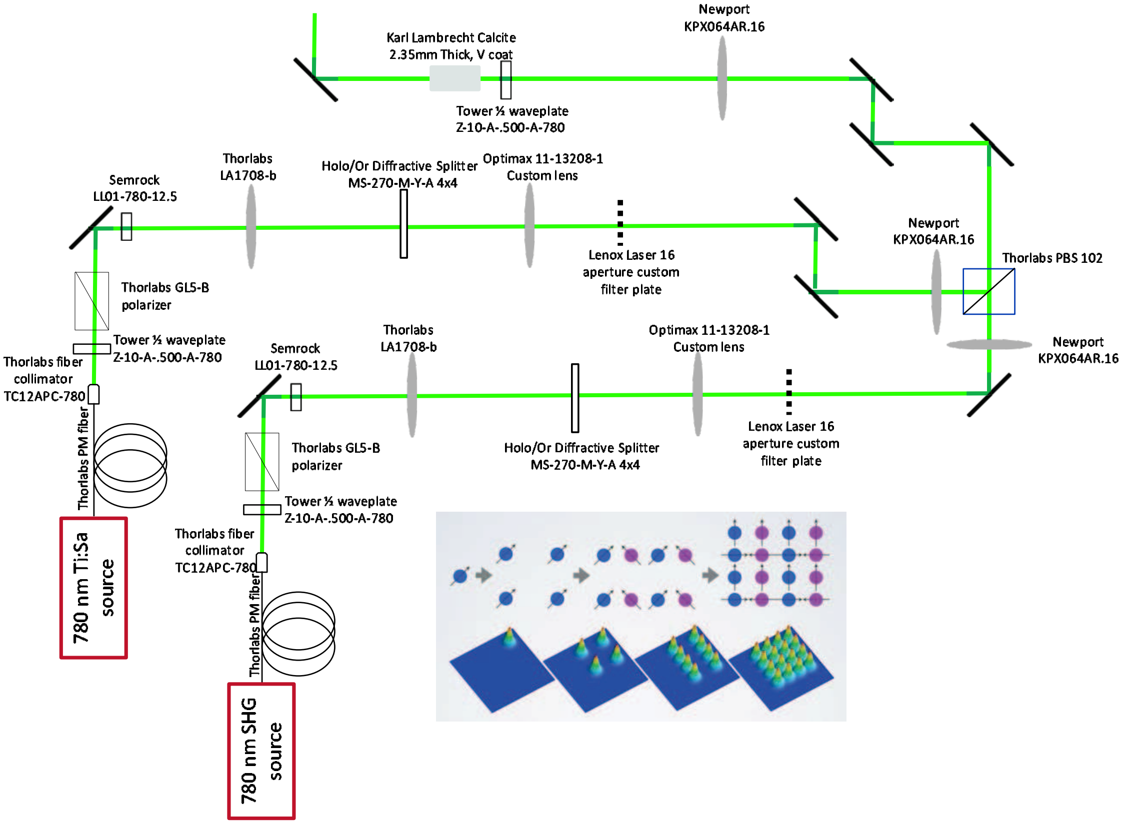

Figure 2.7: full incoherent array optical layout

Using this SHG 780 nm laser described above along with a Ti:Sapphire Laser[9] tuned to 780 nm, pumped by a 18 W 532 nm laser[10], a configuration similar to the half-incoherent array just described can be realized only every beam in a unit cell will either be from a different laser or have an orthogonal polarization thus creating a “fully-incoherent array”. As illustrated in Fig. 2.7 two different 780 nm sources are sent through two different diffractive elements each creating a 4×4 array of parallel Gaussian beams. These beams are combined on a polarizing beam splitter and then sent through a calcite which halves the spacing of the beams. The result is 64 spots with the same distance to beam waist ratios as the half-incoherent set-up. Table 2.1 summarizes the relevant

---

[9] M2 SolsTiS-PSX-F

[10] Coherent Verdi V18

Table 2.1: Parameters for half-incoherent and full-incoherent arrays

Wavelength, λ	780 nm
Beam periodicity, d	3.8 μm
Beam waist, w_0	1.81 μm
Cs scalar polarizability at λ, α_0^{cgs}	-240 $\times$ 10^{-24} cm^3
Total optical power,half-incoherent	1.5 W
Total optical power,full-incoherent	2.5 W
Calculated trap depth, half incoherent	830 μK
Calculated radial trap frequency, half-incoherent	$2\pi\times$39 kHz
Calculated axial trap frequency, half-incoherent	$2\pi\times$6.4 kHz
Trap depth, full-incoherent	570 μK
Radial trap frequency, full-incoherent	$2\pi\times$39 kHz
Axial trap frequency, full-incoherent	$2\pi\times$9.6 kHz

parameters used in our experiments for each of the arrays. The low 50% transmission is mostly due to the diffractive element which transmits about 70% of the light in the desired diffractive order.

2.3 Imaging System

After loading single atoms in the array of dipole traps we will need a way to image them. This means both spatially resolving each site which is separated by 3.8 μm and being able to distinguish with good fidelity the difference between 0 and 1 atoms. We image the atoms by turning on the MOT and repumper light with the gradient field off and collecting the resulting fluorescence. The MOT light is further detuned to -8 Γ and the power is decreased to about 100 μW per beam. These settings are similar to those used during polarization gradient cooling (PGC)[51] such that the light cools the atoms and many photons can be scattered without losing the atoms from the trap. The scattered photons are collected by a high numerical aperture lens and then imaged onto

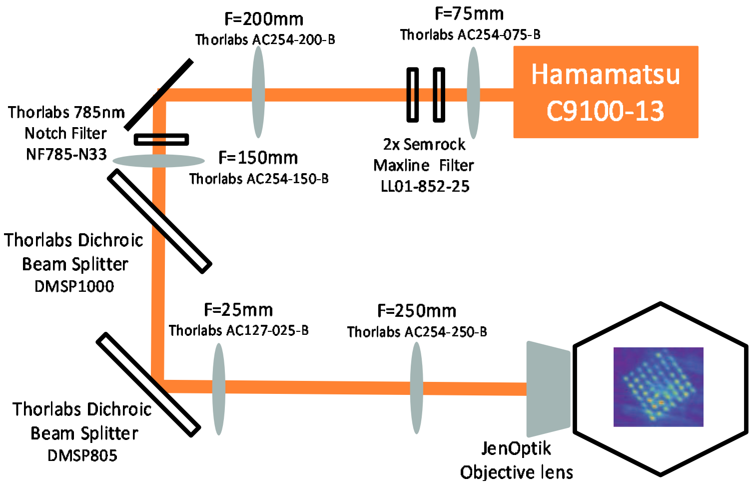

Figure 2.8: Imaging optics set up for imagining single atoms in the array. A series of dichroics and filters are needed to isolate the fluorescence light. The lenses shown result in an imaging magnification of 25.5 which gives an effective pixel size of 0.63 μm.

a EMCCD[11]. The detection efficiency must be large enough and the background small enough to distinguish the atom signal from the background.

The same lens used for focusing the trapping and excitation beams is used for collecting the fluorescence for single atom imaging, as depicted in Fig. 2.1. The 5 element custom JenOptik Objective lens is designed to be diffraction limited for 455, 685, 780, 852, 915 and 1038 nm and to have greater than 94 $\%$ transmission for these wavelengths. It has a numerical aperture of 0.4 and an effective focal length of 23.125 mm. An additional 5 lenses are used to image the fluorescence onto the EMCCD, as seen in Fig. 2.8. We are imaging the back scatter so the first two lenses in the imaging relay are shared by the 780 nm trap light. The 852 nm photons are separated from the 780 nm trapping light using a dichroic and from the 1038 nm Rydberg excitation beam by yet another dichroic. A series of 852 nm band pass filters and 780 nm notch filters are used to try to reduce the background scattering the camera sees. The relay of lenses results in an imaging magnification of 25.5 which gives an effective pixel size of about 0.63 μm. Given our 3.8 μm trap spacing this imaging should allow us to spatially resolve single sites.

---

[11] Hamamatsu C9100-13

We can calculate what we would expect this single atom signal to be given our system parameters which include readout beam intensities and detunings, exposure time, collection efficiency and measured background signals. A two-level atom interacting with a monochromatic field is described by the optical Bloch equations[1]. The scattering rate is given by

$$R_{\mathrm{sc}} = \frac{\Gamma}{2}\frac{I/I_{\mathrm{sat}}}{1 + I/I_{\mathrm{sat}} + (\frac{2\Delta}{\Gamma})^2}, \tag{2.11}$$

where we have introduced the saturation intensity and

$$\frac{I}{I_{\mathrm{sat}}} = 2(\frac{\Omega}{\Gamma})^2, \tag{2.12}$$

where Ω is the coupling between the ground and excited state. We must average over all of the couplings to the various sublevels, of which there are 27 for the $f = 4$ ground state. Then we have

$$\frac{I}{I_{\mathrm{sat}}} = \frac{2}{27\Gamma^2}\sum_{m_g,q} |\Omega_{4,m_g \to 5,m_g+q}|^2, \tag{2.13}$$

where m_g are the sublevels of the ground state, $m_e = m_g + q$ represent the excited state and q is equal to $(-1, 0, +1)$ for $(\sigma_-, \pi, \sigma_+)$ photon polarization. Values for these matrix elements are found in Ref. [1]. In general, I_{sat} depends on the polarization of the light which is seen in equation (2.13). For atom imaging we use a three-dimensional $\sigma_+ - \sigma_-$ configuration, just as with the MOT as described in section 2.1 but with the gradient field turned off. In this case we have an isotropic pump field where all three polarizations are equal and $I_{\mathrm{sat}} = 2.7$ mW/cm ^{2}. For a readout detuning of $\Delta = -8\Gamma$ and total beam saturation parameter of $I/I_{\mathrm{sat}} = 2.26$, this will give a scattering rate $R_{\mathrm{sc}} = 138000\mathrm{s}^{-1}$. These scattered photons are collected by the custom 5 element lens and must pass through multiple surfaces before reaching the EMCCD. The total fractional solid angle and estimated transmission efficiency of our imaging system is therefore 0.042 and 0.8, respectively. Finally, the quantum efficiency of our EMCCD at 852 nm is 0.7, resulting in a photon collection efficiency of about 2.4 $\%$. Therefore the detected scattering rate for a single atom is calculated to be 3200 s^{-1}. In 50 ms we can expect to detect 162 photons. This number must be greater than our background to be useful.

We can now predict how many counts to expect given the conversion factor for the EMCCD is 5.8 electrons/count. For single atom readout experiments, we have the analog gain set to 4 and the EM gain set to 191. We can calculate the expected output signal minus dark signal(background):

Expected Output Signal - Dark Signal=(detected photon number)×(analog gain)×(EM gain)×(quantum efficiency)/(conversion factor)=162×4×191×0.7/5.8=14916 counts

Each trapped atom is confined to a 3×3 pixel region. The average background pixel value was measured at 5457 counts. The signal we expect too see on the camera is then

Expected Output Signal=(Expected Output Signal - Dark Signal)+(average background pixel value)×(ROI area)=6.4×10^4 counts.

In Chapter 3 we will see that these calculations agree with experiment when we include the Stark shifts of the 780 nm trap light. When calculating the photon scattering rate, we used the free space detuning. In the experiments described in Chapter 3, we learn that the 780 nm light in the trap centers Stark shift the readout line by about 1 to 2 Γ, varying slightly from site to site. This variation in trap center will effectively change the readout detuning from site to site. Including the Stark shift variation, we can expect an output signal between 6.9×10^4 counts and 7.5×10^4 counts.

2.4 Optical Pumping set up

The second requirement needed for a quantum computer as stated by DiVincenzo [7] is the ability to initialize the quantum state. This is done in cold neutral atom systems by well developed optical pumping techniques [20]. We optically pump into the $|1\rangle = |f = 4, m = 0\rangle$ clock state. This is achieved by applying light linearly polarized in the direction of an applied 1.5 G bias field which is parallel to the trap axis. The light is resonant to the $f = 4 \rightarrow f' = 4$ D1 transition at 894 nm. Since the $|m_f = 0\rangle$ states are not coupled by the light all of the population will accumulate in $|f = 4, m = 0\rangle$ due to spontaneous emission from all of the other states. Repumper light at the $f = 3 \rightarrow f' = 4$ transition is also needed to eliminate $|f = 3\rangle$ populations. The optical pumping light and the repumping light are aligned to the same fiber which is aligned to the atoms vertically, through the top window with a beam waist of 200 μm at the atoms. A polarizing beam cube is placed just before the light enters the cell to clean up the polarization. The beam is carefully aligned to the 750 μm pinhole in the lower cell to minimize light scattering which would result in unwanted polarization and affect the pumping fidelity.

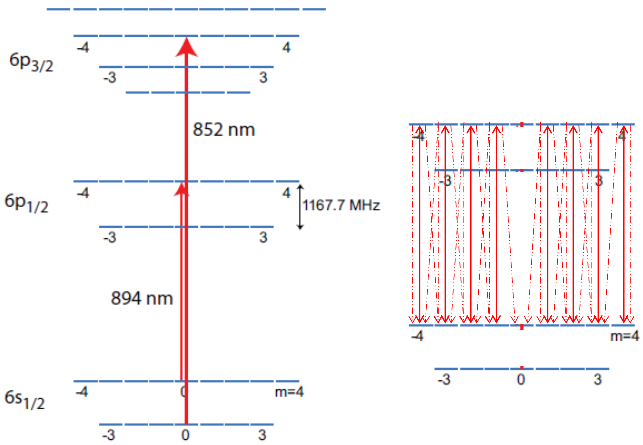

Figure 2.9: Level diagram showing the lasers needed for Optical pumping along with the optical pumping procedure. Dashed lines show population loss from the excited states due to spontaneous emission.

Shown in Fig. 2.3 with the cooling lasers, the optical pumping laser at a 894 nm[12] is locked to the $6s_{1/2}f = 4 \rightarrow 6p_{1/2}f' = 4$ transition. The light is sent through an AOM set up in the double pass configuration driven at 100 MHz then through another AOM set up in a single pass configuration and driven at 200 MHz. The -1^{st} order from this second AOM is combined on a 50/50 beam splitter with resonant repumper light and coupled into a fiber. The two AOMs are meant to cancel each other out such that the light is resonant with the f=4 → f'=4 transition. We need at least one AOM to act as a switch on the light as well as to shift the frequency by a small amount to compensate for Stark shifts in the traps. We need the second AOM to cancel out most of the shift from the first. Very little light is needed for optical pumping so the hits we take from having two AOMs plus the 50/50 beam splitter are not a problem. The 894 nm power seen by the atoms is around 500 nW.

Finally we use a state-dependent blow away beam for state detection. The blow away beam is resonant with $6s_{1/2}f = 4 \rightarrow 6p_{3/2}f' = 5$, same as the MOT light but with no detuning. This light

---

[12] Vescent Photonics D2-100-DBR laser with a D2-110 spectroscopy module

will only blow away atoms in the $|f = 4\rangle$ state so after a 50 μs pulse we know if our atoms were in $|0\rangle$ or $|1\rangle$. As mentioned in section 2.1 and seen in Fig. 2.3 this light comes from the same laser as the main 3D-MOT cooling light but is split off before the TA and sent through a single pass AOM driven at 219 MHz. Then it is coupled through a fiber and sent to the experiment. Polarization and position does not matter as long as the beam is overlapping with the atoms. The blow away light is collimated to have a beam waist around 0.5 mm and sent into the chamber adjacent to one of the MOT beams.

2.5 Beam scanners for Single Qubit Addressing

The ability to address specific sites in the array is essential in achieving high fidelity quantum operations. Single site addressing of single neutral atom qubits can be achieved several ways. Acousto-optical modulators can be used to spatially scan tightly focused beams [52, 53]. Microelectromechanical systems (MEMS) can also be used to steer beams across qubit sites[48] . Magnetic field gradients can be used to introduce position dependent qubit frequencies which can then be addressed with microwave pulses tuned to those frequencies [54].

Here an optical system is designed for single site addressing of single atoms trapped in a two dimensional array using two acousto-optical modulators (AOMs) to scan over both dimensions. A combination of telescopes and relay optics are used to convert the angular deflection created by the AOM into a linear translation. Acousto-optic beam scanners are designed for both 459 nm and 1038 nm light and their performance is characterized.

2.5.1 Design

Acousto-optical modulators (AOMs) are tools commonly used in optical labs for a variety of applications as they allow for fast electronic control of intensity, position, and frequency of laser beams. This application uses two AOMs to control the two dimensional position of a tightly focused beam on an array of single atoms separated by 3.8 μm. A RF source drives a transducer which creates an acoustic wave in an acousto-optical crystal. This acoustic wave forms a sinusoidal grating which diffracts incoming optical beams. To the incoming beam, the crystal looks like a

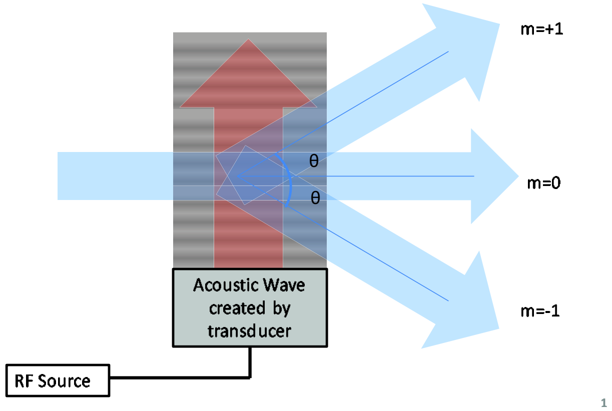

Figure 2.10: Basic picture of how an AOM works

Bragg cell with parallel planes from which it can reflect. Reflections of the plane will interfere constructively when the Bragg condition, $m\lambda = 2d\sin(\theta_{\mathrm{B}})$, is met. In this case, the distance between parallel planes, d, is the wavelength of the sound wave, or $d = \frac{V_{\mathrm{acoustic}}}{f_{\mathrm{RF}}}$ with $V_{\mathrm{acoustic}} = 4200$ km/s for a Tellurium Dioxide crystal used in this set up. f_{RF} is the RF frequency being applied to the crystal, nominally 150 MHz here. When the incoming beam is at an angle $\theta_{\mathrm{B}} \approx \frac{\mathrm{m}\lambda}{2d} = \frac{m\lambda f_{\mathrm{RF}}}{2V_{\mathrm{acoustic}}}$ with respect to the normal of the face of the AOM, reflections off of the Bragg planes created by the acoustic wave will constructively interfere into the m^{th} order, and destructively interfere into all other orders. The resulting m^{th} order will be deflected by an amount $2\theta_{\mathrm{B}}$ which is linear in RF frequency. This means by changing the RF frequency driving the AOM, the angular position of the m^{th} order is changed.

2.5.2 Optical Layout

The optics in this system need to achieve two things simultaneously. The first is to convert the deflection angle introduced by the AOM into a linear translation. The second is to resize the beam so it is appropriately sized at each AOM to optimize diffraction efficiency. The first requirement is illustrated in Fig. 2.11. If the AOM sits at the focal plane of the lens, then the beam passes through

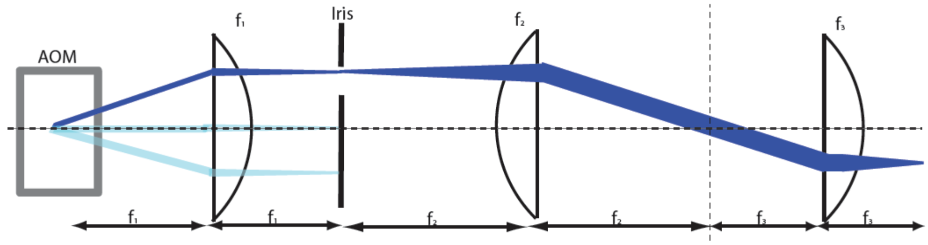

Figure 2.11: Illustration of how the angular deflection introduced by the AOM is transformed into linear translation.

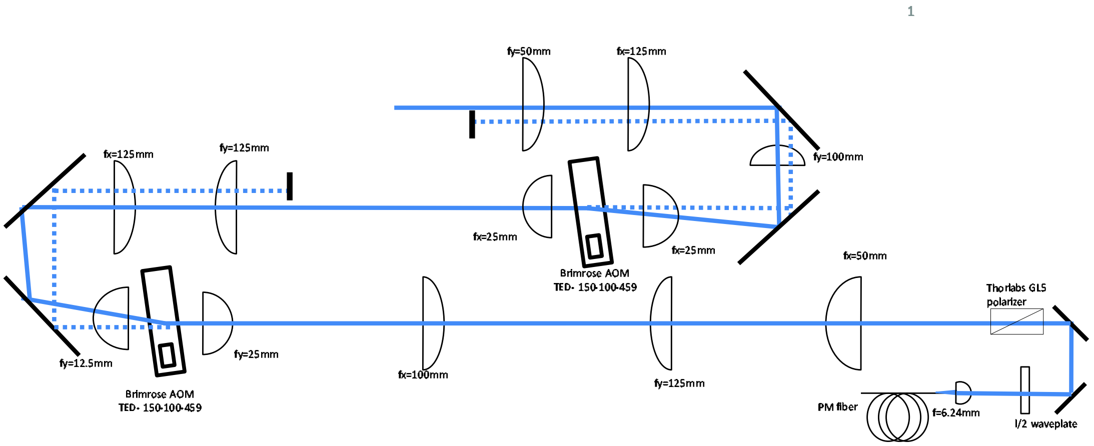

Figure 2.12: Full layout of the beam scanning optics.

the focal plane at some angle set by the AOM RF frequency. A ray that passes through the focus of an ideal lens, with focal length f_1, is transformed by the lens into a ray that is parallel to the optical axis, and thus angular deflection is transformed into linear translation. Adding another lens, with focal length f_2, which sits a distance $f_1 + f_2$ from the first lens magnifies the rays input angle by f_2/f_1 . A third lens, confocal to the second, transforms this magnified angle back into linear translation. The result in the image plane is a linearly translating, focused beam.

Next, we need to consider the optimal beam waists at the AOMs. There is a trade-off between having good diffraction efficiency over a wide range of RF frequencies and having fast switching times. The more Bragg planes that the beam overlaps with, the more ways the reflections can add constructively and thus the better the diffraction efficiency. This seems to imply we want a very large beam waist in the deflection direction, or at least we require this beam waist to be much larger than the wavelength of the acoustic wave. However the switching time of the AOM is limited by the time is takes the acoustic wave to propagate across the optical beam, or T $\sim 2w_{1/e^2}/V_{\text{acoustic}}$. Since we wish to use the device to uniformly scan over a large array, we need good diffraction efficiency throughout a large part of the operating bandwidth of the AOM. Since our crystal is effectively 2.1 mm (active aperture) in the scanning dimension, we choose our beam waist in that dimension to be 1 mm. In the orthogonal dimension, the active aperture is 0.5 mm, and we choose a beam waist of 0.1 mm. This should give us the diffraction efficiency we desire with switch times of about 500 ns.

Using cylindrical lenses, a $2\times$ telescope in the saggital plane and a $1/5\times$ telescope in the tangential plane will give the beam waists needed in the plane of the first AOM. This is followed by another pair of cylindrical telescopes that are $10\times$ in the tangential plane and $1/10\times$ in the saggital plane. This inverts the dimensions of the beams at the first AOM to the second AOM which will deflect in the tangential plane. The final pair of telescopes is the reverse of the first pair. This results in a final output that is the same as the input with a waist of w_0. From here, final imaging optics are needed to image the beams onto the atomic array. The proposed layout with the appropriate focal lengths is shown in Fig. 2.12. For a chosen input of $w_0 = 0.5$ mm, the waists in the tangential and saggital plane are 0.1 mm and 1 mm, respectively, at the first AOM. Then at the second they are 1 mm and 0.1 mm, respectively.

2.5.3 Performance

2.5.3.1 Switching Time measurement

Rise/fall times can be measured by placing a knife edge in an imaging plane. Another lens placed a focal distance away will focus the beam onto a fast photodetector. This lens converts linear translation into angular deflection so that the beam position is constant in the plane of the detector. To measure a rise time, the AOM is switched from an off position, where the deflected beam is blocked by the knife edge, to an on position. The photodetector will see an exponentially rising signal as seen in Fig. 2.13. This signal can be fit to an exponential of the form $1 - e^{-t/\tau}$and the 90 $\%$ - 10 $\%$ time extracted. The time is takes to switch between sites is around 0.9 μs.

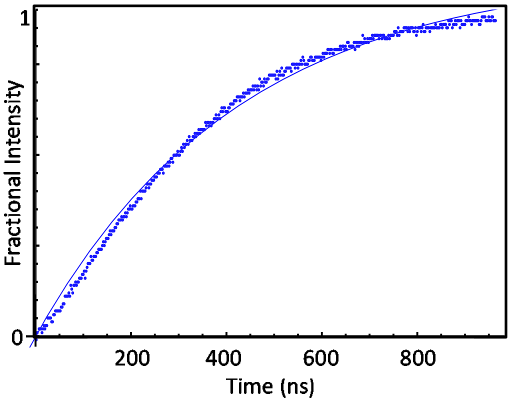

Figure 2.13: Measurement of scanner response time, data fitted to $1 - e^{-t/\tau}$ and τ =426 ns. 90 % - 10 % time is 935 ns.

2.5.3.2 Diffraction Efficiency

To check the beam scanning performance, the transmission through the scanner is measured at different RF settings which approximately corresponds to locations of different trap sites. The efficiency is taken to be the power after the final cylindrical lens divided by the power out of the fiber.

Fig. 2.14 shows the diffraction efficiency for the 1038 nm scanner as an example. The middle column has the best efficiency which then falls off on the edges. Notice the fall off is more dramatic in the horizontal direction than in the vertical direction. One might naively expect that the efficiency of the whole system might be calculated by simply multiplying the efficiencies of the two AOMs, independent of each other. The fall off is much steeper in the horizontal direction than in the vertical direction.

To better understand this consider what is happening between the two AOMs depicted in Fig. 2.15. After the first AOM the beam is deflected by an angle that is magnified by a factor determined by the lenses in between the AOMs. The first AOM is deflecting in the horizontal direction. For the 1038 nm system, this factor is 10.4. We want to know how the incoming angle at the second AOM, which is due to the deflection by first AOM, affects the diffraction efficiency

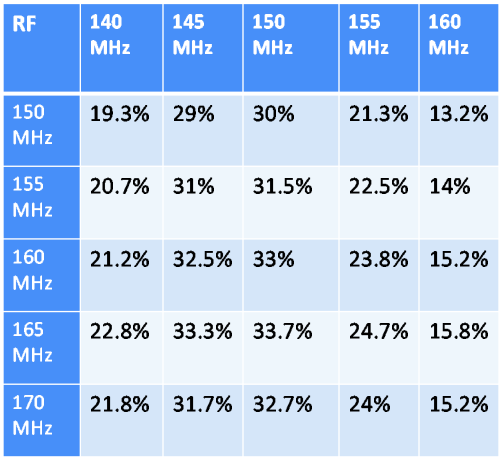

RF	140 MHz	145 MHz	150 MHz	155 MHz	160 MHz
150 MHz	19.3%	29%	30%	21.3%	13.2%
155 MHz	20.7%	31%	31.5%	22.5%	14%
160 MHz	21.2%	32.5%	33%	23.8%	15.2%
165 MHz	22.8%	33.3%	33.7%	24.7%	15.8%
170 MHz	21.8%	31.7%	32.7%	24%	15.2%

Figure 2.14: measured diffraction efficiencies compared to naive calculated efficiency in parentheses estimated by multiplying together the diffraction efficiencies of the independent AOMs

of the second. The incoming angle is being deflected in the plane that is orthogonal to the deflection direction of that AOM. Recall that in this direction, the crystal is very small, 0.5 mm. The effect is estimated by calculating the overlap between the acoustic mode of the second AOM and the optical mode of the beam as a function of the incoming deflection angle. The acoustic wave is approximated as a collimated Gaussian beam which propagates in the x-direction or the AOM deflection direction

$$E_{\text{acoustic}}(x,y,z) = 2\sqrt{\frac{P}{\pi w_y(x) w_z(x)}} e^{\frac{-y^2}{w_y(x)^2}} e^{\frac{-z^2}{w_z(x)^2}}. \tag{2.14}$$

The size of this acoustic Gaussian beam is approximately the size of the transducer on the crystal which is w_{0z} = 4 mm in the direction in which the optical beam propagates and $w_{0y} = .25$ mm in the orthogonal direction. The optical beam is the usual diverging Gaussian beam. Assume the waist of this beam forms at the center of the crystal where $z = 0$

$$E_{\text{optical}}(x,y,z) = 2\sqrt{\frac{P}{\pi w_x(z) w_y(z)}} e^{\frac{-x^2}{w_x(z)^2}} e^{\frac{-y^2}{w_y(z)^2}}, \tag{2.15}$$

where

$$w(z) = w_0\sqrt{1 + (\frac{z}{z_{\text{R}}})^2}, \tag{2.16}$$

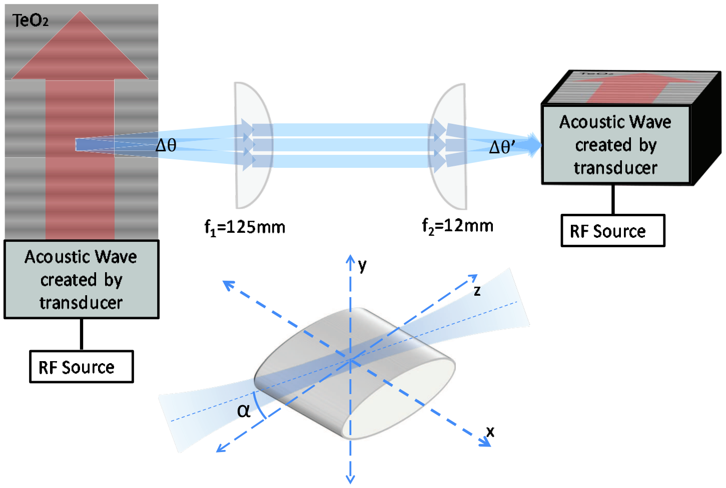

Figure 2.15: The first AOM introduces a deflection angle which is magnified by the lenses between AOMs. The angle will affect the diffraction efficiency of the second AOM which will limit the scanning ability of the system.

and

$$z_{\mathrm{R}} = \frac{\pi w_0^2}{\lambda}. \tag{2.17}$$

Allowing the beam to rotate by a small amount, α, in the y-z plane the following coordinate transformation can be made:

$$x' \rightarrow x \tag{2.18a}$$

$$y' \rightarrow y cos\alpha - z sin\alpha \tag{2.18b}$$

$$z' \rightarrow z cos\alpha - y sin\alpha \tag{2.18c}$$

Choosing $w_{0y} = 0.1$ mm and $w_{0x} = 1$ mm and calculating the overlap between the acoustic wave and the optical wave as a function of α gives

$$|O|^2 = \int \frac{1}{2} E_{\text{optical}}(x', y', z') E_{\text{acoustic}}(x, y, z) \mathrm{dxdydz}. \tag{2.19}$$

For the 1038 nm scanner, $\alpha = \pm 1.5$ degrees for the outer most columns in Fig. 2.14, $\pm .75$ for the 2nd and fourth, etc. We assume the third and middle column are at $\alpha = 0$. Numerically solving

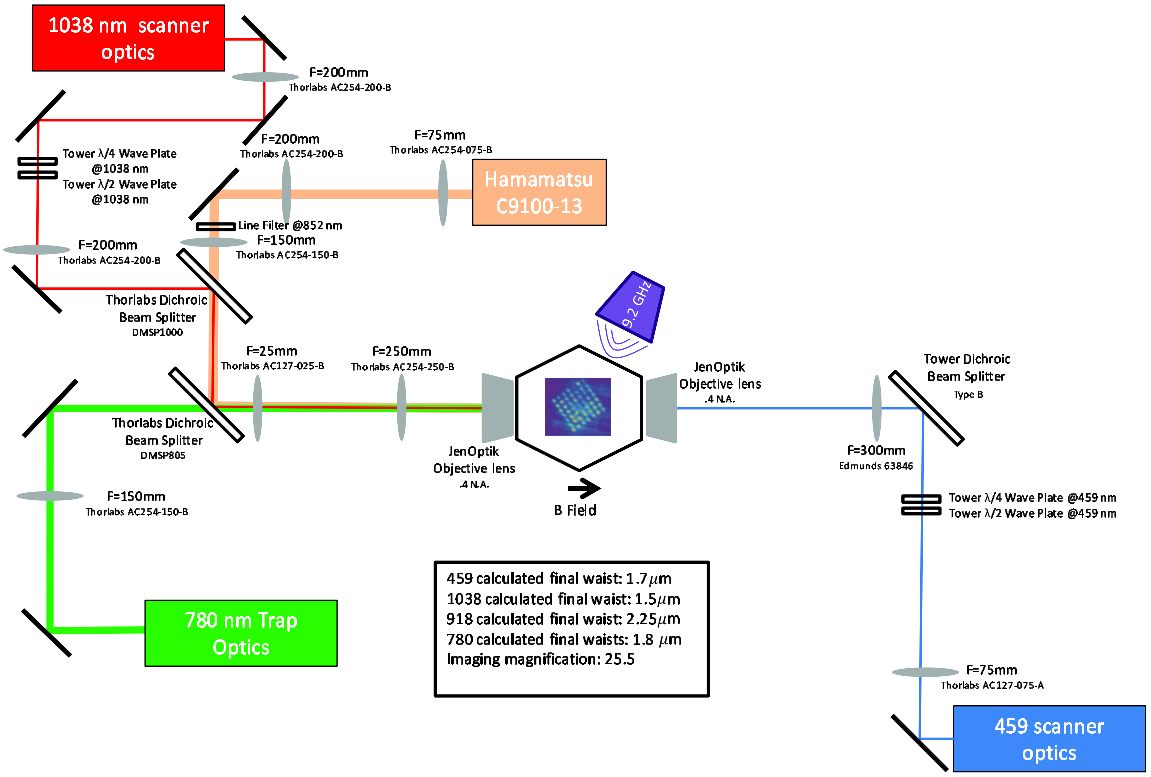

Figure 2.16: Complete system with relay optics used and predicted waists and magnifications at atoms.

this integral for 1038 nm at small values for α results in an overlap factor for the different columns. For the edges, the overlap factor is 0.755. For the second and fourth its 0.925. Adding this factor to our naive expectations, the predictions are now much closer to the measured values.

2.6 Putting it all together

Now we have described all the component parts, let's see how they fit together. All the relay and imaging optics needed to create tightly focused beams at the atoms and needed to image the array at single atom resolution are shown in Fig. 2.16 along with the beam waists at the atoms.

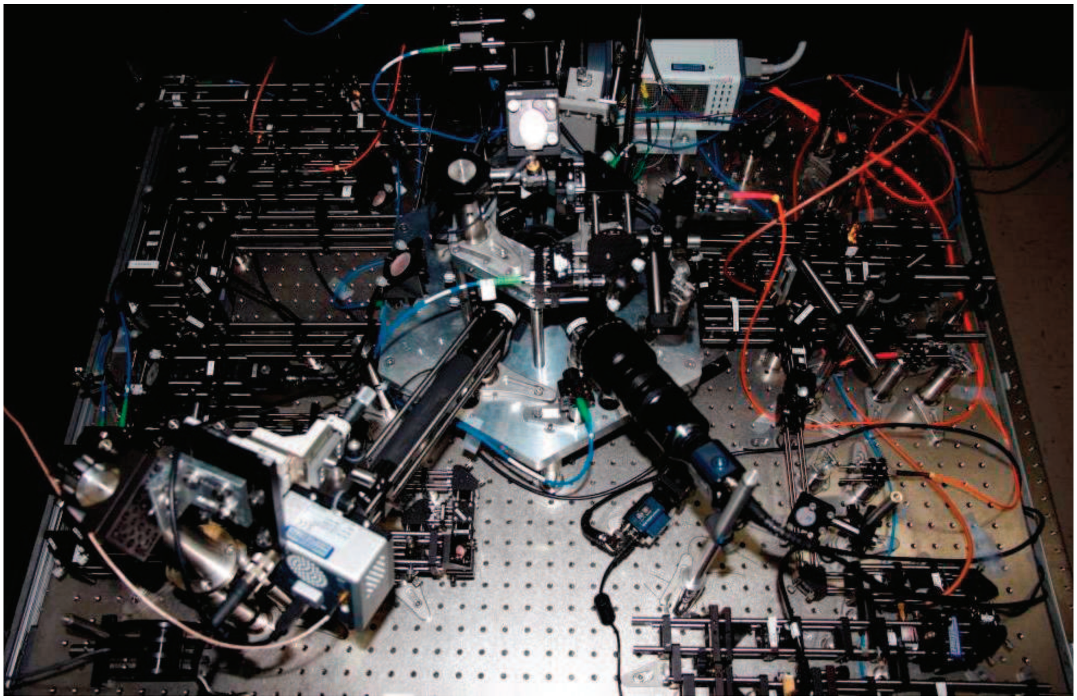

Figure 2.17: Photograph of experimental set-up.

Everything is mounted on a 3×4 foot Invar breadboard. A grounded aluminum box is placed around the breadboard to act as a partial Faraday cage, as well as a shield from light, wind currents and dust. The box uses a combination of fans, heating/cooling plates, and TEC temperature controllers to stabilize the internal temperature to within 0.1° C independent of the outside lab temperature. Fig. 2.17 is a photograph taken inside the experiment box. In addition to the main experimental components identified above, seen here are cameras and beam pick offs used for diagnostics as well as the temperature control equipment.

Chapter 3

Qubit Preparation

The first step in preparing qubits for gate experiments is loading single atoms into the trap array. After the 3D-MOT is loaded from the 2D-MOT for $\sim$500 ms, a phase of polarization gradient cooling (PGC) [51] is implemented. During PGC, the power in each MOT beam is decreased to 100 μW while the detuning is increased to -7 Γ and the magnetic field gradient is switched off. The magnetic gradient is left off for the remainder of the experiment cycle. Shimming magnetic field coils are used to cancel out any stray magnetic fields. 5 ms of PGC results in approximately 10-20 μK atom temperature measured using time-of-flight techniques [55] looking at the fluorescence from the MOT. To first order, the shim settings along with beam powers and detuning are set by minimizing the MOT temperature after the PGC phase. The optical dipole traps which spatially overlap the atomic cloud are switched on 4 ms into the PGC phase which continues for another 1 ms to ensure that the atomic cloud is cold but still dense for sufficient trap loading. After 5 ms of PGC, the cooling light is extinguished while the traps remain on for 100 ms letting any untrapped atoms fall away. If this time is not sufficiently long the background of the fluorescence image will be too high due to leftover untrapped atoms. The cooling beams are then switched back on for the first readout phase. The readout light is left on for an extra 100 ms before triggering the camera for an exposure. The purpose of this is to ensure light assisted collisions [44] have eliminated the chance that more than one atom has been loaded per trap. In this readout phase, each MOT beam has about 100 μW of power with -8 Γ detuning, similar to the PGC phase to ensure the atoms are not heated out of the trap during the readout. When loading is initially achieved, the PGC settings along with the readout settings, including the shims, and various timings described above can be optimized to give the best single atom signal, meaning the best discrimination between the zero and

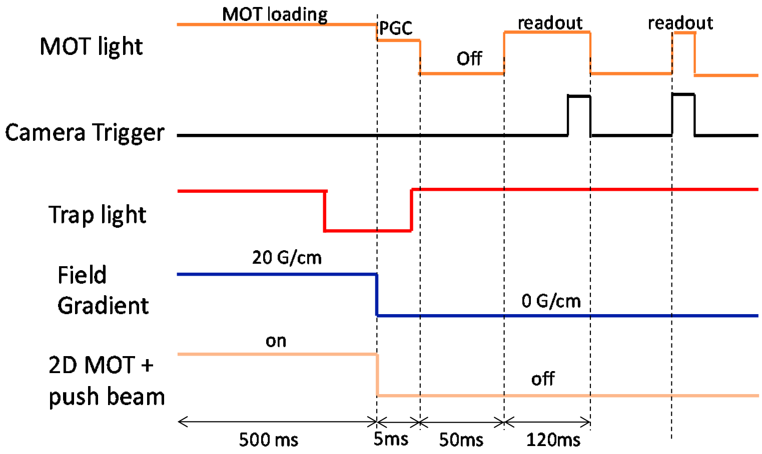

Figure 3.1: General timing sequence for single atom loading experiments.

one atom signal. After readout is optimized, the settings are rescanned to give optimal retention, which is discussed in section 3.3. A generalized timing sequence is seen in Fig. 3.1. Each trap site is imaged onto the EMCCD with an effective pixel size of 0.6 × 0.6 μm. The fluorescence from a single site spreads over a 3 × 3 pixel area which defines the site's region of interest (ROI). During a fluorescence measurement, the pixel values in each ROI are summed and plotted on a histogram. For each of the 6 (49) trap sites, a single atom peak is clearly resolved from the zero atom background peak, examples of which are seen in Fig. 3.2 for the 6 site array.

3.1 6 Site Array Loading

The histograms in Fig. 3.2 show examples for all six sites with 5000 measurements. The exposure time for this experiment is 50 ms. The loading rate of each site is noted beneath the histogram. These histograms show a clear separation of the zero-atom background from the one-atom peak. No events with two or more atoms in a single trap are observed here, although we cannot exclude the possibility that we load two atoms and lose them rapidly during the pre-readout or readout. On some of the sites, for example Region 3, there are some events that show up in between the zero-atom and one-atom signal. We suspect these are atoms that are lost during readout. In the previous chapter, section 2.3, an expected signal strength was predicted given our

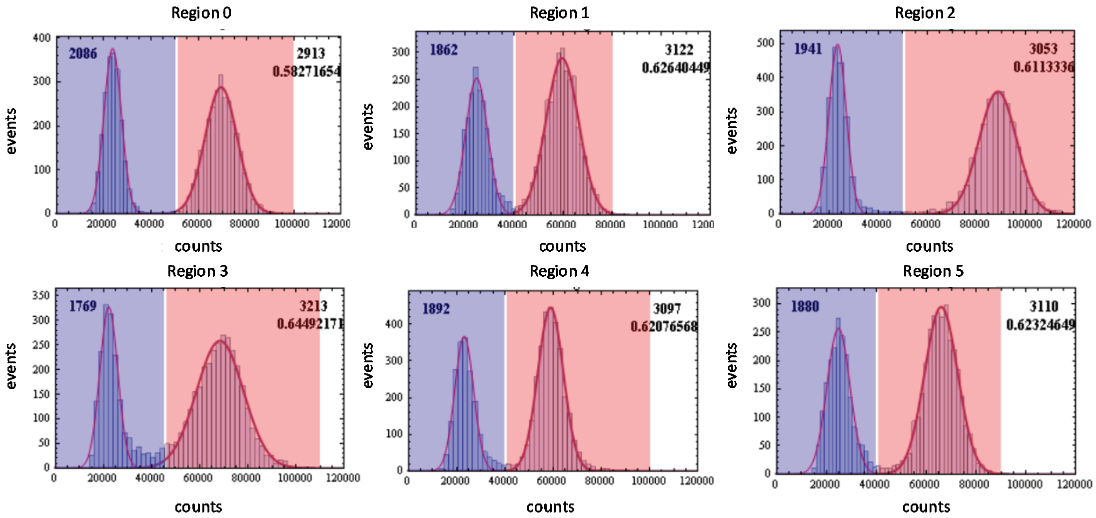

Figure 3.2: Loading histograms for 6 site array for 5000 shots, 50 ms exposure time. Data from 2012_11_02_17_44_17. On each histogram the number of 0 atom and 1 atom events is noted along with the loading rate.

readout parameters, magnification, and background signal. If the trap centers induce a Stark shift of 1 Γ to 2 Γ the expected output signal is between 6.9 $\times 10^4$ and 7.5 $\times 10^4$ counts which agrees with what is seen in Fig. 3.2. In section 3.4.2, we measure this Stark shift in the 49 site array using a resonant beam and find an average shift of -8 MHz or 1.5 Γ. The difference in the signal strength from site to site seen in Fig. 3.2 is most likely due to this Stark shift varying from site to site due to slight trap misalignments.

Fig. 3.3 shows a three dimensional image of the six site traps. The image is an average of 105 out of 5000 events where all six sites have loaded a single atom. This image shows how we resolve each site well given our imaging apparatus.

3.2 49 Site Array Loading

Similar histograms are produced for the 49 site array. Fig. 3.4 (a) shows a histogram for the number of atoms loaded in a single measurement for 1000 measurements. Here the average atoms loaded per shot is close to 29. On average about 60 % of the sites are loaded in a single measurement. Fig. 3.4(b) maps out the loading rate for each site in a 1000 measurement experiment.

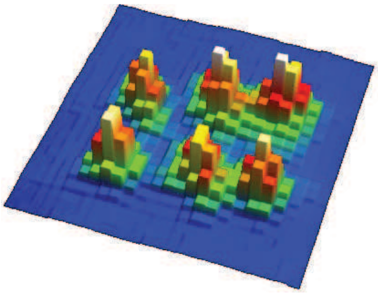

Figure 3.3: Average image for the 105 out of 5000 events where all six sites loaded single atoms shows good single site resolution. Data from $2012\_11\_02\_17\_44\_17$.

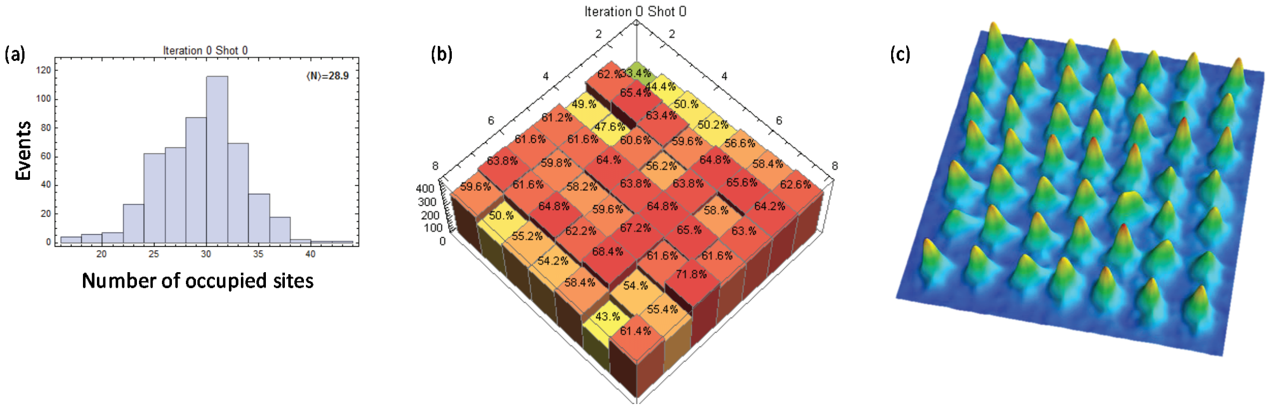

Figure 3.4: (a)Histogram showing the number of atoms loaded in a single shot for 1000 shots, average of 29 atoms (b)average loading for individual sites averages over 1000 shots (c)average in 3D. Data from $2013\_11\_14\_15\_18\_54$.

One can use images like this to assess the uniformity of the array. Part (c) shows an accumulative averaged over 1000 measurements plotted in three dimensions.

The average loading rates we see are sub-Poissonian and also above that expected from light-assisted collisions or collisional blockade [44]. We believe this loading rate can be even further improved by implementing repulsive light-assisted collisions [45, 56]. In these references, the authors showed 82.7 % and later 91 % loading into a small dipole trap. Higher loading rates would significantly improve our data rate and implementation of such techniques are currently being explored.

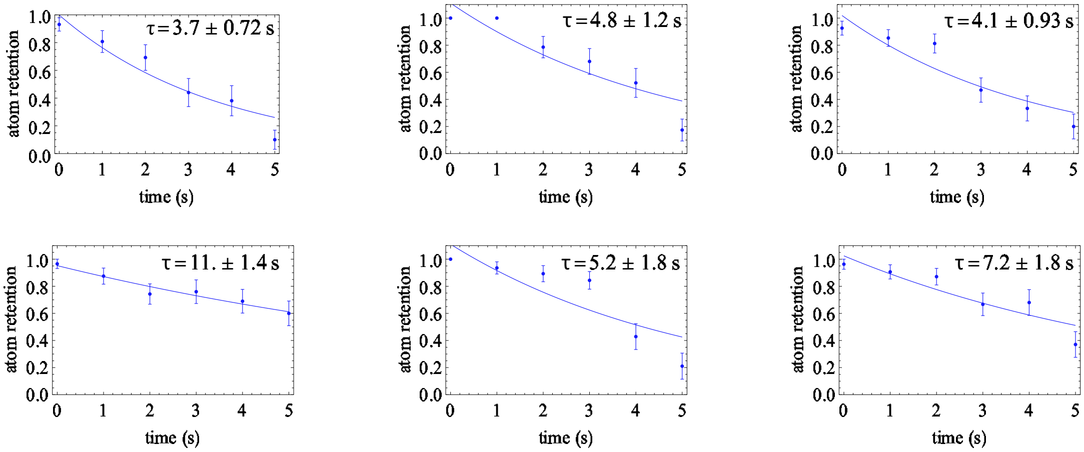

Figure 3.5: Lifetime measurement for each of the sites of the 6 site array. Data from 2013_01_17_10_04_54.

3.3 Trap Characterization

3.3.1 Retention and Lifetime

The retention rate of each trap is measured by taking two camera shots per measurement with a gap time in between shots. The retention rate is defined as the percentage of measurements that have an atom in the second shot, conditional on there being an atom in the first shot. Our traps consistently have retention rates between 0.9 and 1 for a gap time of 35 ms, which is the minimum time allowed between camera exposures. By varying the gap time, we can measure a lifetime for each trap. The retention is measured for each gap time and the results are fit to a function $Ae^{-t/\tau}$. In the 6 site array, we measured a lifetime, τ, varying from 3.7 to 11 s for the different sites as seen in Fig. 3.5. The lifetime due to background collisions with untrapped atoms is measured to be 24 s using a milli-Kelvin deep red-detuned trap created using 1038 nm light focused down to 3 μm. The shorter trap lifetimes are due to the lower trap depth. The variation is due to imperfections in the array alignment which can lead to trap depth variations. The 49 site array shows a similar

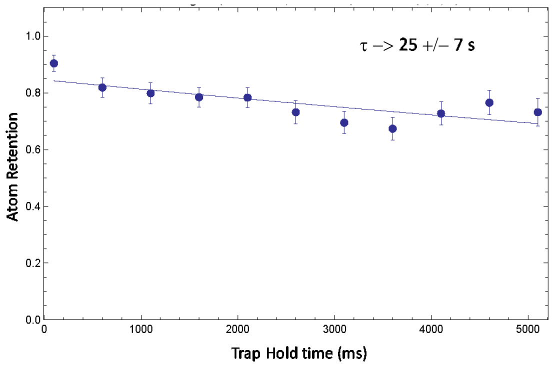

Figure 3.6: Lifetime measurement in a red-detuned optical dipole trap gives a background collisional loss time of 24 s. Data from 2012_09_06_15_20_22.

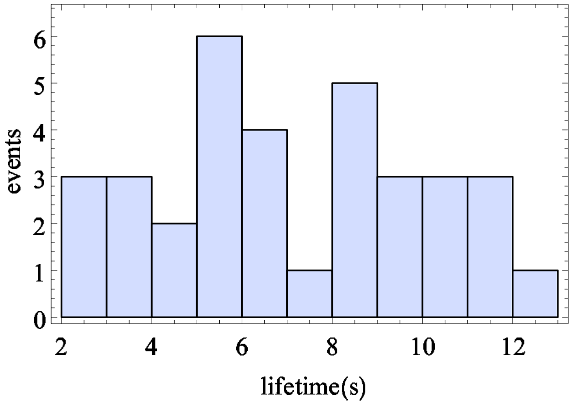

Figure 3.7: Histogram for the lifetimes measured in the 49 site array. The average is 7.2 s with a standard deviation of 2.9 s. Data from 2014_03_17_10_23_42.

variation of lifetime for different sites. The average in the 49 site array is measured to be 7.2 s. A histogram of the 49 fitted lifetimes is seen in Fig. 3.7.

3.3.2 Atom Temperature

We can measure the temperature of the atoms in the traps by doing a release and recapture experiment [57]. After trapping an atom the trap light and MOT light are turned off for some time,

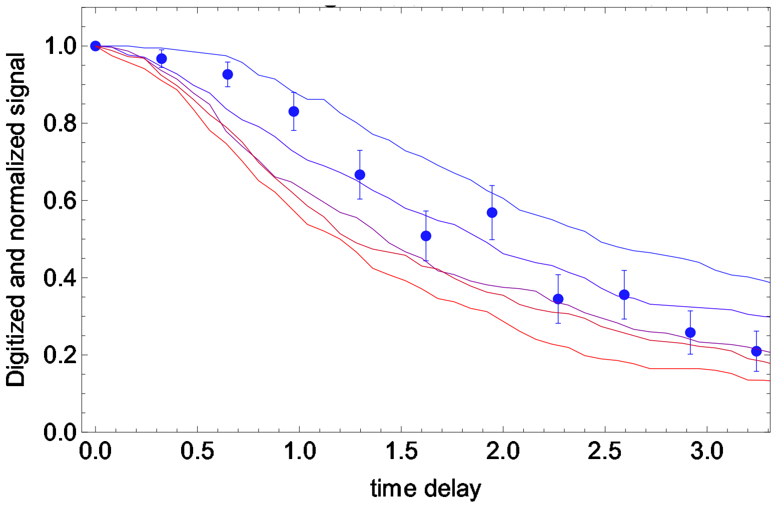

Figure 3.8: An example of single atom temperate data compared to simulations for atom temperatures 10, 20, 30, 40, 50 μK. Data from $2012\_10\_01\_18\_37\_57$.

t_{drop}, and the atom is allowed to fall under the force of gravity. Recapture probability is measured as t_{drop} is varied and compared to Monte Carlo trajectory simulations of atoms in ideal trapping potentials to estimate the temperature. An example of this is seen in the Fig. 3.8 where simulations are done for atom temperatures of 10, 20, 30, 40 and 50 μK. From data sets like these we estimate a single atom temperature between 10 μK and 20 μK.

There is some uncertainty in comparing the data to a simulation as the simulations depend on trap depth and geometry which we only know approximately. We instead turn to T_2^* coherence measurements to estimate the trapped atom temperature. This will be the subject of section 4.4.2.

3.3.3 Trap Frequency

The characteristic trap frequencies are measured by modulating the trap amplitude [58]. Modulation at twice the trap frequency will result in atom loss due to parametric heating. A spectrum of one of the traps in the six site array is seen in Fig. 3.9. In this spectrum a resonance is seen around 18 kHz, corresponding to $\omega_z = 2\pi \times 9$ kHz and a broader resonance around 90 kHz corresponding to the radial frequency, $\omega_x = 2\pi \times 45$ kHz. The radial frequency agrees with the calculated trap frequency predicted in section 2.2.1 to about 10 $\%$. The axial frequency is about 50% higher than

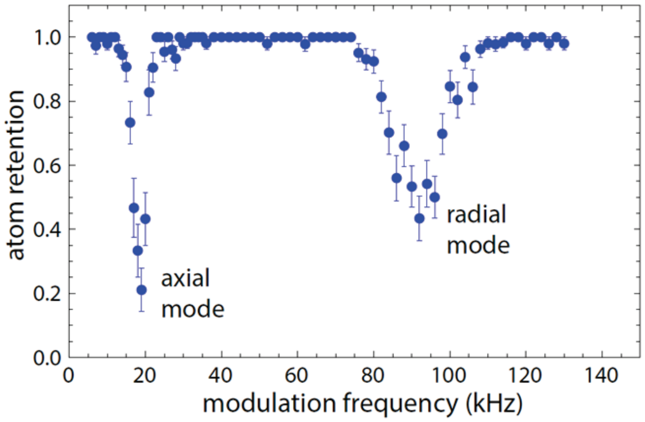

Figure 3.9: Spectrum of trap frequencies for a single site in the 6 site array. Data combined from 2013_04_19_11_25_40 and 2013_04_19_16_19_33.

expected. This may be due to the fact that we have observed that the individual tightly focused beams diverge more rapidly than that of normal Gaussian beams [2].

3.4 State Preparation and Detection

3.4.1 State Preparation via Optical Pumping

Using the optical pumping scheme described in Chapter 2 we can study the optical pumping properties across the array. A common method for evaluating optical pumping fidelity is to measure the pumping time and the depumping time. The pumping time is measured by applying a time varying optical pumping pulse to prepare the atoms in $|f = 4; m_f = 0\rangle$ followed by a microwave π-pulse (discussed in Chapter 4) which should transfer the atoms into $|f = 3; m_f = 0\rangle$ if the pumping is working well. The percentage of atoms in $|f = 3; m_f = 0\rangle$ as a function of time is fit to the function, $A - Be^{-t/\tau_{\text{pump}}}$. The pumping time, τ_{pump}, should be around 50-100 μs. We choose a time about 10 $\times\tau_{\text{pump}}$ to ensure that the pumping process has been completed. Typically in experiments the optical pumping time is set to 2 ms. Measuring the depumping time amounts to doing a 2 ms pumping phase followed by a phase with the repumper off but the 894 nm light on. This will eventually depump the atoms back into the $|f = 3\rangle$ state but this should happen much

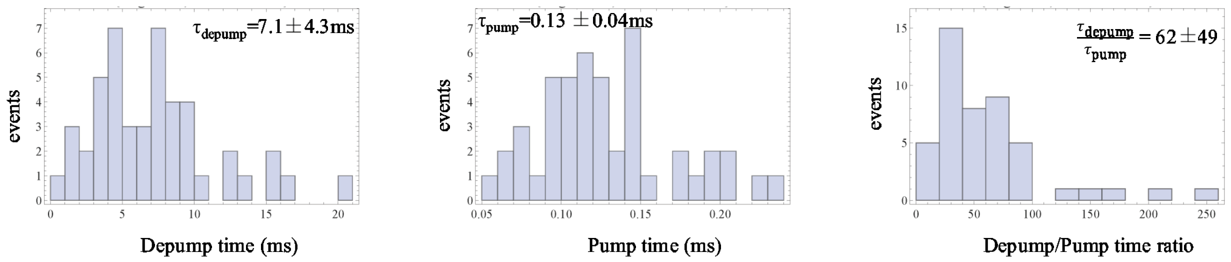

Figure 3.10: Pump and depump data for the 49 site array. The average depumping time is measured to be 7.1 ms with an average pumping time of 130 μs. The ratio of depumping time to pumping time is 62. The larger this ratio is the better the pumping fidelity should be. Data combined from 2014_07_03_07_41_33 and 2014_07_03_07_31_07.

slower than the pumping time if things are set up properly. Using these times the optical pumping settings are evaluated and optimized.

A bias magnetic field of 1.5 G is applied in the trap axis direction. To achieve good pumping fidelity, the linear polarization direction of the optical pumping beam must be well aligned to this bias field. As mentioned in section 2.4 , a polarizing beam cube is placed just before the light enters the cell to clean up the polarization of the beam. With this polarization defining the quantization axis, the remaining shims are scanned until the effective bias field matches this direction. The easiest way to find the proper settings for the shims is by maximizing the depumping time. The pumping time is minimized by scanning the laser frequency to compensate for Stark shifts from the 780 nm light at the trap centers-either finding an average across the array or focusing on a couple sites. Results of the pumping and depumping time measurements are shown in the Fig. 3.10 for the 49 sites in the array after the optimization procedure described above has been completed. The ratio of depumping time to pumping time should be as high as possible for high fidelity state preparation. An average ratio of 62 should translate into a pumping fidelity of $1 - \frac{1}{62} = 0.984$. The varying Stark shifts for the different traps across the array tends to wash out the average. We achieve higher fidelity if we focus just on the sites we care about. For example, region 4 in the data presented below has a pumping time of 0.088 ms with a depumping of 25 ms giving a fidelity of 99.6%. In Chapter 4 we will measure these fidelities by looking at microwave Rabi flopping amplitudes.

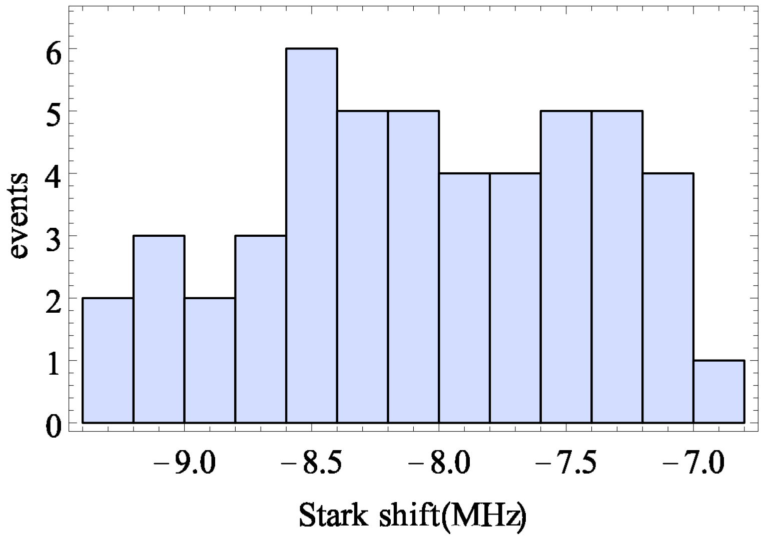

Figure 3.11: Stark Shift of D2 line in the 49 site array. The mean shift relative to an atom in free space is found to be -8 MHz or 1.5 Γ. Data from $2014\_10\_11\_14\_59\_20$.

3.4.2 State Detection

We use a single beam on resonance with $f = 4 \rightarrow f' = 5$ to perform state detection measurements described in section 2.4. The beam has a waist of 0.5 mm with 500 μW of power. This beam blows away the atoms in $|f = 4\rangle$ but does not interact with the atoms in $|f = 3\rangle$. Spectroscopy of this blow away beam is another test of the array uniformity. As mentioned throughout this chapter, different amounts of 780 nm light at the trap centers will induce different Stark shifts of atomic transitions used for state control, in this case the $6p_{3/2}$ line. These varying shifts will cause site to site differences in readout, cooling efficiency, and optical pumping efficiency, for example. This will also cause a varying differential shift between the two hyperfine states which means different qubit frequencies. For these reasons, it is important to quantify these shifts. Scanning the frequency with a fixed blow away pulse time of 4 μs we look for a minimum in atom retention where the blow away is most efficient. Fig. 3.11 shows the mean transition shift relative to a free-space, unshifted atom is equal to -8 MHz or 1.5 Γ with a standard deviation of 0.65 MHz. This gives a fractional deviation of 0.65/8=8 $\%$. Given 2 W of total 780 nm power at the atoms we expect a shift at the trap center of about -2 MHz increasing to about -60 MHz at a trap corner.

From section 2.2.1, the trap center intensity is related to the effective trapping intensity by $I_c/I_t = 2e^{-s^2/2}(1 - 2e^{-s^2/2}) = 0.17$ at s = 2.1. The average light shift at the trap center is 0.17 × 570 μK = 97 μK with a standard deviation of about 10 μK [2].

This variation across the array may come into play when considering the dephasing of the qubit states. For our hyperfine qubit with a transition frequency of 9.2 GHz, the 72 nm (32.5 THz) trap detuning from the Cs D2 transition gives a standard deviation of the qubit frequency across the array due to the trap-induced Stark shifts of 10 μK × $\frac{.0092}{.0092+32.5}$ = 0.0028 μK or 60 Hz. This will cause dephasing of the qubits on time scales of a few milliseconds if left uncompensated [59, 60]. Dephasing and coherence will be discussed more in Chapter 4.

Chapter 4

Single Qubit Operations

Single qubit operations involve driving the transition between $|0\rangle$ and $|1\rangle$ or in our case the $|f = 3; m_f = 0\rangle$ and $|f = 4; m_f = 0\rangle$ hyperfine levels of the $6s_{1/2}$ ground state of cesium. A 1.5 G bias field is applied along the trap axis in order to isolate the transition by Zeeman shifting other m_f transitions out of resonance. This ensures a simple two level system. The qubit state is described by a complex unit vector in a 2-dimensional Hilbert space. Such a vector can be written as

$$|\psi\rangle = \cos\frac{\theta}{2}|0\rangle + e^{i\phi}\sin\frac{\theta}{2}|1\rangle. \tag{4.1}$$

A useful geometrical interpretation arises when this vector is depicted as a point on the surface of a unit sphere known as the Bloch sphere. θ and ϕ fully describe this vector since it is constrained to have norm 1. The state vector can also be expressed in Cartesian coordinates as

$$(x, y, z) = (\sin\theta\cos\phi, \sin\theta\sin\phi, \cos\theta). \tag{4.2}$$

In this representation it is easy to show that $|0\rangle = (0, 0, 1)$ and $|1\rangle = (0, 0, -1)$. Single qubit operations are unitary transformations acting on a qubit. This can be thought of as a rotation on the Bloch sphere which transforms $|\psi\rangle$ to $U|\psi\rangle$. The rotations about the $x-$, $y-$ and $z-$ axes of the Bloch sphere are represented as

$$R_i = e^{-i\theta\sigma_i/2}, \tag{4.3}$$

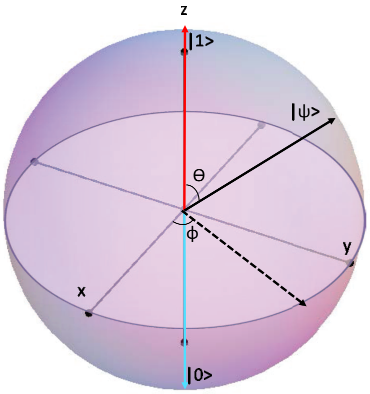

Figure 4.1: The Bloch sphere is a useful geometric interpretation of a qubit. A qubit can be represented by a complex unit vector in a 2-dimensional Hilbert space which points to a place on the surface of the Bloch sphere. Single qubit operations are then just rotations to different locations on the surface of this sphere.

for $i = x, y, z$ and the σ_i's are the respective Pauli operators. In the computational basis this becomes

$$R_x(\theta) = \begin{pmatrix} \cos\theta/2 & -i\sin\theta/2 \\ -i\sin\theta/2 & \cos\theta/2 \end{pmatrix}, \tag{4.4a}$$

$$R_y(\theta) = \begin{pmatrix} \cos\theta/2 & -\sin\theta/2 \\ \sin\theta/2 & \cos\theta/2 \end{pmatrix}, \tag{4.4b}$$

$$R_z(\theta) = \begin{pmatrix} e^{-i\theta/2} & 0 \\ 0 & e^{i\theta/2} \end{pmatrix}. \tag{4.4c}$$

These rotations can be driven in a few different ways. The magnetic dipole transition can be directly driven using microwaves tuned to the 9.2 GHz hyperfine splitting but because microwaves cannot be focused down to the 1 μm level needed for single site addressing, this method is used only to do global operations on all array sites. For rotations on a single site additional gradients can be introduced either by adding a tightly focused laser beam to induce a position dependent Stark shift or by adding a magnetic field to induce a position dependent Zeeman shift. Here we use an additional Stark shifting beam [61]. Another strategy is to drive a two-photon Raman process.

4.1 Semi-Classical Derivation

Single qubit operations can be understood using the semi-classical picture of a two-level quantum mechanical atom interacting with a classical, monochromatic field [34]. The Hamiltonian of this system has two parts,

$$H = H_0 + H_I(t). \tag{4.5}$$

H_0 is the unperturbed atomic Hamiltonian whose eigenvalues and eigenfunctions are the unperturbed atomic energy levels and wavefunctions. For a two level system the wavefunctions satisfy

$$H_0\psi_1(\mathbf{r}) = E_1\psi_1(\mathbf{r}), \tag{4.6}$$

$$H_0\psi_2(\mathbf{r}) = E_2\psi_2(\mathbf{r}), \tag{4.7}$$

for

$$\Psi_n(\mathbf{r}, t) = \psi_n(\mathbf{r})e^{-iE_nt/\hbar}. \tag{4.8}$$

$H_I(t)$ is the interaction term which acts to perturb these eigenfunctions. For a monochromatic oscillating electric field, $\mathbf{E}$, this interaction is equal to

$$H_I(t) = e\mathbf{r}\cdot\mathbf{E}, \tag{4.9}$$

where

$$\mathbf{E} = \frac{\mathbf{E_0}}{2}e^{i\omega t} + c.c.. \tag{4.10}$$

Here ω is the frequency of the field. The electric field interacts with an atomic dipole given by an atom dipole operator $\mathbf{d} = -e\mathbf{r}$ where $-e$ is the electron charge and $\mathbf{r}$ is the position of the electron with respect to the center of mass of the atom. The interaction mixes the two unperturbed states and at any instance in time the wavefunction is equal to

$$|\psi\rangle = c_1e^{-i\omega_1t}|1\rangle + c_2e^{-i\omega_2t}|2\rangle, \tag{4.11}$$

which must obey the normalization condition

$$|c_1|^2 + |c_2|^2 = 1. \tag{4.12}$$

Plugging in equations (4.5) and (4.11) into the time dependent Schroedinger equation yields a set of linear, coupled differential equations for the probability amplitudes

$$i\dot{c_1} = \frac{\langle 1|e\mathbf{r}\cdot\mathbf{E}|2\rangle}{\hbar} c_2 e^{-i\omega_0 t}, \tag{4.13a}$$

$$i\dot{c_2} = \frac{\langle 2|e\mathbf{r}\cdot\mathbf{E}|1\rangle}{\hbar} c_1 e^{i\omega_0 t}, \tag{4.13b}$$

where we have taken $\omega_0 \equiv \omega_2 - \omega_1$. Here the Rabi frequency is introduced and defined as

$$\Omega \equiv \frac{\langle 1|e\mathbf{r}\cdot\mathbf{E_0}|2\rangle}{\hbar} \tag{4.14}$$

such that (4.13) becomes

$$i\dot{c_1} = \Omega\cos(\omega t) c_2 e^{-i\omega_0 t}, \tag{4.15a}$$

$$i\dot{c_2} = \Omega^* \cos(\omega t) c_1 e^{i\omega_0 t}. \tag{4.15b}$$

In most cases we are interested in, the detuning is small such that $|\omega - \omega_0| << \omega, \omega_0$. The terms oscillating at $\omega_0 + \omega \approx 2\omega$ are very fast and average to zero over any reasonable time scale and therefore are ignored. This is known as the rotating wave approximation (RWA). Denoting the detuning $\Delta = \omega - \omega_0$, we can then transform into an appropriate rotating frame to eliminate the time dependence. Making the transformation $c_2(t) = \tilde{c}_2(t)e^{-i\Delta t}$ and applying RWA equations (4.15) reduce to

$$i\dot{c_1} = \frac{\Omega}{2}\tilde{c}_2, \tag{4.16a}$$

$$i\dot{\tilde{c}}_2 = \frac{\Omega^*}{2} c_1 - \Delta\tilde{c}_2. \tag{4.16b}$$

These equations can be solved exactly by starting with the trial solution $c_1(t) = e^{i\kappa t}$. Plugging this into equation (4.16) results in an expression for $\tilde{c}_2$

$$\tilde{c}_2(t) = -\frac{2\kappa}{\Omega} e^{i\kappa t}. \tag{4.17}$$

Using this expression for $\tilde{c}_2$ in equation (4.15), we get the characteristic equation quadratic in κ,

$$\kappa^2 - \Delta\kappa - |\frac{\Omega}{2}|^2 = 0 \tag{4.18}$$

which can be solved to give solutions

$$\kappa_{\pm} = \frac{\Delta}{2} \pm \frac{\sqrt{\Delta^2 + \Omega^2}}{2}. \tag{4.19}$$

The general solutions for c_1 and $\tilde{c}_2$ can be written as

$$c_1(t) = Ae^{i\kappa_+ t} + Be^{i\kappa_- t}, \tag{4.20a}$$

$$\tilde{c}_2(t) = -\frac{2}{\Omega}(A\kappa_+ e^{i\kappa_+ t} + B\kappa_- e^{i\kappa_- t}). \tag{4.20b}$$

If we assume our initial conditions are $c_1(0) = 1$ and $c_2(0) = 0$ the coefficients A and B can be solved for then plugged back into equation (4.20) to get expressions for $c_1(t)$ and $c_2(t)$ equal to

$$c_1(t) = e^{i\Delta t/2}(\cos(\sqrt{\Delta^2 + \Omega^2}t/2) - \frac{i\Delta}{\sqrt{\Delta^2 + \Omega^2}}\sin(\sqrt{\Delta^2 + \Omega^2}t/2)), \tag{4.21a}$$

$$c_2(t) = \frac{-i\Omega}{\sqrt{\Delta^2 + \Omega^2}}e^{-i\Delta t/2}\sin(\frac{\sqrt{\Delta^2 + \Omega^2}t}{2}). \tag{4.21b}$$

The quantity measured in our experiments is the probability of finding the atom in the second state, $|c_2|^2$, which is equal to

$$|c_2(t)|^2 = \frac{\Omega^2}{\Omega^2 + \Delta^2}\sin^2(\frac{\sqrt{\Omega^2 + \Delta^2}t}{2}). \tag{4.22}$$

When the field is on resonance $\omega = \omega_0$ and $\Delta = 0$ this simplifies to the familiar

$$|c_2(t)|^2 = \sin^2(\frac{\Omega t}{2}). \tag{4.23}$$

This is the condition needed for full population transfer. More generally, we can write the evolution matrix that transforms $\mathbf{c}(t) = U(t - t_0)\mathbf{c}(t_0)$ for the vector $\mathbf{c}(t) = \begin{pmatrix} c_1 \\ c_2 \end{pmatrix}$. Setting $t_0 = 0$

$$U(t) = \begin{pmatrix} e^{i\Delta t/2}(\cos(\frac{\Omega' t}{2}) - \frac{i\Delta}{\Omega'}\sin(\frac{\Omega' t}{2})) & ie^{i\Delta t/2}\frac{\Omega*}{\Omega'}\sin(\frac{\Omega' t}{2}) \\ ie^{-i\Delta t/2}\frac{\Omega}{\Omega'}\sin(\frac{\Omega' t}{2}) & e^{-i\Delta t/2}(\cos(\frac{\Omega' t}{2}) + \frac{i\Delta}{\Omega'}\sin(\frac{\Omega' t}{2})) \end{pmatrix}, \tag{4.24}$$

where $\Omega' = \sqrt{|\Omega|^2 + \Delta^2}$. For the important case when $\Delta = 0$ this reduces to

$$U(t) = \begin{pmatrix} \cos(\frac{|\Omega| t}{2}) & i\sin(\frac{|\Omega| t}{2}) \\ i\sin(\frac{|\Omega| t}{2}) & \cos(\frac{|\Omega| t}{2}) \end{pmatrix}. \tag{4.25}$$

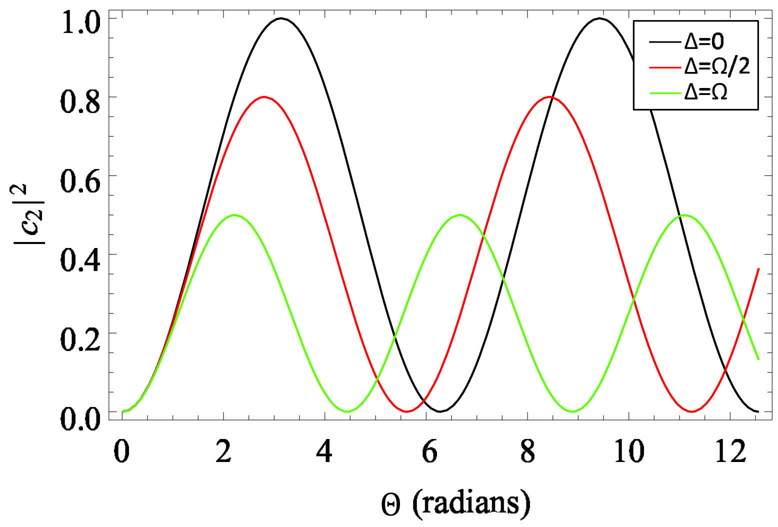

Figure 4.2: Rabi flopping at different for different field detunings. Note for full population transfer, usually needed for quantum gate operations, the detuning must be equal to 0.

Relating this to equation (4.4a) for single qubit gates, note that $\theta = |\Omega|t$. If we apply the field, Ω, for a time $t = \frac{\pi}{|\Omega|}$ we recover, up to an overall phase, an X-gate also known as a Not-gate also known as a π -pulse

$$U_\pi = \begin{pmatrix} 0 & -i \\ -i & 0 \end{pmatrix} . \tag{4.26}$$

Applying the field for a time $t = \frac{\pi}{2|\Omega|}$ will result in a $\pi/2$-pulse which puts the state vector on the equator of the Bloch sphere if it started at the poles,

$$U_{\pi/2} = \frac{1}{\sqrt{2}} \begin{pmatrix} 1 & i \\ i & 1 \end{pmatrix} . \tag{4.27}$$

Finally for a time $t = \frac{2\pi}{|\Omega|}$ the result is a 2π-pulse which rotates the vector around the Bloch sphere back to where it started but with an overall phase shift,

$$U_{2\pi} = - \begin{pmatrix} 1 & 0 \\ 0 & 1 \end{pmatrix} . \tag{4.28}$$

Y-gates or any gate that is a rotation about some axes in the x-y plane of the Bloch sphere are executed in similar ways but with a phase shift added to the driving field, eg a phase shift of $\pi/2$ for the Y-gate.

Rotations about the z-axis are implemented in two distinct ways. From reference [62] we know that any single qubit gate can be decomposed into three rotations about two non-parallel axes plus some overall phase

$$U = e^{i\alpha} R_{\hat{n}}(\beta) R_{\hat{m}}(\gamma) R_{\hat{n}}(\delta) \tag{4.29}$$

where the most general rotation about an axis $\hat{n} = (n_x, n_y, n_z)$ is $R_{\hat{n}}(\theta) = \cos\left(\frac{\theta}{2}\right) I - i \sin\left(\frac{\theta}{2}\right)(n_x\sigma_x + n_y\sigma_y + n_z\sigma_z)$. As mentioned above it is straight-forward to change the phase of the driving field and thus the rotation axis in the x-y plane. It will be most convenient for us to therefore decompose rotations about the z-axis into three rotations about the $X = R_{\phi=0}(\theta)$ and $Y = R_{\phi=\pi/2}(\theta)$ axes

$$R_z(\theta) = e^{i\alpha} R_x(\beta) R_y(\gamma) R_x(\delta). \tag{4.30}$$

For example, if we wanted to perform a π rotation about the z-axis we can decompose this as

$$R_z(\pi) = R_x(3\pi/2) R_y(\pi) R_x(\pi/2). \tag{4.31}$$

A $\pi/2$ rotation about the z-axis would be decomposed as

$$R_z(\pi) = R_x(\pi/2) R_y(3\pi/2) R_x(3\pi/2). \tag{4.32}$$

Alternatively, rotating the qubit about the z-axis amounts to controlling the phase between the qubit basis states. In other words a z-gate can be implemented by applying the unitary

$$\begin{pmatrix} 1 & 0 \\ 0 & e^{i\phi} \end{pmatrix}. \tag{4.33}$$

ϕ is controlled by introducing a known differential Stark shift, δ, between the two states, resulting in a phase shift $\phi = \delta t$. This shift is found experimentally using Ramsey oscillations and will be discussed in detail later in this thesis.

4.2 Global Rotations Using Microwaves

Microwaves are used to directly drive the hyperfine transition. This transition is an M1 magnetic dipole transition. The derivation in section 4.1 is still valid but the interaction Hamiltonian needs to be replaced with $H_I = -\mu \cdot \mathbf{B}$. Instead of an electric dipole coupling to the oscillating electric field, the magnetic dipole, μ, is coupled to the oscillating magnetic field, **B**, in the microwave field and the Rabi frequency becomes $\Omega = \frac{\langle 1|\mu B|2\rangle}{\hbar}$. We use microwaves tuned to the 9.2 GHz hyperfine splitting to perform single qubit operations on all qubits simultaneously.

A 9 GHz RF signal from an synthesized sweeper[1] is mixed with a 200 MHz signal from a DDS board. The synthesized sweeper is referenced to a stable 10 MHz GPS signal. This signal also is used as a reference for another synthesized sweeper tuned to 1 GHz used as a stable reference for the DDS. Two DDS channels are used which allows storage of up to 16 profiles which store the frequency, phase and amplitude information. An RF switch is used to switch between the two DDS channels. This signal is then sent to a voltage controlled attenuator (VCA) controlled by an analog noise eater device which outputs a voltage dependent on a power level reading picked off by a detector down stream in the electronics path. This feedback loop is used to stabilize the RF intensity. A mixer[2] mixes the voltage controlled 200 MHz signal with the 9 GHz signal. This mixing will allow us to control the phase of the RF field by trivially changing the phase output of the DDS. Phase control allows for rotations around arbitrary axes as mentioned in section 4.1. After the mixer the RF signal consists of the 9 GHz carrier frequency along with the 9 GHz±200 MHz side band frequencies. This signal is pre-amplified by a 24 dB mini-circuits amplifier and then is sent through an isolator before being sent through a high power filter which only passes the 9.2 GHz side band. This signal is finally amplified by a 35 dB, 3 W amplifier before being sent to a microwave horn which is directed onto the atoms. This set-up is shown schematically in Fig. 4.3

Fig. 4.4 shows an example of a microwave spectroscopy experiment where the pulse area is fixed and the detuning from unperturbed clock frequency is scanned. We expect a differential shift of about -630 Hz from the 780 nm trapping light. Measuring this differential shift across the array we see an average shift of -260 Hz with a standard deviation of 400 Hz. If we tuned our microwave frequency to this average some sites can be 400 Hz detuned. At ~10 kHz Rabi frequency that

---

[1] HP 83623A

[2] mini-circuits ZMX-10G+

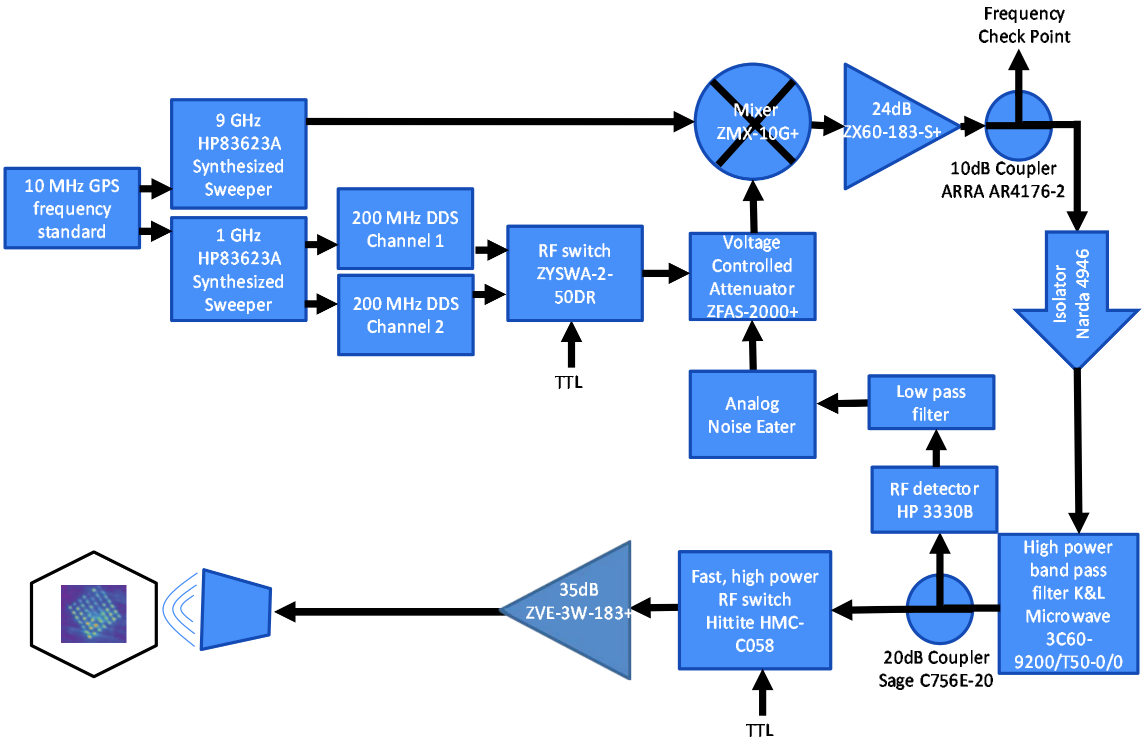

Figure 4.3: Schematic for microwave control electronics. A 9 GHz Synthesize Sweeper is combined with a 200 MHz signal created by a DDS on a mixer before eventually being amplified and sent to the atoms via a microwave horn. This set-up allows for full frequency, amplitude and phase control of the microwave field driving single qubit rotations.

would translate into a rotation error of $1 - \frac{10^2}{10^2 + .4^2} = 0.0016$ It is possible to compensate for this using composite pulse techniques discussed in section 4.6.

Also seen in the figure is an example of Rabi flopping experiments. The spread of Rabi frequencies across the array is due to both inhomogeneities in the driving fields and difference in the qubit frequencies discussed above. Its also possible to compensate for these using composite pulse techniques. The average amplitude is consistent with the pumping fidelity measurement of the previous chapter given the average depumping and pumping times.

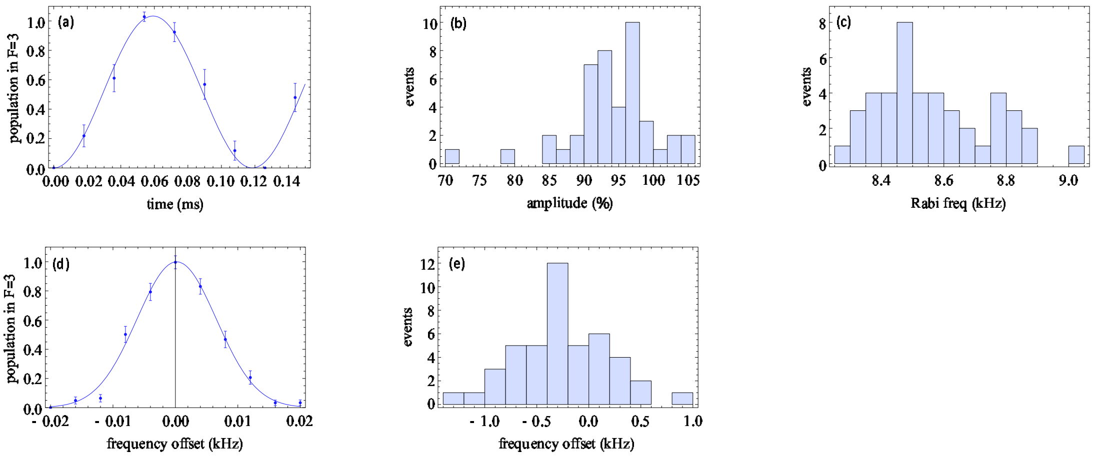

Figure 4.4: (a) Representative data of a microwave Rabi flopping experiment on a single site. Experiments as seen in (a) are done on all sites simultaneously. From the fits, array statistics are extracted. (b) Array statistics for the microwave Rabi flopping amplitude. The average amplitude across the array is 0.94 with a stand deviation of 0.063. RFE data from 2014_07_28_07_18_21. (c) Array statistics for the microwave Rabi frequency shows an average of 8.6 kHz with a standard deviation of 0.18 kHz. (d) Representative data of a microwave Rabi spectroscopy experiment on a single site. The microwave frequency is scanned from the unperturbed Clock frequency using a microwave pulse with fixed area. (e) The average frequency shift across the array is measured to be 0.26 kHz with a stand deviation of 0.44 kHz. Spectroscopy data from 2014_09_11_17_49_58.

4.3 Single Site Rotations Using Microwaves

Our microwave source is extremely robust and does not require precise alignments, locks or any sort of day to day maintenance unlike our complicated laser systems. We would prefer to use the microwaves for all single qubit rotations however the microwave field cannot be focused down to the micron level needed for single qubit manipulation. Here we add a tightly focused Stark shifting beam to achieve this. This beam adds a differential shift to the ground state of a single site. If the microwaves are tuned to be resonant with the remaining un-shifted sites the microwave pulses can be used to rotate all but the single differentially shifted site. Alternatively, the microwaves can be tuned to the differentially shifted frequency and then rotations are performed on just the single site.

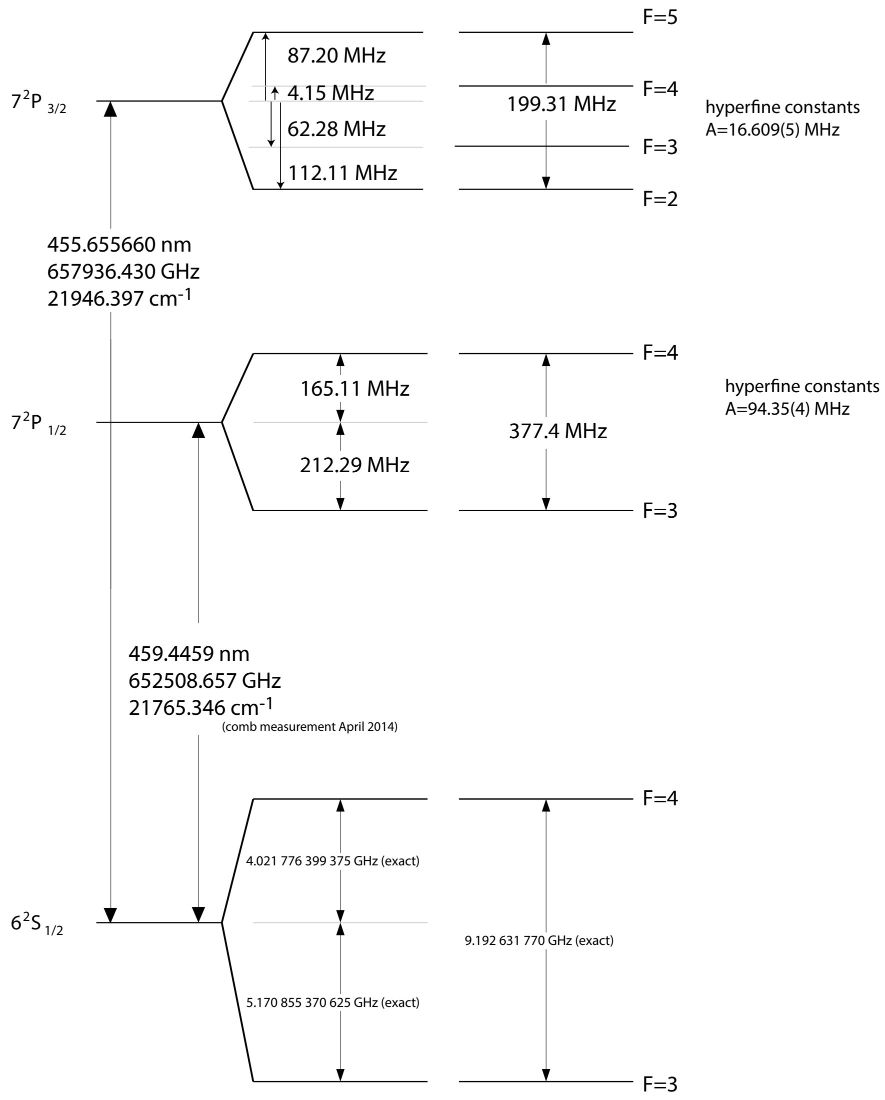

Figure 4.5: Atomic structure of the Cs $7p_{1/2}$ resonance. We use this transition throughout this thesis for implementing both single site Stark shifting as explained here and for Rydberg excitation, explained in Chapter 5.

The latter will require the laser to be more stable than the former as any drift in the intensity will change the effective qubit frequency.

We implement the single site Stark shifting using the Rydberg A laser. This laser will be fully discussed in the next chapter in the context of Rydberg excitations needed for two qubit operations. The laser operates at 459 nm with a typical detuning, $\Delta_1 \sim -2\pi \times 2$ GHz, detuned from the center of mass of the $7p_{1/2}$ level. The structure of the $7p_{1/2}$ level can be seen in Fig. 4.5. The differential shift is calculated by considering the resonant Stark shift on each of the hyperfine ground states. For $|f = 4\rangle$ this shift is equal to $\frac{1}{4}\frac{\Omega_1^2}{\Delta_1}$ where Ω_1 is the single photon Rabi frequency and Δ_1 is the detuning from the $7p_{1/2}$ level. The shift on $|f = 3\rangle$ is then $\frac{1}{4}\frac{\Omega_1^2}{\Delta_1 - \omega_{\rm HF}}$ where $\omega_{\rm HF} = 9.2$ GHz is the hyperfine splitting. These equations are only valid when Δ_1 is large compared to the hyperfine splitting on the $7p_{1/2}$ level. Within this hyperfine manifold the relative detunings of the two hyperfine states from the center of mass is equal to

$$\Delta_{f_p} = \frac{A}{2}[f_p(f_p + 1) - I(I + 1) - j_p(j_p + 1)], \tag{4.34}$$

where A is the magnetic dipole hyperfine constant equal to 94.35 MHz. For the relevant quantum numbers $f_p = 3, 4$, $I = 7/2$ and $j_p = 1/2$, $\Delta_{f_3} = -2\pi\times -212.3$ MHz and $\Delta_{f_4} = 2\pi\times 165.1$ MHz. The Rabi frequency is equal to

$$\Omega^{f_p}_{f_g,m_{f_g},q_1} = \Omega_1' \tilde{\Omega}^{f_p}_{f_g,m_{f_g},q_1}, \tag{4.35}$$

after the matrix element has been reduced via the Wigner-Eckart theorem to an angular factor times a radial matrix element such that

$$\Omega_1' = \frac{eE_1\langle n_pL_pSJ_p||r||n_gL_gSJ_g\rangle}{\hbar}. \tag{4.36}$$

For the transition from the ground state to the $7p_{1/2}$ level in cesium the reduced matrix element is[63]

$$\langle 7p_{1/2}||r||6s_{1/2}\rangle = 0.276a_0, \tag{4.37}$$

where a_0 is the Bohr radius. The angular factors are computed as

$$\tilde{\Omega}^{f_p}_{f_g,m_{f_g},q_1} = c^{j_p,f_p}_{I,j_g,f_g} C^{f_p,m_{f_g}+q_1}_{f_g,m_g,1,q_1},$$

where $C^{\cdot\cdot}_{\cdot\cdot\cdot\cdot}$ is a Clebsch-Gordon coefficient and

$$c^{j_1,I,f_1}_{j_2,I,f_2} = (-1)^{1+I+f_1+j_2}\sqrt{2f_1 + 1}S^{j_1,I,f_1}_{f_2,1,j_2}, \tag{4.38}$$

where $S^{\cdots}_{\cdots}$ is the 6j symbol. We take hyperfine clock states, $m_{f_g} = 0$, and $q_1 = 1$ is the angular momentum quantum number for the photon. The relevant factors can be computed

$$\begin{aligned}\tilde{\Omega}^4_{4,0,1} =& -\sqrt{5/48},\\ \tilde{\Omega}^4_{3,0,1} =& \sqrt{5/48},\\ \tilde{\Omega}^3_{4,0,1} =& -1/4,\\ \tilde{\Omega}^3_{3,0,1} =& 1/4.\end{aligned} \tag{4.39}$$

The Stark shifts on each of the ground states are computed by summing over the hyperfine states of the $7p_{1/2}$ including the relative detunings

$$\begin{aligned}\Delta_{\text{ac},3} =& (\frac{\Omega^3_{3,0,1}}{2})^2 \frac{1}{\Delta_1 - \Delta_{f_3} - \omega_q} + (\frac{\Omega^4_{3,0,1}}{2})^2 \frac{1}{\Delta_1 - \Delta_{f_4} - \omega_q},\\ \Delta_{\text{ac},4} =& (\frac{\Omega^3_{4,0,1}}{2})^2 \frac{1}{\Delta_1 - \Delta_{f_3}} + (\frac{\Omega^4_{4,0,1}}{2})^2 \frac{1}{\Delta_1 - \Delta_{f_4}}.\end{aligned} \tag{4.40}$$

Using the angular factors from above, the differential shift can be written as

$$\Delta^0_{\text{diff}} = \frac{|\Omega_1'|^2}{64}\left[\frac{5/3}{\Delta_1 - \Delta_{f_4}} + \frac{1}{\Delta_1 - \Delta_{f_3}} - \frac{5/3}{\Delta_1 - \Delta_{f_4} - \omega_q} - \frac{1}{\Delta_1 - \Delta_{f_3} - \omega_q}\right]. \tag{4.41}$$

To write Ω_1' in convenient units express the field, E_1, in terms of the beam power, P_{459}, and beam waist, w_{459},

$$E_1 = \sqrt{\frac{4}{\epsilon_0 c}\frac{P_{459}}{\pi w_{459}^2}}. \tag{4.42}$$

For $w_{459} = 3$ μm and $P_{459} = 66$ μW, which are typical parameters used in the Rydberg experiments described in the next chapter, the single site differential shift, Δ^0_{diff}, would be around 680 kHz. If we used this beam to shift one site off of resonance and then rotate all other sites with a microwave π-pulse we would expect a rotation error on this site, given a 10 kHz microwave Rabi frequency, to be $\frac{10^2}{10^2+680^2} = 2\times10^{-4}$. At this point, however spontaneous emission from the $7p_{1/2}$ level becomes important. The scattering rate is equal to

$$\Gamma_{7p_{1/2}} = \frac{\gamma_p |\Omega_1'|^2}{32}\left(\frac{1}{(\Delta_1 - \Delta_{f_3})^2} + \frac{5/3}{(\Delta_1 - \Delta_{f_4})^2}\right), \tag{4.43}$$

where $\gamma_p = 2\pi \times 0.94$ MHz is the radiative decay rate of the $7p_{1/2}$ state. In the time it takes to complete a microwave π-pulse the probability of scattering a photon is 22% for the parameters

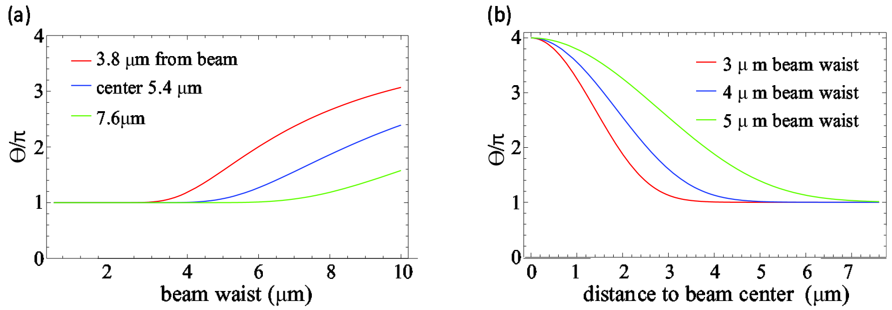

Figure 4.6: (a)Rotation on a neighboring, non-addressed site as a function of beam waist for fixed distances. (b)Rotation on a neighboring, non-addressed site as a function of distance from the intended site for fixed beam waists.

defined above. This will obviously be a problem as it will cause decoherence of our qubit state so we need to decrease Ω_1 by decreasing P_{459}. We can also increase Δ_1 for the same effect but as stated earlier, this is fixed for Rydberg experiments. The goal is to minimize spontaneous emission and the off-resonant rotation errors simultaneously. One strategy is to find a detuning which gives a 2π off-resonant rotation on the Stark shifted site when a $\pi/2$ resonant rotation is applied to the other sites. From equation (4.22) we set up the condition to satisfy

$$\sqrt{\Omega_{\mu\mathrm{W}}^2 + (\Delta_{\mathrm{diff}}^0)^2}\frac{\pi}{2\Omega_{\mu\mathrm{W}}} = 2\pi. \tag{4.44}$$

Here $\Omega_{\mu\mathrm{W}}$ is fixed by the microwave power and is ∼10 kHz. We solve this equation and find a solution $(\Delta_{\mathrm{diff}}^0)^2 = 15\Omega_{\mu\mathrm{W}}^2$. This means if we set our differential Stark shift, Δ_{diff}^0, to be $\sqrt{15}\Omega_{\mu\mathrm{W}} \approx$ 39 kHz, $\pi/2$-pulses on the non-Stark shifted sites will lead to 2π rotations on the shifted site. Similarly at this detuning π-pulses on non-shifted sites will give $\sqrt{\Omega_{\mu\mathrm{W}}^2 + 15\Omega_{\mu\mathrm{W}}^2}\frac{\pi}{\Omega_{\mu\mathrm{W}}} = 4\pi$ rotations on the Stark shifted site. More analysis of this can be found in the reference [53].

This 39 kHz shift is 17 times smaller than the shift estimated for the full power case which means the spontaneous emission probability drops to $\sim 1\%$. Consider what happens on a neighboring site. We know that the differential shift scales with the single photon Rabi frequency squared or $\Delta_{\mathrm{diff}}^0 \sim \Omega_1^2$. Until now we have assumed a constant shift at peak intensity, $I_0 = \frac{2P}{\pi w^2}$, but in reality the shift has some position dependence. For a Gaussian beam this is $I = I_0 e^{-2r^2/w^2}$ where r is some radial position from the beam center and w is the beam waist. Then $\Omega_1(r)$ can be written

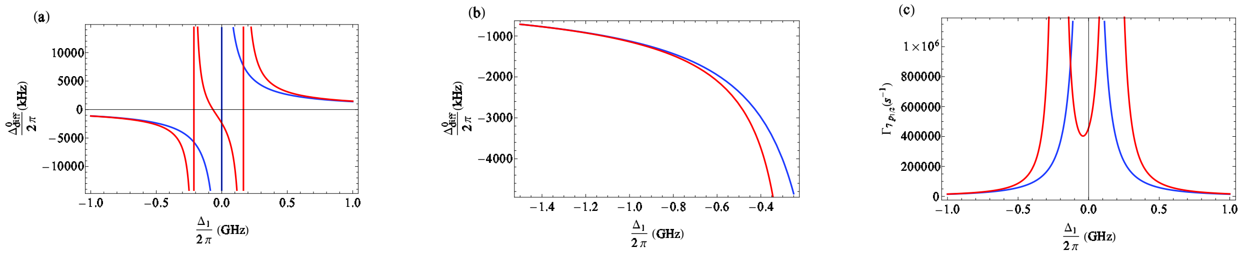

Figure 4.7: Using parameters chosen to be approximately equal to experimental parameters ($P_{459} = 45\mu$W, $w_{459} = 3\mu$m, and $q = +1$), the differential Stark shift and photon scattering rate from the intermediate level are calculated using both the full hyperfine structure of the $7p_{1/2}$ level (red) and the fine structure approximation (blue). (a) The differential shift on the ground state is calculated as a function of the detuning using both methods. (b) Zooming in on the region where the two curves converge. After $\frac{\Delta_1}{2\pi} \sim 1$ GHz the fine structure approximation becomes valid. (c) Calculation of the photon scattering rate using both methods.

as

$$\Omega_1(r) = \Omega_1^0 e^{-r^2/w^2}, \tag{4.45}$$

where Ω_1^0 is the Rabi frequency at $r = 0$. The differential shift as a function of r is then

$$\Delta_{\rm diff}(r) =\equiv \Delta^0_{\rm diff} e^{-2r^2/w^2}. \tag{4.46}$$

If we choose $\Delta^0_{\rm diff} = \sqrt{15}\Omega_{\mu\rm W}$ then we can calculate what off-resonant rotation we would expect on the neighboring sites. For a resonant π-rotation this is equal to

$$\Theta_{\rm x-talk} = \sqrt{\Omega^2_{\mu\rm W} + 15\Omega^2_{\mu\rm W} e^{-2r^2/w^2}}\,\frac{\pi}{\Omega_{\mu\rm W}}. \tag{4.47}$$

Plotted in Fig. 4.6 (b) is the off-resonant rotation in units of π for fixed beam waists as a function of distance from the beam center for a π-pulse. Fig. 4.6 (a) shows the off-resonant rotation as a function of beam waist for a fixed distances.

To demonstrate the importance of using the full hyperfine calculations found in equations (4.41) and (4.43), Fig. 4.7 shows calculations of $\Delta^0_{\rm diff}$ and of the photon scattering rate, $\Gamma_{7p_{1/2}}$, using the full hyperfine equations(red curves) and the fine structure approximation (blue). Note the convergence of the two around $\frac{\Delta_1}{2\pi} = 1$ GHz.

4.3.1 State Preparation

Using the techniques described above we can measure how well we prepare the two qubit computational basis states. $|11\rangle$ is prepared by optically pumping into $|f = 4; m_f = 0\rangle$. $|00\rangle$ is prepared by pumping into $|f = 4; m_f = 0\rangle$ and applying a global microwave π-pulse such that all sites are rotated to $|f = 3; m_f = 0\rangle$. $|10\rangle$ is prepared by applying the Stark shifting beam to the first site while applying a π-pulse following the optical pumping phase. This will put all sites not interacting with the Stark shifting beam into $|f = 3; m_f = 0\rangle$. The intensity of the Stark shifting beam will differentially shift the first site in such a way that in the time it takes all other sites to complete a π rotation, site one will finish a 2π rotation returning it to $|f = 4; m_f = 0\rangle$ resulting in the two qubit state $|10\rangle$. $|01\rangle$ is prepared in a similar way this time Stark shifting the second site. These are the states needed for implementation of the gate so evaluation of this state preparation is an important diagnostic. An example of this is seen is Fig. 4.8.

4.4 Measurement of Decoherence and Dephasing

The microwaves are used for single qubit rotations but they are useful for studying the coherence properties of our qubits. Typically, two characteristic times, T_1 and T_2^*, are used to for this characterization. The T_1 time is called the longitudinal relaxation time and describes the population decay of the either qubit states. T_2^* is the decay of the phase coherence between the two qubit states.

4.4.1 T_1

To measure T_1 the atom is pumped into either qubit state. The time it takes to decay out of that state is measured by varying the time between state preparation and measurement. Specifically, T_1 is measured after pumping all of the sites into $|f = 4; m_f = 0\rangle$. After waiting for some variable time, a microwave π-pulse is applied followed by the blow away of $|f = 4\rangle$ for state detection. The atoms that have been depumped due to the finite T_1 will be ejected from the traps resulting in a decay of the signal as a function of time. Alternatively, T_1 of the $|f = 3; m_f = 0\rangle$ state is measured by applying the microwave π-pulse right after the optical pumping phase and before the

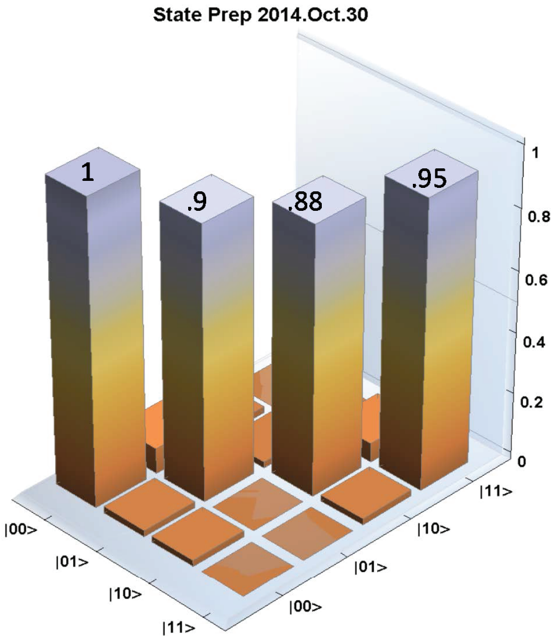

Figure 4.8: State preparation demonstration of the four 2 qubit computational basis states. Data combined from $2014\_10\_30\_08\_25\_49$, $2014\_10\_30\_08\_50\_14$, $2014\_10\_30\_09\_14\_01$, and $2014\_10\_30\_09\_39\_25$.

variable delay time. This will also show a decay as a function of time of the $|f = 3; m_f = 0\rangle$ state due to the finite T_1. The signals are fitted to a, e^{-t/T_1}, and T_1's are extracted.

Ideally, T_1 should be sufficiently long such that only trap loss is seen, on times scales on the order of a few seconds, due to collisions with hot background atoms. In reality, we measure about 0.5 s which is about a factor of 10 lower than the measured trap lifetime. We think this is due to Raman scattering from the trap light or leakage from the cooling and repumper light. While this is clearly less than ideal, it is still much longer than the time needed to run the gate and the coherence time, as will be demonstrated in the section that follows.

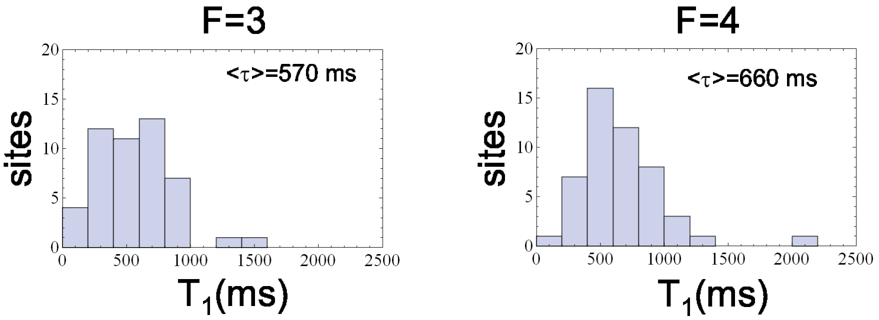

Figure 4.9: Measured T_1 times in 49 site array for each basis state. Data from 2013_04_26_17_16_24 and 2013_04_29_17_35_06.

T_1 is a useful diagnostic for measuring beam leakage onto the atoms. The cooling light is switched off using AOMs by switching off the RF power. This puts all of the power into the 0^{th} diffraction order of the AOM. It's possible that the 0^{th} order can still be coupled to the fiber so in addition to switching the AOMs, piezo shutters are added to physically block the light. If T_1 for $|f = 4\rangle$ is very short this is a sign that there is light leaking through that is depumping the atom to $|f = 3\rangle$ which can be traced back to either 852 nm cooling light or 894 nm pumping light. If the $|f = 3\rangle$ T_1 time is very short this is a sign of repumper light leaking. If this is the case the alignment or timing of the shutters should be checked.

4.4.2 T_2^*

To measure T_2^*, we use the microwaves to do a Ramsey type sequence. In the language of the Bloch vector, the initial state of a single atom is (0,0,-1) after optical pumping. A $\pi/2$-pulse is applied which rotates the Bloch vector to the (0,1,0) equator state. Here the Bloch vector freely precesses around the equator at an angular frequency equal to the detuning, δ, and then another $\pi/2$-pulse is applied after some time, t. After this pulse sequence we expect the probability amplitude to evolve as

$$c_2(t) = \cos(\delta t), \tag{4.48}$$

where $\delta = \omega - \omega_0$ is the detuning of the microwave radiation, ω, from the atomic resonance, ω_0. The microwaves induce no Stark shift on the atoms so to ensure a measurable precession they must be detuned by a small amount so that $\omega = \omega_{\text{HF}} + \delta_{\text{synth}}$. Alternatively, the phase of the second pulse can be varied at a fixed delay time. In this situation, we tune the microwaves to be resonant with the atoms but there is still a small calibration error from the synthesizer, δ_{synth}.

External perturbations will modify the atomic resonance ω_0 so that

$$\omega_0 = \omega_{\text{HF}} + \delta_{\text{ls}} + \delta_{\text{B}}, \tag{4.49}$$

where δ_{ls} is the energy dependent differential light shift from the trap light and δ_{B} is the quadratic Zeeman shift.

The 780 nm light used for trapping is blue-detuned from the D-line of Cesium. This will cause the ground state to shift to higher energy which is why higher intensity repels the atom. Because of the 9.2 GHz hyperfine ground state splitting, the $|f = 3\rangle$ level is shifted up by a larger amount than the $|f = 4\rangle$. This will result in a qubit frequency smaller than the free space frequency, ω_{HF}. The difference in these two frequencies is the differential light shift which has position dependence due to the spatial structure of the traps. An atom at the exact center of the trap should have a minimal shift but since the atom has a finite temperature is moves around the trap sampling different amounts of trap light which therefore causes fluctuations in the qubit frequency. The average shift is related to the atoms average energy which can be related to atom temperature. The reversible dephasing time, T_2^*, is inversely proportional to the atom temperature[64]

$$T_2^* = 0.97\frac{2\hbar}{\eta k_{\text{B}} T_a}, \tag{4.50}$$

for T_a the atom temperature and $\eta = \frac{\omega_{\text{HF}}}{\Delta_{\text{eff}}}$ where Δ_{eff} is the effective detuning of the trapping light taking into account the weighted contributions of the D_1 and D_2 lines.

To measure this time, the sequence of $\pi/2$-pulses is applied at several delay times. Fig. 4.10 shows an example of the Ramsey experiments on a single site with varying delay times. Note the amplitudes decreasing with increasing delay time. The amplitudes are extracted at each delay time, as seen in Fig. 4.11 (a) for a single site, and are fitted with a decaying exponential. Fig. 4.11 (b) shows the results of the extracted decay times for the sites in the array. For this data set the average time is 5.9 ms. Site to site differences in trap structure caused by slight misalignments will cause site to site variations in the light shift experienced by the atoms. Furthermore, interference

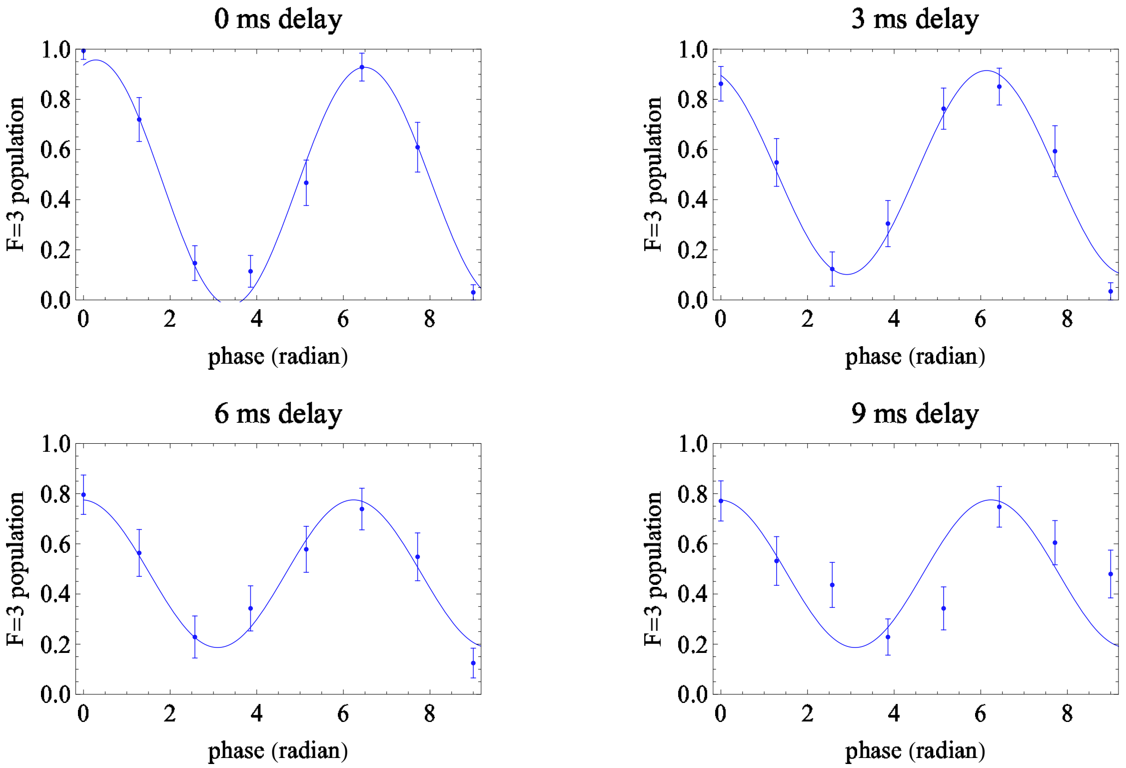

Figure 4.10: Ground state Ramsey experiments at different delay times. Data from 2014_10_02_12_52_42, 2014_10_02_13_11_11, 2014_10_02_13_28_29, and 2014_10_02_13_40_48.

patterns formed by the MOT beams can cause site to site variations in the cooling efficiency. These effects can explain the spread of T_2^* seen in Fig. 4.11 (b). Trap compensation techniques will be implemented in the future and should allow for substantial improvements in the T_2^* times [59, 60]. These times can be converted into temperatures via equation (4.50). For this data set the average temperature is 15μK with a standard deviation of 8μK. This closely agrees with the drop and recapture measurements of Chapter 3 which predicted an atom temperature between $10 - 20\mu$k.

4.5 Randomized benchmarking of single qubit gates

The characterization of single qubit gate errors is an important step on the road towards fault tolerant quantum computing. The error threshold theorem says that if the errors per gate are small enough then arbitrarily accurate computations are possible using quantum error correction [65]. We characterize the errors of our single qubit gates using randomized benchmarking (RB). RB was

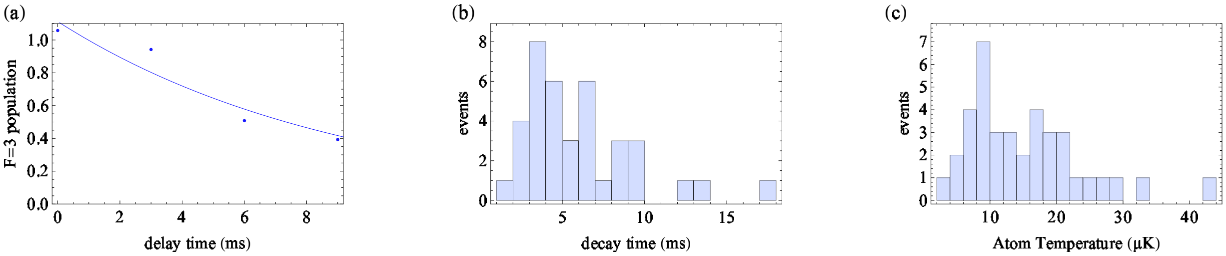

Figure 4.11: (a) Representative single site data which shows the fitted Ramsey amplitudes as a function of delay time with a fit which gives a decay time of 8.7 ms. (b) Results of these fitted decay times across the array, gives an average time of 5.9 ms with a standard deviation of 3.4 ms. (c)Converting the T_2 times in (b) into atom temperatures using equation (4.50). The average temperature is 15μK with a standard deviation of 8μK.

first developed and implemented in ion systems [66] and it is an efficient way of the evaluating the errors of gate operations. Random Clifford gate sequences of varying lengths, l, are applied to a fixed input state, $|1\rangle$. Single qubit Clifford gates are generated by the set $\{I, R_i(\pm\pi/2), R_i(\pi))\}$ of which there are 24 in total. The 24 gates are specified in Table 4.1 along with the microwave rotations needed to implement each gate. The average pulse area per gate is $7\pi/4$.

At the end of each sequence a final gate is added which puts the qubit into $|0\rangle$ in the absence of errors. In the presence of de-polarization errors[3] the probability of measuring $|0\rangle$ is

$$P_{|0\rangle} = \frac{1}{2} + \frac{1}{2}(1 - d_{\text{if}})(1 - d)^l, \tag{4.51}$$

where d_{if} is the de-polarization probability associated with state preparation and measurement and d is the average de-polarization of a Clifford gate. Applying several of these randomized gate sequences while varying l one can extract a value for d. This is done simultaneously on all sites using the microwaves pulses. Defining the fidelity in the usual way, $F(\rho, \rho') = Tr[\sqrt{\sqrt{\rho}\rho'\sqrt{\rho}}]$, one can show that the square of the average gate fidelity is related to d by $F^2 = 1 - d/2$. We measure the average F^2 across the array to be 0.9983(14) [53]. Based on estimated values of detuning errors (100 Hz) and pulse length errors (25 ns), the dominant factor limiting the gate fidelity is thought to be due to the T_2^* times. As was discussed in section 4.4.2, this can be extended

---

[3] These errors are equivalent to applying an X,Y,Z or I gate to the state randomly with equal probability.

index	x axis	y axis	z axis	U	R_3	R_2	R_1	θ_{total}
1	I	I	I	$\begin{pmatrix}1 & 0\\0 & 1\end{pmatrix}$	-	-	-	0
2	I	I	$\pi/2$	$e^{-\imath\pi/4}\begin{pmatrix}1 & 0\\0 & i\end{pmatrix}$	$R_x(\pi/2)$	$R_y(\pi/2)$	$R_x(3\pi/2)$	$5\pi/2$
3	I	I	π	$-i\begin{pmatrix}1 & 0\\0 & -1\end{pmatrix}$	-	$R_x(\pi)$	$R_y(\pi)$	2π
4	I	I	$-\pi/2$	$e^{\imath\pi/4}\begin{pmatrix}1 & 0\\0 & -i\end{pmatrix}$	$R_x(\pi/2)$	$R_y(3\pi/2)$	$R_x(3\pi/2)$	$7\pi/2$
5	I	π	I	$-1\begin{pmatrix}0 & 1\\-1 & 0\end{pmatrix}$	-	-	$R_y(\pi)$	π
6	I	π	$\pi/2$	$-e^{\imath\pi/4}\begin{pmatrix}0 & 1\\i & 0\end{pmatrix}$	$R_x(\pi/2)$	$R_y(\pi/2)$	$R_x(\pi/2)$	$3\pi/2$
7	π	I	I	$-i\begin{pmatrix}0 & 1\\1 & 0\end{pmatrix}$	-	-	$R_x(\pi)$	π
8	π	I	$\pi/2$	$e^{-\imath\pi/4}\begin{pmatrix}0 & 1\\-i & 0\end{pmatrix}$	$R_x(\pi/2)$	$R_y(3\pi/2)$	$R_x(\pi/2)$	$5\pi/2$
9	π	$\pi/2$	I	$\frac{-i}{\sqrt{2}}\begin{pmatrix}1 & 1\\1 & -1\end{pmatrix}$	-	$R_x(\pi)$	$R_y(\pi/2)$	$3\pi/2$
10	I	$-\pi/2$	I	$\frac{1}{\sqrt{2}}\begin{pmatrix}1 & 1\\-1 & 1\end{pmatrix}$	-	-	$R_y(3\pi/2)$	$3\pi/2$
11	$\pi/2$	I	$\pi/2$	$\frac{e^{-\imath\pi/4}}{\sqrt{2}}\begin{pmatrix}1 & 1\\-i & i\end{pmatrix}$	-	$R_y(3\pi/2)$	$R_x(\pi/2)$	2π
12	$\pi/2$	π	$\pi/2$	$-\frac{e^{\imath\pi/4}}{\sqrt{2}}\begin{pmatrix}1 & 1\\i & -i\end{pmatrix}$	-	$R_y(3\pi/2)$	$R_x(3\pi/2)$	3π
13	π	$-\pi/2$	I	$\frac{i}{\sqrt{2}}\begin{pmatrix}1 & -1\\-1 & -1\end{pmatrix}$	-	$R_x(\pi)$	$R_y(3\pi/2)$	$5\pi/2$
14	$-\pi/2$	I	$\pi/2$	$\frac{e^{-\imath\pi/4}}{\sqrt{2}}\begin{pmatrix}1 & -1\\i & i\end{pmatrix}$	-	$R_y(\pi/2)$	$R_x(3\pi/2)$	2π
15	I	$\pi/2$	I	$\frac{1}{\sqrt{2}}\begin{pmatrix}1 & -1\\1 & 1\end{pmatrix}$	-	-	$R_y(\pi/2)$	$\pi/2$
16	$-\pi/2$	π	$\pi/2$	$\frac{e^{\imath\pi/4}}{\sqrt{2}}\begin{pmatrix}1 & -1\\-i & -i\end{pmatrix}$	-	$R_y(\pi/2)$	$R_x(\pi/2)$	π
17	$-\pi/2$	$-\pi/2$	I	$\frac{e^{-\imath\pi/4}}{\sqrt{2}}\begin{pmatrix}1 & i\\-1 & i\end{pmatrix}$	-	$R_x(3\pi/2)$	$R_y(3\pi/2)$	3π
18	$-\pi/2$	$\pi/2$	I	$\frac{e^{\imath\pi/4}}{\sqrt{2}}\begin{pmatrix}1 & i\\1 & -i\end{pmatrix}$	-	$R_x(3\pi/2)$	$R_y(\pi/2)$	2π
19	$-\pi/2$	π	I	$\frac{i}{\sqrt{2}}\begin{pmatrix}1 & i\\-i & -1\end{pmatrix}$	-	$R_x(3\pi/2)$	$R_y(\pi)$	$5\pi/2$
20	$-\pi/2$	I	I	$\frac{1}{\sqrt{2}}\begin{pmatrix}1 & i\\i & 1\end{pmatrix}$	-	-	$R_x(3\pi/2)$	$3\pi/2$
21	$\pi/2$	$-\pi/2$	I	$\frac{e^{\imath\pi/4}}{\sqrt{2}}\begin{pmatrix}1 & -i\\-1 & -i\end{pmatrix}$	-	$R_x(\pi/2)$	$R_y(3\pi/2)$	2π
22	$\pi/2$	I	I	$\frac{1}{\sqrt{2}}\begin{pmatrix}1 & -i\\-i & 1\end{pmatrix}$	-	-	$R_x(\pi/2)$	$\pi/2$
23	$\pi/2$	π	I	$\frac{-i}{\sqrt{2}}\begin{pmatrix}1 & -i\\i & -1\end{pmatrix}$	-	$R_x(\pi/2)$	$R_y(\pi)$	$3\pi/2$
24	$\pi/2$	$\pi/2$	I	$\frac{e^{-\imath\pi/4}}{\sqrt{2}}\begin{pmatrix}1 & -i\\1 & i\end{pmatrix}$	-	$R_x(\pi/2)$	$R_y(\pi/2)$	π

Table 4.1: Elements of the Clifford group for a single qubit. The sequence of rotations about the x-, y- and z-axes results in the operator U which is implemented with the microwaves using $R_3R_2R_1$, up to an overall phase. The average total rotation is $7\pi/4$.

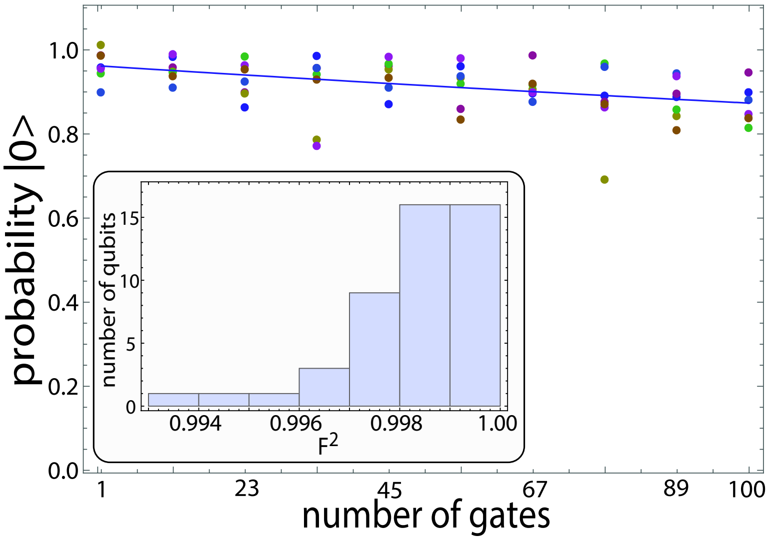

Figure 4.12: Probability of measuring the correct output state at site 27 of the array for 7 RB sequences. The inset shows a histogram of gate fidelities for 47 of the 49 array sites. Two sites were dropped due to poor loading statistics.

by implementing trap compensation techniques along with improving the cooling of the atoms in the traps. Increasing our microwave power and thus our microwave Rabi frequency[4] as well replacing all $3\pi/2$-pulses with $-\pi/2$-pulses will also improve this T_2^* limited gate fidelity. Fig. 4.12 shows the probability of measuring the correct output state for 7 RB sequences on a single representative site along with a histogram of the gate fidelities for 47 sites of the array. Similar experiments are done to test the single site gate fidelity using a Stark shifting beam, as described in section 4.3, that is -20 GHz detuned from the $7p_{1/2}$ line. A single site is shifted by 33 kHz and the microwaves are detuned to match this shift so that only one site on resonance. Note this is the opposite of what was described in section 4.3. With the large detuning the spontaneous emission is so minimal that switching to this method works well, however this does require the use of another laser tuned to this further detuning. The measured fidelities using this single site gate scheme are equal to $F^2 = 0.9923(7)$ with an average cross-talk error on all other sites equal to 0.002(9). This error is 4.5 times larger than the global gates which is attributed to fluctuations in intensity and pointing of the tightly focused beam. Because of the finite size of the Stark beam

---

[4] $\Omega_{\mu\mathrm{W}} = 4.74$ kHz in these experiments.

there is some intensity overlap to nearest neighbor sites that is as high as 5%, resulting in increased cross-talk errors when compared to further away sites. The average cross-talk error amongst the nearest neighbor sites is 0.014 ± 0.02. A smaller beam will minimize cross-talk but will increase sensitivity to alignment drifts and the atom temperature. Use of some composite pulse sequences, described in the following section, or use of a beam with a top-hat profile could alleviate these issues. This trade-off must be considered moving forward.

4.6 Improving Single Qubit Rotations with Composite Pulse Techniques

Errors in the lab that can affect the performance of our quantum gates can be both random and systematic in nature. The error threshold theorem tells us that if our error per gate is less than a certain threshold, we can in principal use quantum error correction to execute arbitrarily long and arbitrarily accurate quantum computations[65]. However these threshold values are predicted to be about $\mathrm{O}(-4)$ to $\mathrm{O}(-6)$. Composite pulse techniques can be used to alleviate certain systematic errors. Systematic errors can arise from miscalibrated apparatus, inhomogeneities in the driving field across the spatial extent of the qubit system, or qubit frequency offsets due to varying Stark shifts across the qubit system. Composite pulse methods take advantage of the fact that concatenation of several pulses can produce more accurate rotations than a single pulse. It has been shown that systematic errors can be compensated for without specific knowledge of the magnitude of the error and these methods have been used by the NMR community for many years [67]. For quantum computation purposes we are interested in "fully compensating" sequences that work without specific knowledge of the initial state[68].

Systematic errors in the context of single qubit rotations are usually categorized as one of the following: pulse length errors (PLE) and off resonant errors (ORE). Pulse length errors can be thought of as over/under rotations or amplitude errors. When some pulse length error has occurred the rotation angle is modified by $\theta' = \epsilon\theta$ for some small error, ϵ. For a large system of qubits, these errors can occur if there are inhomogeneities in the driving field across the system. For example, if one had a laser beam set up to hit multiple qubits at the same time, the intensity closer to the edges of the beam would be less than at the center resulting in position dependent Rabi frequencies.

Off-resonance errors are due to the driving field being detuned from the qubit frequency. The rotation angle is modified by $\theta' = \theta\sqrt{1 + \delta^2/\Omega^2}$. On the Bloch sphere the axis of rotation is tilted out of the x-y plane. Using the same example as above of a large beam addressing multiple qubits, the qubits in the center of the beam will experience a different differential Stark shift than the qubits on the edge of the beam resulting in different qubit frequencies. In our system, slight alignment errors of our trapping array cause some sites to have more trapping light at the center of the trap than other sites. This will cause different differential shifts and therefore different qubit frequencies across the array as demonstrated in section 4.2.

There exists a large number of composite pulse sequences. Here I will present a few examples and discuss how they may be useful to us.

4.6.1 Pulse Length Errors

The first type of pulse length compensating sequence is called broadband number 1(BB1)[68]. An imperfect pulse which has some rotation error, ϵ, is written as

$$V_\phi(\theta) = U_\phi(\theta[1 + \epsilon]), \tag{4.52}$$

where $U_\phi(\theta) = e^{-i\theta(\sigma_x \cos\phi + \sigma_y \sin\phi)/2}$ is a rotation about some axis in the x-y plane of the Bloch sphere.

BB1 is executed by implementing the following sequence

$$R_{\mathrm{BB1}}(\theta) = V_\phi(\pi)V_{3\phi}(2\pi)V_\phi(\pi)V_0(\theta) \tag{4.53}$$

for $\phi = \cos^{-1}(-\theta/4\pi)$. It is instructive to visualize this sequence on the Bloch sphere. Say, for example, we wish to execute a $\pi/2$-pulse so $V_0(\theta) = V_0(\pi/2)$. Doing $V_0(\pi/2)$ alone should brings the Bloch vector to the equator of the Bloch sphere, but due to imperfections in the system the target position is missed by some small amount, ϵ. We compensate for this by implementing the rest of the BB1 sequence. Fig. 4.13 traces out how each rotation acts on the vector on the Bloch sphere, for a given value of ϵ. Fig. 4.14 shows the full BB1 sequence for different values of ϵ.

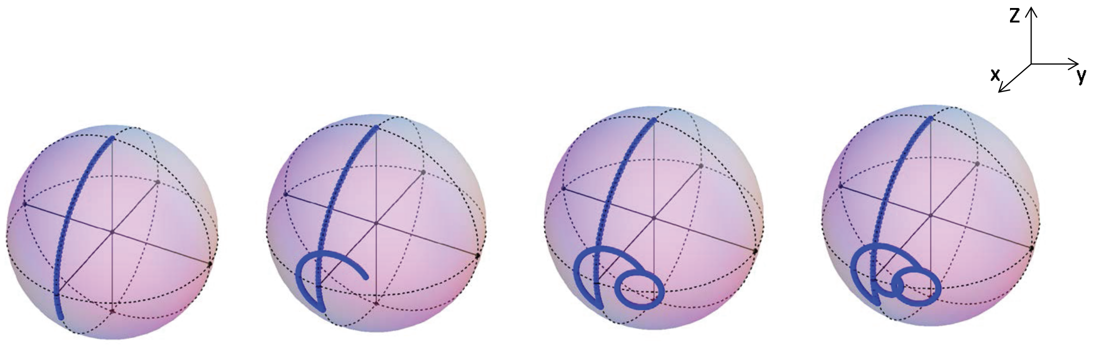

$V_0(\theta)$ $V_\phi(\pi)V_0(\theta)$ $V_{3\phi}(2\pi)V_\phi(\pi)V_0(\theta)$ $V_\phi(\pi)V_{3\phi}(2\pi)V_\phi(\pi)V_0(\theta)$

Figure 4.13: For an error, $\epsilon = 0.2$, each pulse of BB1 is traced on the Bloch sphere.

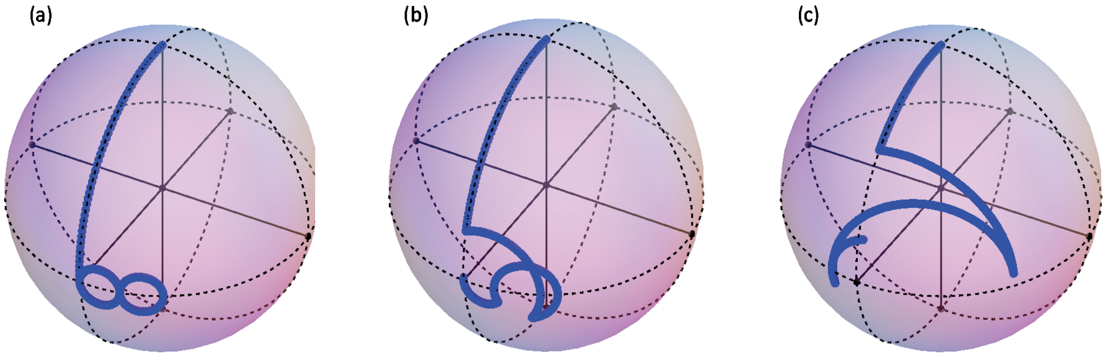

Figure 4.14: Full BB1 sequence traced on the Bloch sphere for different values of ϵ: (a) ϵ=-0.01, (b) ϵ=-0.2, (c) ϵ=0.5. Note for ϵ=0.5, the procedure fails.

Another useful pulse sequence for correcting pulse length errors is called SK1 [69] which is implemented by the following pulse sequence:

$$R_{\mathrm{SK1}}(\theta) = V_\phi(2\pi)V_{-\phi}(2\pi)V_0(\theta), \tag{4.54}$$

for $\phi = \cos^{-1}(-\theta/4\pi)$. Fig. 4.15 shows the fidelity, or overlap with the target state, of a few different sequences including a single pulse, SK1 sequence and BB1 sequence as a function of the rotation error. This plot shows the broadband nature of the BB1 and how insensitive it is to rotation errors. Clearly this is the favorable sequence for executing global rotations. The narrower,

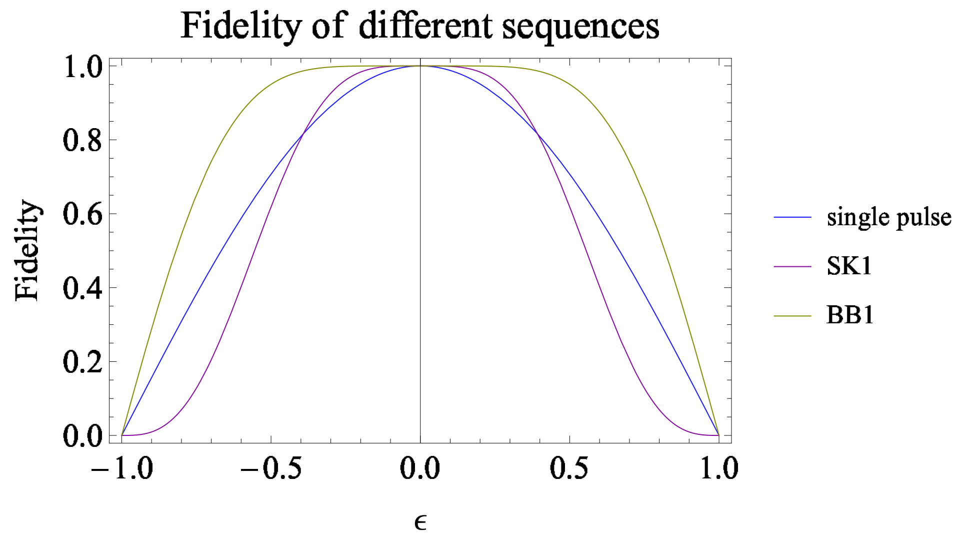

Figure 4.15: Fidelity of different sequences as a function of rotation error

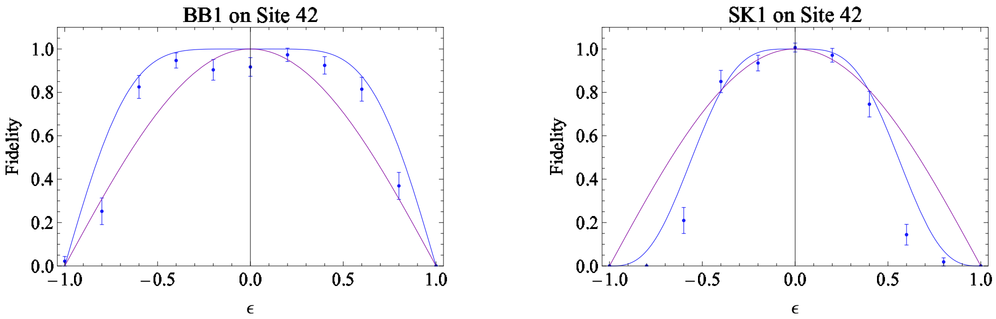

Figure 4.16: Experimental demonstration of BB1 and SK1, plotted with theoretical curves for comparison. BB1 data from 2014_02_17_08_14_53. SK1 data from 2014_02_17_08_53_57.

flat-top nature of SK1 should be favorable for single site rotations when we care about addressing and cross-talk error.

We have demonstrated both SK1 and BB1 using global microwave pulses on the atoms. Fig. 4.16 shows an example performed on a specific site. The data is plotted with the theoretical fidelity curve for the respective composite pulse sequence along with a single pulse for comparison.

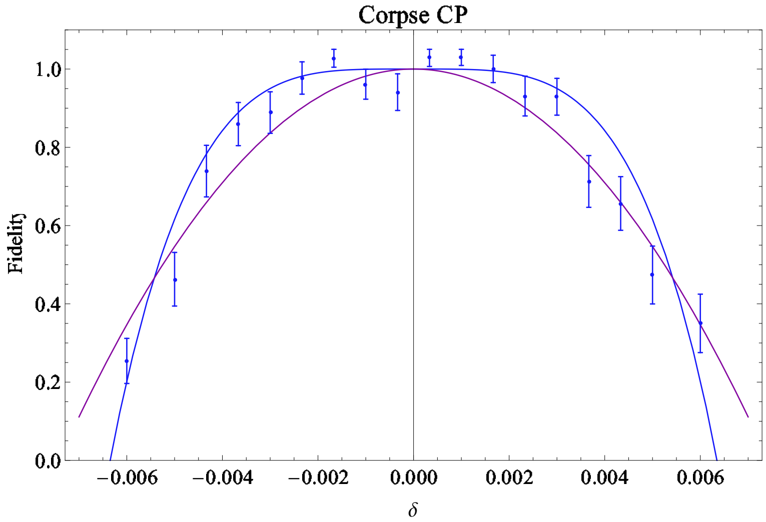

Figure 4.17: Experimental demonstration of CORPSE, plotted with theoretical curves for comparison. Data from 2014_02_17_10_31_29.

4.6.2 Off-Resonance Errors

A driving field that is slightly off-resonance will cause a tilt in the rotation axis and a modification to the rotation angle from θ to $\theta' = \theta\sqrt{1+\delta^2/\Omega^2}$ where δ is the error. One fully compensating composite pulse sequence for correcting these errors is called CORPSE [70]:

$$R_{\text{CORPSE}}(\theta) = V_0(\frac{\theta}{2} - k)V_\pi(2\pi - 2k)V_0(2\pi + \frac{\theta}{2} - k), \tag{4.55}$$

where

$$k = \arcsin(\sin(\theta/2)/2). \tag{4.56}$$

Fig. 4.17 shows a experimental demonstration of the CORPSE sequence. One thing to keep in mind when implementing these sequences is the added length of the pulse. For BB1 and SK1, in order to compensate for a π-pulse a total of 5π rotation is needed. For a CORPSE π-pulse a total of $13\pi/3$ rotation is needed. Given our 10 KHz microwave Rabi frequency, a 5π rotation takes 250 μs which is $\sim$ 5% of the T_2^* time. To correct for both pulses simultaneously, one can think about concatenation sequences. For example, one could concatenate BB1 with CORPSE. Then each of the pulses that make up BB1 would be executed with a CORPSE sequence giving a total of 12 rotations. To compensate for a π-pulse a total of 19π rotation is needed which is impractical given our microwave Rabi frequency and T_2^* time. Increasing the microwave power and increasing the T_2^* will allow us to take advantage of these techniques.

Chapter 5

Coherent Rydberg Excitations

As outlined in Chapter 1, the primary advantage of Rydberg mediated quantum information processing comes from the ability to turn on and off the long-range interaction between qubits. In order to take advantage of this we need the ability to coherently transfer population between the ground and Rydberg states.

The wavelength needed for a single photon excitation to the Rydberg levels is 319 nm in cesium. Building a high-power, narrow linewidth laser at such a short wavelength is technically challenging though some groups take this approach [71, 72]. We use a two-photon excitation to ns or nd levels. Here we excite to the Rydberg level by way of the intermediate excited state, $7p_{1/2}$. We chose the second resonance lines because the photons required here are at 459 nm and 1038 nm. It is relatively easy to get a lot of power at 1038 nm as commercial fiber amplifiers are built for this wavelength. As will be discussed later in this chapter, the matrix element connecting the intermediate level to the Rydberg state is much smaller than that connecting ground to the intermediate, so we prefer our second photon to have higher power in order to do fast Rydberg Rabi oscillations. Using the first resonance $6p_{1/2}$ or $6p_{3/2}$ would require the second photon to have a wavelength of 494 nm or 510 nm and it is much harder to get high power lasers at these wavelengths.

5.1 Semi-Classical Derivation

The coupling between the states is shown schematically in Fig. 5.1. E_1 connects $|g\rangle$ and $|p\rangle$ and E_2 connects $|p\rangle$ and $|r\rangle$. The Hamiltonian is $H = H_0 + V_d$ where the unperturbed Hamiltonian is $H_0 = \hbar\omega_g|g\rangle\langle g| + \hbar\omega_p|p\rangle\langle p| + \hbar\omega_r|r\rangle\langle r|$. The interaction is $V_d = -E_1 d_{pg} - E_2 d_{rp} + h.c.$, where

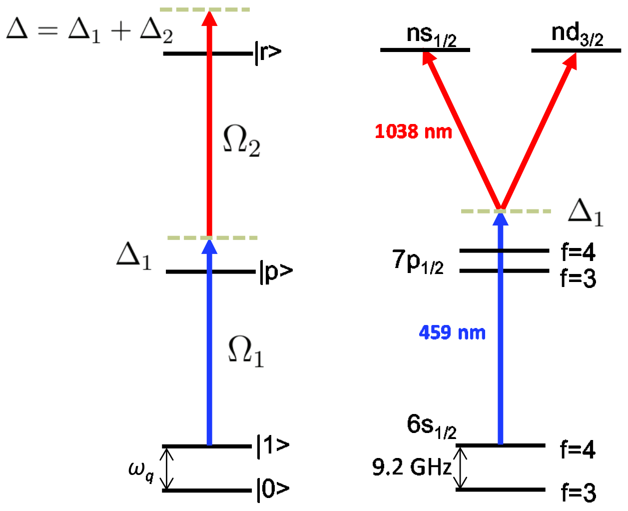

Figure 5.1: (left) A general level diagram from the excitation to a chosen Rydberg level. (right) A more specific diagram relevant to the work in this thesis.

d_{ij} is the same dipole operator introduced in Chapter 4, $\mathbf{d} = -e\mathbf{r}$. The wavefunction describing this three level system is written as

$$|\psi\rangle = c_g(t)e^{-i\omega_g t}|g\rangle + c_p(t)e^{-i\omega_p t}|p\rangle + c_r(t)e^{-i\omega_r t}|r\rangle. \tag{5.1}$$

Plugging this into the Schroedinger equation, applying the RWA and transforming into an appropriate rotating frame will result in three coupled differential equations for the probability amplitudes [73]:

$$\begin{aligned}\dot{c}_g &= -i\frac{\Delta}{2}c_g + i\frac{\Omega_1^*}{2}c_p,\\ \dot{c}_p &= i\frac{\delta}{2}c_p + i\frac{\Omega_1}{2}c_g + i\frac{\Omega_2^*}{2}c_r,\\ \dot{c}_r &= i\frac{\Delta}{2}c_r + i\frac{\Omega_2}{2}c_p.\end{aligned} \tag{5.2}$$

Here $\Delta = \Delta_1 + \Delta_2$ and $\delta = \Delta_1 - \Delta_2$. When $\delta >> \Omega_1, \Omega_2$ we can adiabatically eliminate [74] the intermediate state by setting $\dot{c}_p = 0$, and thus $c_p = -\frac{\Omega_1}{\delta}c_g - \frac{\Omega_2^*}{\delta}c_r$, resulting in an effective two level system

$$\begin{aligned}\dot{c}_g &= -\frac{i}{2}\Delta_1^{'}c_g - \frac{i}{2}\Omega_R^* c_r,\\ \dot{c}_r &= \frac{i}{2}\Delta_2^{'}c_r - \frac{i}{2}\Omega_R c_g.\end{aligned} \tag{5.3}$$

Here $\Delta'_{1(2)} = \Delta \pm \frac{|\Omega_{1(2)}|^2}{\delta}$ is the effective detuning which includes the a.c. Stark shifts and $\Omega_R = \frac{\Omega_1\Omega_2}{\delta} = \frac{\Omega_1\Omega_2}{2\Delta_1-\Delta}$ is the two-photon Rabi frequency. In the relevant situation when $|\Delta_1| \gg |\Delta|$, we take the approximation $\delta \simeq 2\Delta_1$ and therefore $\Omega_R = \frac{\Omega_1\Omega_2}{2\Delta_1}$. The single photon Rabi frequencies depend on the field amplitude and polarizations along with the transition matrix elements to the relevant states.

Solving the coupled differential equations assuming that at time $t = 0$ all population is in the ground state, $c_g(0) = 1$ and $c_r(0) = 0$, the probability of being the in Rydberg state as a function of time is

$$P_r(t) = \frac{\Omega_R^2}{\Omega'^2}\sin^2(\frac{\Omega' t}{2}), \tag{5.4}$$

where $\Omega' = \sqrt{|\Omega_R|^2 + \Delta_+^2}$ is the effective off-resonance Rabi frequency and $\Delta_\pm = (\Delta'_1 \pm \Delta'_2)/2$. Note that the resonance condition, when full population transfer to the Rydberg state occurs, happens when $\Delta_+ = 0$. This resonance condition includes the ac Stark shifts from each of the excitation beams.

The single photon Rabi frequencies are $\Omega_1 = -eE_1\langle p|\mathbf{r}\cdot\epsilon_1|g\rangle/\hbar$, $\Omega_2 = -eE_2\langle r|\mathbf{r}\cdot\epsilon_2|p\rangle/\hbar$ with E_i, ϵ_i the field amplitudes and polarizations. To compute these, the matrix element is reduced via the Wigner-Eckart theorem to an angular factor times a radial matrix element $\langle n'l'_{j'}||r||nl_j\rangle$. For a two photon Rydberg excitation to Rydberg level, n, via the $7p_{1/2}$ level in Cesium the reduced matrix elements we are concerned with are [63]

$$\begin{aligned} \langle 7p_{1/2}||r||6s_{1/2}\rangle &= 0.276a_0, \\ \langle ns_{1/2}||r||7p_{1/2}\rangle &= \frac{-8.08}{n^{3/2}}a_0, \\ \langle nd_{3/2}||r||7p_{1/2}\rangle &= \frac{-22.2}{n^{3/2}}a_0, \end{aligned} \tag{5.5}$$

where the Rydberg wavefunctions are calculated using measured quantum defects [75].

5.1.1 Including the intermediate state hyperfine structure

As discussed in section 4.3, the $7p_{1/2}$ level has a hyperfine structure that needs to be considered when the detuning, Δ_1, is comparable to this splitting. The two-photon Rabi frequency derived above, $\Omega_R = \frac{\Omega_1\Omega_2}{2\Delta_1}$, is only accurate when $|\Delta_1| >> \Delta_{hf}$ where Δ_{hf} is the width of the hyperfine structure which is equal to 377.4 MHz for the $7p_{1/2}$ level in cesium. Within the hyperfine manifold the relative detuning from the center of mass is

$$\Delta_{f_p} = \frac{A}{2}[f_p(f_p+1) - I(I+1) - j_p(j_p+1)], \tag{5.6}$$

where A is the magnetic dipole hyperfine constant equal to 94.35 MHz. For the relevant quantum numbers $f_p = 3, 4$, $I = 7/2$ and $j_p = 1/2$, $\Delta_{f_3} = -2\pi \times$ 212.3 MHz and $\Delta_{f_4} = 2\pi \times$ 165.1 MHz. The two-photon Rabi frequency between hyperfine states becomes

$$\Omega^{f_r,m_{f_g}+q_1+q_2}_{f_g,m_{f_g}} = \Omega\tilde{\Omega}^{f_r,m_{f_g}+q_1+q_2}_{f_g,m_{f_g}}, \tag{5.7}$$

where Ω is the "reduced" Rabi frequency,

$$\Omega = \frac{E_1E_2\langle n_rL_rSJ_r||r||n_pL_pSJ_p\rangle\langle n_pL_pSJ_p||r||n_gL_gSJ_g\rangle}{2\hbar^2\Delta_1}, \tag{5.8}$$

and the relevant $\langle nLSJ||r||n'L'S'J'\rangle$'s are computed using eq.(5.5). The angular factor is computed by summing over the intermediate hyperfine states

$$\tilde{\Omega}^{f_r,m_{f_g}+q_1+q_2}_{f_g,m_{f_g}} = \sum_{f_p} c^{j_pf_p}_{Ij_gf_g} c^{j_rf_r}_{Ij_pf_p} C^{f_r,m_{f_g}+q_1+q_2}_{f_p,m_{f_g}+q_1,1,q_2} C^{f_p,m_{f_g}+q_1}_{f_g,m_{f_g},1,q_1} \frac{\Delta_1}{\Delta_1 - \Delta_{f_p}}. \tag{5.9}$$

Recalling from chapter 4, $C^{\cdot\cdot}_{\cdot\cdot\cdot\cdot}$ is a Clebsch-Gordon coefficient and

$$c^{j_1,I,f_1}_{j_2,I,f_2} = (-1)^{1+I+f_1+j_2}\sqrt{2f_1+1}S^{j_1,I,f_1}_{f_2,1,j_2}, \tag{5.10}$$

where $S^{\cdot\cdot\cdot}_{\cdot\cdot\cdot}$ is the 6j symbol.

We are coupling hyperfine ground states characterized by hyperfine quantum numbers $(n, I, j, l, s, f, m_I, m_f)$ to highly excited Rydberg fine-structure states that are characterized by the fine structure quantum numbers $(n, I, j, l, s, m_I, m_j)$. The Rydberg hyperfine states can be expanded as

$$|j_rI; m_{j_r}, m_I\rangle = \sum_{f_r,m_{f_r}} C^{f_r,m_{f_r}}_{j_r,m_{j_r},I,m_I}|j_rI; f_rm_{f_r}\rangle. \tag{5.11}$$

In our situation, we are always starting in a single ground hyperfine level, $m_{f_g} = 0$, so m_{f_r} is fixed by the angular momenta of the photons: $m_{f_r} = m_{f_g} + q_1 + q_2$. Then the effective angular factor coupling ground hyperfine to Rydberg fine structure states can be written as

$$\bar{\Omega}^{j_r,m_{j_r}}_{f_g,m_{f_g}} = \sum_{f_r} C^{f_r,m_{f_r}}_{j_r,m_{j_r},I,m_I}\tilde{\Omega}^{f_r,m_{f_r}}_{f_g,m_{f_g}}. \tag{5.12}$$

Note that $m_I = m_{f_r} - m_{j_r}$ and therefore $m_I = m_{f_g} + q_1 + q_2 - m_{j_r}$. In many cases there are two Rydberg Zeeman states with different values of m_{j_r} that can couple to the ground state. A bias field is applied to separate these m_{j_r} states by some amount that is large compared to the Rabi frequency. Then the laser can be tuned to be resonant with just one state. The Zeeman states are shifted by the bias field by an amount $\Delta E = g_j \mu_B m_{j_r} B$ where μ_B is the Bohr Magneton equal to 1.4 MHz/G, B is the applied magnetic field, and g_j is the Landé g-factor which is equal to 2 for the Rydberg $ns_{1/2}$ states and $\frac{4}{5}$ for the $nd_{3/2}$ states. Typically, we use the same bias field strength as that which is used for optical pumping, $B = 1.5$ G. For example, applying this field to an $ns_{1/2}$ state will shift the levels an amount equal to $\Delta E = 1.5\mathrm{G} \times 1.4\mathrm{MHz/G} \times \pm\frac{1}{2} \times 2 = \pm 2.1$ MHz.

The single photon Rabi frequencies are needed to calculate the Stark shifts and spontaneous emission rates. These should also include this intermediate hyperfine splitting. The one photon Rabi frequencies are also split into their angular and radial parts:

$$\begin{aligned}
\Xi^{f_p}_{f_g,m_{f_g},q_1} &= \Xi_{gp}\tilde{\Xi}^{f_p}_{f_g,m_{f_g},q_1} = \Xi_{gp} c^{j_p,f_p}_{I,j_g,f_g} C^{f_p,m_{f_g}+q_1}_{f_g,m_{f_g},1,q_1}, \\
\Xi^{f_p}_{j_r,m_{j_r},q_2} &= \Xi_{rp}\bar{\Xi}^{f_p}_{j_r,m_{j_r},q_2} = \Xi_{rp} \sum_{f_r} c^{j_p,f_p}_{I,j_r,f_r} C^{f_p,m_{f_g}+q_1}_{f_r,m_{f_r},1,-q_2} C^{f_r,m_{f_r}}_{j_r,m_{j_r},I,m_I}.
\end{aligned} \tag{5.13}$$

Here the radial parts of the single photon Rabi frequencies are

$$\begin{aligned}
\Xi_{gp} &= \frac{eE_1 \langle n_p L_p S J_p || r || n_g L_g S J_g \rangle}{\hbar}, \\
\Xi_{rp} &= \frac{eE_2 \langle n_r L_r S J_r || r || n_p L_p S J_p \rangle}{\hbar}.
\end{aligned} \tag{5.14}$$

In Chapter 6 we will become concerned with the various Stark shifts induced by the excitation beams on both the ground and the Rydberg states. These can be calculated with the modified single photon Rabi frequencies by summing over the intermediate hyperfine states. The shift on the ground state is then

$$\Delta_{\mathrm{ac},g} = \frac{\Xi_{gp}}{4} \sum_{f_p} \frac{(\tilde{\Xi}^{f_p}_{f_g,m_{f_g},q_1})^2}{\Delta_1 - \Delta_{f_p}}. \tag{5.15}$$

The shift on the Rydberg state is similarly calculated

$$\Delta_{\mathrm{ac},r} = \frac{\Xi_{rp}}{4} \sum_{f_p} \frac{(\bar{\Xi}^{f_p}_{j_r,m_{j_r},q_2})^2}{\Delta_1 - \Delta_{f_p}}. \tag{5.16}$$

The final quantity we care about is the number of photons scattered from the intermediate level during a Rydberg π-pulse, t_π:

$$N = \frac{\gamma_p t_\pi}{2}\left[\Xi_{gp}^2 \sum_{f_p} \frac{(\tilde{\Xi}^{f_p}_{f_g,m_{f_g},q_1})^2}{2(\Delta_1-\Delta_{f_p})^2} + \Xi_{rp}^2 \sum_{f_p} \frac{(\tilde{\Xi}^{f_p}_{j_r,m_{j_r},q_2})^2}{2(\Delta_1-\Delta_{f_p})^2}\right], \tag{5.17}$$

where $\gamma_p = 1/\tau_p$ is the radiative decay from the p level. Generally we want $N << 1$.

5.1.2 Fine structure Rabi frequencies

As mentioned before, when Δ_1 is large compared to the hyperfine splitting of the intermediate level the coupling through the intermediate level can be approximated in terms of the fine structure states. In this limit $\Omega_R = \Omega_1\Omega_2/2\Delta_1$ and the one photon Rabi frequencies are

$$\begin{aligned} \Omega_1 \equiv& \Omega^{j_p,m_{j_g}+q_1}_{j_g,m_{j_g}} = \Omega_1'\bar{\Omega}^{j_p,m_{j_g}+q_1}_{j_g,m_{j_g}}, \\ \Omega_2 \equiv& \Omega^{j_r,m_{j_g}+q_1+q_2}_{j_p,m_{j_g}+q_1} = \Omega_2'\bar{\Omega}^{j_r,m_{j_g}+q_1+q_2}_{j_p,m_{j_g}+q_1}. \end{aligned} \tag{5.18}$$

These are composed of the radial parts,

$$\begin{aligned} \Omega_1' =& \frac{E_1\langle n_pL_pSJ_p||r||n_gL_gSJ_g\rangle}{\hbar}, \\ \Omega_2' =& \frac{E_2\langle n_rL_rSJ_r||r||n_pL_pSJ_p\rangle}{\hbar}, \end{aligned} \tag{5.19}$$

and the angular parts,

$$\begin{aligned} \bar{\Omega}^{j_p,m_{j_g}+q_1}_{j_g,m_{j_g}} =& \frac{C^{j_p,m_{j_g}+q_1}_{j_g,m_{j_g},1,q_1}}{\sqrt{2j_p+1}}, \\ \bar{\Omega}^{j_r,m_{j_g}+q_1+q_2}_{j_p,m_{j_g}+q_1} =& \frac{C^{j_r,m_{j_g}+q_1+q_2}_{j_p,m_{j_g}+q_1,1,q_2}}{\sqrt{2j_r+1}}. \end{aligned} \tag{5.20}$$

The ground state hyperfine states are expanded as

$$|j_gI;m_{j_g},m_I\rangle = \sum_{f_g,m_{f_g}} C^{f_g,m_{f_g}}_{j_g,m_{j_g},I,m_I}|jI;f_g,m_{f_g}\rangle. \tag{5.21}$$

For experiments discussed in this thesis the relevant hyperfine ground state is the $|f_g=4,m_g=0\rangle$ state. For the $m_{f_g}=0$ states, $m_I=-m_{j_g}$ and for $f_g=4$, this coupling factor is equal to $1/\sqrt{2}$. The total expression for the two photon Rabi frequency is

$$\Omega = \frac{1}{\sqrt{2}}\frac{\Omega_1'\Omega_2'}{2\Delta_1}\bar{\Omega}^{j_p,m_{j_g}+q_1}_{j_g,m_{j_g}}\bar{\Omega}^{j_r,m_{j_g}+q_1+q_2}_{j_p,m_{j_g}+q_1}. \tag{5.22}$$

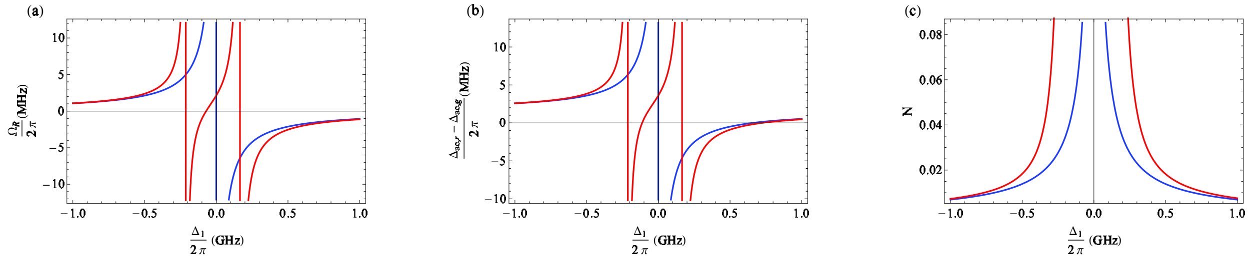

Figure 5.2: Calculations of the (a) Rydberg Rabi frequency the (b) Ground-Rydberg differential Stark shift and (c) the number of photons scattered from $7p_{1/2}$ during a Rydberg π-pulse using the full hyperfine structure (red) and the fine structure approximation (blue). Parameters chosen are approximately what is used in the following experiments. Rydberg level $82s_{1/2}$, $q_1 = 1$, $q_2 = -1$, $P_{459} = 45\mu$W, $P_{1038} = 4$ mW, $w_{459} = 3\mu$m, $w_{1038} = 3.7\mu$m.

The ac Stark shifts and spontaneous emission rates are computed in a similar fashion as in section 5.1.1 but using the single photon angular factors computed in equation (5.20). In the limit that $\Delta_{f_p} \to 0$ the quantities computed in this section will converge with those computed in section 5.1.1. A comparison of these two calculations as Δ_1 is varied can be seen in Fig. 5.2. For each calculation the red curve represents the results including the full hyperfine structure and the blue curve represents the results in the fine structure limit.

5.1.3 $6s_{1/2} - 7p_{1/2} - ns_{1/2}$

As an example, consider an excitation to an $ns_{1/2}$ Rydberg state from the $|f = 4, m_f = 0\rangle$ ground state via the $7p_{1/2}$ state using photons with $q_1 = +1$ and $q_2 = -1$. With this photon polarization choice we couple through the $m_{j_p} = +1/2$ state in the p level and thus only couple to the $m_{j_r} = -1/2$ in the Rydberg level. The relevant quantum numbers are $j_g = 1/2$, $j_p = 1/2$, $j_r = 1/2$, $m_{j_r} = -1/2$, $f_g = 4$, $m_g = 0$, $f_p = 3(4)$, $f_r = 3(4)$, $m_{f_r} = 0$, $I = 7/2$ and $m_I = +1/2$. The two-photon angular factor coupling the ground $|4, 0\rangle$ hyperfine state to the Rydberg fine state $|1/2, -1/2\rangle$ is computed using equations (5.9) and (5.12):

$$\bar{\Omega}_{4,0}^{1/2,-1/2} = -\frac{1}{3\sqrt{2}} \frac{1 - \frac{5\Delta_{p3}}{8\Delta_p} - \frac{3\Delta_{p4}}{8\Delta_p}}{(1 - \frac{\Delta_{p3}}{\Delta_p})(1 - \frac{\Delta_{p4}}{\Delta_p})}. \tag{5.23}$$

Using the fine structure formula (5.22) the angular factor, using the above quantum numbers, is equal to $-\frac{1}{3\sqrt{2}}$. Setting $\Delta_{p_4} = 0$ and $\Delta_{p_3} = 0$ in equation (5.23), which is equivalent to the limit where $\Delta_1 >> \Delta_{hf}$, results in an angular factor equal to $-\frac{1}{3\sqrt{2}}$. As expected the fine structure Rabi frequency and the hyperfine structure Rabi frequency converge.

Table 5.1 shows the two photon Rabi frequency calculated using the full hyperfine equations (HF) and using the fine structure approximation (FS). Also calculated is the differential Stark shift of the ground and Rydberg state and the photon scattering rate from the intermediate level. The parameters are chosen to be close to the experimental parameters used in the following sections of this thesis. Calculations are done using two different detunings. At a detuning of -2.2 GHz the difference between the hyperfine calculation and the fine structure calculation is less than a percent. The fine structure approximation is valid here. Moving to a detuning of +0.82 GHz results in a $\sim 7\%$ difference so clearly the hyperfine equations are needed at this point.

5.1.4 $6s_{1/2} - 7p_{1/2} - nd_{3/2}$

Using this two photon excitation scheme via the $7p_{1/2}$ level it is also possible to excite $nd_{3/2}$ Rydberg states. Starting in $m_{f_g} = 0$ will result in $m_{f_r} = 0$ or ± 2 depending on the photon polarization and f_r = 5,4,3, or 2. Equation (5.12) can be used to map onto the Zeeman states whose quantum numbers can be $m_{j_r} = \pm 3/2$ or $\pm 1/2$ depending on the photon polarization. A single Zeeman level is selected by applying a bias field.

5.2 Rydberg Laser

The light used for coherent excitation to the Rydberg level is made up of two separate lasers at 459 nm and 1038 nm. The 459 nm laser denoted as Rydberg A connects $|f_g = 4\rangle$ hyperfine level of the ground state to the intermediate $7p_{1/2}$ level. The 1038 nm laser provides the second photon needed in the excitation and connects the intermediate $7p_{1/2}$ to the desired Rydberg level. Both lasers are shown schematically in Fig. 5.3.

The Rydberg A laser is a 918 nm extended cavity diode laser (ECDL) that is locked to a high finesse cavity using the Pound-Drever-Hall (PDH) technique [76]. The cavity acts both to narrow

Table 5.1: Two-photon Rabi Frequency, differential Stark shift, and photon scattering calculations for $82s_{1/2}$ Rydberg level using the exact hyperfine method (HF) and the fine structure approximation (FS). Calculations are done with two different detunings with parameters approximately equal to what is used in typical experiments.

Rydberg Level	$82s_{1/2}, m = -1/2$	$82s_{1/2}, m = -1/2$
detuning from the center of mass of the 7p level	$-2\pi \times$ 2.2 GHz	$+2\pi \times 0.82$ GHz
Power of 459 beam at atoms	45 μW	30 μW
Power of 1038 beam at atoms	4 mW	2.4 mW
459 beam waist	3 μm	3 μm
1038 beam waist	3.7 μm	3.7 μm
Two photon Rabi Frequency, $\Omega_{\rm HF}$	$2\pi\times$480 kHz	$2\pi\times$879 kHz
Two photon Rabi Frequency, $\Omega_{\rm FS}$	$2\pi\times$481 kHz	$2\pi\times$814 kHz
$(\Delta_{{\rm ac},r} - \Delta_{{\rm ac},g})_{\rm HF}$	$2\pi \times$ 2 MHz	$2\pi \times$ 17 kHz
$(\Delta_{{\rm ac},r} - \Delta_{{\rm ac},g})_{\rm FS}$	$2\pi \times$ 2 MHz	$2\pi \times$ 85 kHz
photon scattering, $N_{\rm HF}$	0.3%	1.0%
photon scattering, $N_{\rm FS}$	0.3%	0.9%

the line-width and serve as a stable frequency reference. A small fraction of the light from the EDCL is picked off for the cavity lock. First a high bandwidth double pass AOM centered at 750 MHz with 500 MHz bandwidth is used to allow for the frequency to scan across the 1.5 GHz free spectral range (FSR) of the cavity. The light then passes through a 79 MHz phase modulating electro-optic modulator (EOM) which adds the frequency sidebands needed for the PDH lock before being sent to the reference cavity. The reference cavity is made up of a 10 cm ultra-low expansion (ULE) glass spacer with two mirrors optically connected to it. One mirror is planar while the other one has a 50 cm radius of curvature. A 1/e lifetime of 17 μs was measured by measuring the ring down time. This gives a reflectivity of 0.99998 and finesse of 160,000. The frequency comb was used to measure the FSR of 1.49685 GHz resulting in a cavity linewidth of 9.4 kHz. The cavity is kept in a temperature controlled vacuum chamber to ensure long term

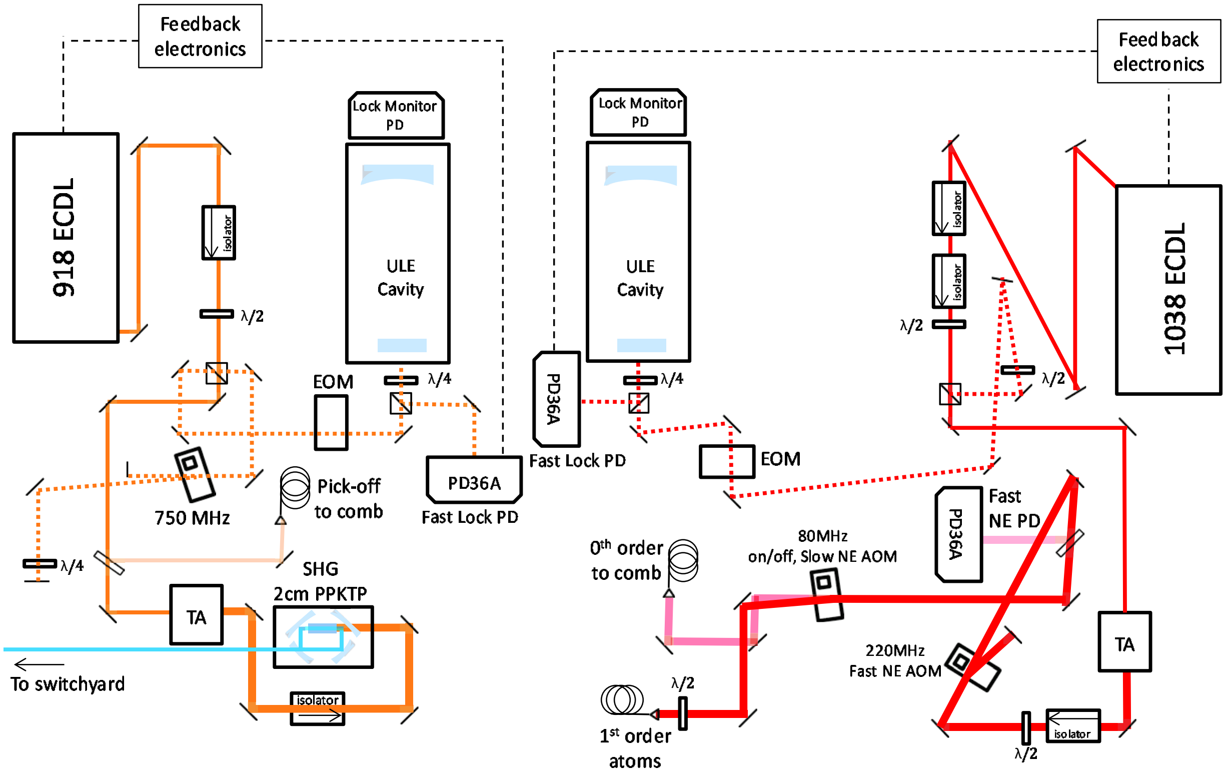

Figure 5.3: Schematic for the Rydberg laser system which includes the 1038 nm laser and the 459 nm laser.

stability. The temperature is set to the zero expansion point using the frequency comb. A plot of this measurement is seen in Fig. 5.4 and the temperature is set to the peak of this curve which corresponds to an actual temperature measured by the hand-held temperature probe of 31.0 C. A fast photodiode looking at the back reflection of the cavity measures the beat frequency created by the carrier and sidebands from the EOM. This signal is then mixed with a local oscillator to generate a DC error signal. This error signal is sent to a circuit for feedback.

The 918 nm light that is not picked off for the lock is now frequency stabilized. A small fraction of this light is picked off and coupled into a fiber and sent to a frequency comb to monitor the laser frequency. The rest of the light is amplified using a tapered amplifier (TA) and then coupled into a second harmonic generation (SAG) cavity. The SAG cavity is a bow tie ring cavity with a 2 cm periodically poled potassium titanyl phosphate (PPKTP) crystal which frequency doubles the light

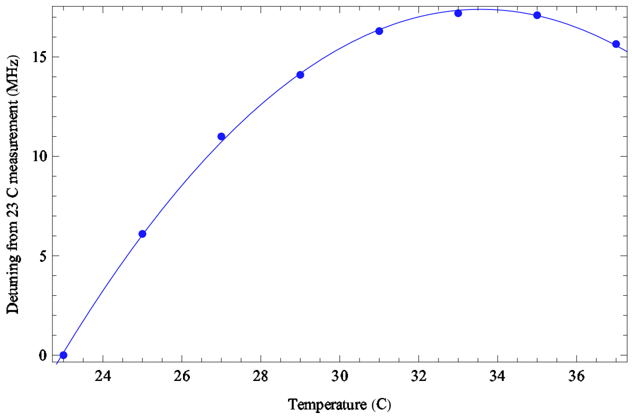

Figure 5.4: Measurement of the zero expansion temperature for the 918 ULE cavity using the frequency comb. The temperatures recorded are the temperature as registered by the TEC driver and have not been well calibrated to actual temperatures. The peak corresponds to an actual temperature measured by the hand-held temperature probe of 31.0 C.

from 918 nm to 459 nm. This light is sent into the "switch-yard", shown in Fig. 5.5, where it is combined with 459 nm Raman light and sent through the same fiber to the experiment table. Before being combined it passes through two AOMs. The first single-pass AOM is used for fast noise eating. A description of this system along with a characterization of the laser noise can be found in Appendix A. Next the beam is sent through another double pass AOM which serves three purposes. As will be seen in section 5.2.1 this AOM will be used to compensate small frequency shifts from the pointing AOMs. It is also used as a on/off switch on the light. Finally this AOM is amplitude modulated for the purpose of slow noise eating, also described in Appendix A. The 1038 nm laser has a similar EDCL to high finesse cavity to TA set up as Rydberg A. This time however there is no SAG cavity. The amplified light is sent through both a fast noise eating AOM and a slow, on/off AOM before being sent to the experiment. The 0^{th} order of the slow noise eating AOM is sent to the frequency comb to monitor the frequency.

5.2.1 Finding the frequency

To hit a specific Rydberg level with the desired detuning from the intermediate state we must tune the laser frequencies taking into account all of the AOMs in the system, including the AOMs

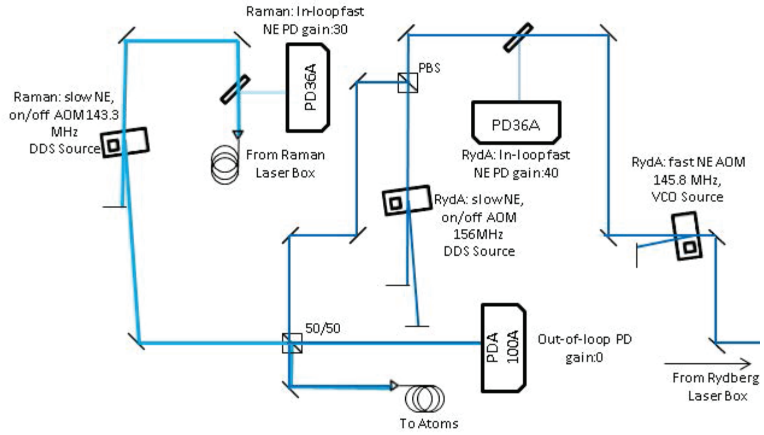

Figure 5.5: Schematic for the 459 nm switch-yard with combines the Rydberg A and the Raman lasers before being sent to the experiment. All AOMs pictured are Brimrose FGM-150-30-459.

in the beam addressing optics. There are 4 AOMs in the Rydberg A system and 3 in the 1038 nm system which impart a frequency shift on the light. The $6s_{1/2}, F = 4 \rightarrow 7p_{1/2}, F' = 4$ resonant frequency is 652504.80 GHz which we have measured with the frequency comb. The laser needs to be tuned a few GHz away from this to minimize spontaneous emission from the intermediate state. Typically our detuning is around -2 GHz. To first order the frequency of the Rydberg A laser, f_{459}, will be this $F = 4 \rightarrow F' = 4$ resonance plus the desired detuning, Δ_1, or $f_{459} = 652504.80\text{GHz} + \Delta_1$. If f_{Ryd} is the total Rydberg frequency, calculated using measured quantum defects [75], then the 1038 nm laser frequency needs to be tuned near to $f_{1038} = f_{\text{Ryd}} - f_{459}$. This is constrained by the discrete modes of the ULE cavity. Small adjustments to Δ_1 must be made to account for this. The higher order mode spacing of the ULE cavity is 220 MHz. Once the desired mode, at f_{1038}, is found the total 1038 laser frequency including all AOM shifts is $f'_{1038} = f_{1038} + f_{\text{on/off}} + f_{\text{scanner,1}} - f_{\text{scanner,2}}$ where $f_{\text{on/off}} = 80$ MHz represents the AOM used for switching and $f_{\text{scanner,1(2)}}$ represents the AOMs used for pointing and can be in between about 140 MHz and 160 MHz. We take the $+1$ order of the first AOM and the -1 order of the second to make the contributions from these AOMs small.

With f'_{1038} fixed, the 918 nm laser frequency is calculated. We measure the frequency using the fiber pick-off which is noted in Fig. 5.3. This pick-off does not see either the switch-yard

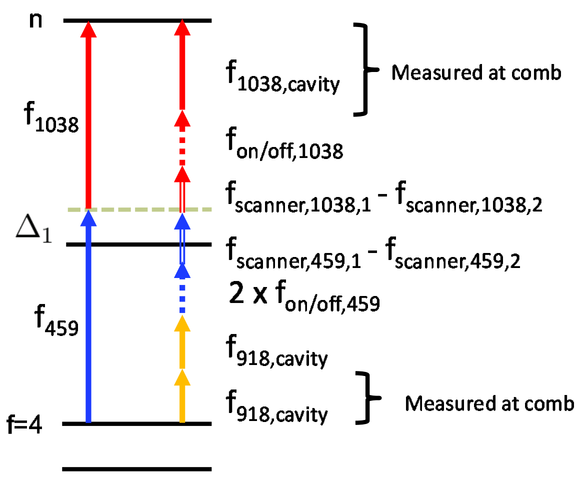

Figure 5.6: Level diagram representing the different frequencies that need to be included in order to find the respective Rydberg level. The 1038 nm laser is locked to a specific cavity mode. The light is additionally shifted by an 80 MHz on/off AOM as well as the two AOMs in the beam scanner. The 918 nm laser is locked to a specific cavity mode before its doubled. Additional shifts are added by way of a double-pass on/off AOM and the two AOMs in the beam scanner. The total of all these frequencies should equal the frequency of the ground to Rydberg transition with the appropriate detuning from the intermediate state.

AOM or the two scanner AOMs. Including everything the laser frequency is $f_{918} = \frac{1}{2}(f_{\text{Ryd}} - f'_{1038} - 2f_{\text{on/off},459} - f_{\text{scanner},1,459} + f_{\text{scanner},2,459})$ recalling that $f_{459} = 2 \times f_{918}$. A combination of changing which cavity mode the 918 nm laser is locked to and changing the frequency of the pre-lock AOM will result in the correct frequency. With any change in any of the scanner AOM frequencies for either 459 or 1038 needed for alignment and site switching, the switch-yard AOM frequency, $f_{\text{on/off},459}$, needs to be adjusted to compensate. This calculation does not include Stark shifts of the excitation beams which are predicted to be a couple MHz.

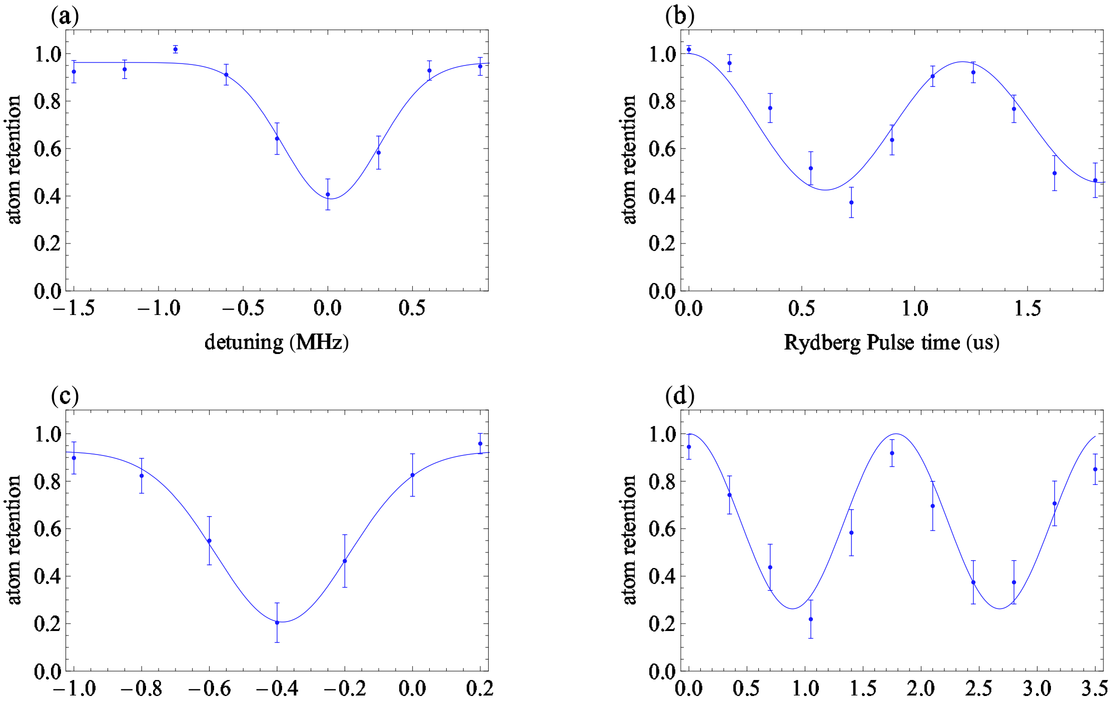

Figure 5.7: Example data for Rydberg two photon spectroscopy experiments and Rabi flopping experiments. (a) A TPS on the $70d_{3/2}$ state. Data from 2014_04_04_07_45_26. (b) An RFE on the $70d_{3/2}$ state. Fit gives a Rabi frequency of 824 ± 21 kHz. Data from 2014_04_04_08_05_03. (c) A TPS on the $82s_{1/2}$ state. Data from 2014_11_03_16_42_53. (d) An RFE on the $82_{1/2}$ state. Fit gives a Rabi frequency of 497 ± 10 kHz. Data from 2014_11_03_17_05_32.

5.3 Rydberg Rabi flopping experiments

Some representative data is shown in Fig. 5.7 for two different Rydberg states $70d_{3/2}$ and $82s_{1/2}$. Table 5.2 lists the parameters used for these experiments along with calculated Rabi frequencies. The Rabi frequencies in this case can be calculated using the fine structure approximation because the detuning in large. First a two photon spectroscopy (TPS) experiment is performed to find the frequency which gives full population transfer from the ground to the Rydberg state. This includes the Stark shift from the excitation beams so slight changes in power or alignment drifts will shift this frequency. The pulse time is fixed to approximately π while the 459 nm frequency,

Table 5.2: Rabi Frequency Calculation for two different angular momentum states using parameters from the experiments shown in 5.7.

Rydberg Level	$70d_{3/2}, m_{j_r} = -3/2$	$82s_{1/2}, m_{j_r} = 1/2$
detuning from the center of mass of the 7p level	$2\pi \times 2.4$ GHz	$2\pi \times 2.2$ GHz
q_1	-1	-1
q_2	-1	+1
Power of 459 beam at atoms	15 μW	45 μW
Power of 1038 beam at atoms	5 mW	4 mW
459 beam waist	3 μm	3 μm
1038 beam waist	3.7 μm	3.7 μm
Two photon Rabi Frequency, Ω	$2\pi\times$860 kHz	$2\pi\times$480 kHz
$\Delta_{\text{ac},r} - \Delta_{\text{ac},g}$	$2\pi \times 1$ MHz	$2\pi \times 2$ MHz
Zeeman shift with 1.5 G	$-2\pi \times 2.5$ MHz	$+2\pi \times 2.1$ MHz

$f_{\text{on/off},459}$, is stepped. The 1038 nm light is always held at a fixed frequency so any change in intensity of either beams is compensated for by changing the 459 nm frequency. Once this frequency is tuned in a Rabi flopping experiment (RFE) is performed by stepping the Rydberg pulse area. For these experiments we turn the trap off during the Rydberg excitation.

We can compare the measured two-photon spectroscopy frequency with the theoretical Rydberg excitation frequencies[77]. As depicted in Fig. 5.6, the experimental two-photon frequency is calculated by summing the frequencies of the lasers plus all the AOM frequencies. The laser frequencies are measured precisely using the frequency comb. Not depicted in the figure is the fact that Stark shifts from the excitation beams and Zeeman shifts from the bias magnetic field must also be included. These values are also calculated in Table 5.2. The difference between the predicted excitation frequency and the measured frequency for the $70d_{3/2}$ state is about 400 kHz. For the $82s_{1/2}$ state the difference between calculated frequency and measured TPS frequency is -7 MHz. This shift is likely due to Stark shifts from dc electric fields.

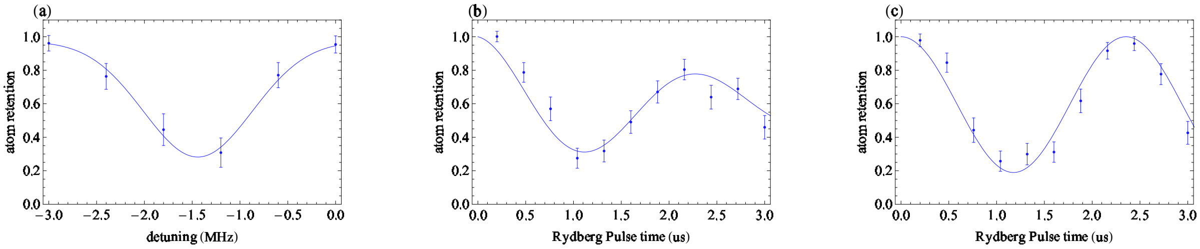

Figure 5.8: (a) The 780 nm trap is left on for this TPS. The detuning is the difference of the frequency with the trap off in the usual scheme. A shift of $\sim$ 1.5 MHz is measured, exactly as expected. Data from 2014_05_28_11_20_41 (b) RFE with the trap on and (c) RFE with the trap off for comparison. The two RFE are taken back to back. More decoherence is seen in the trap on data. (b) Data from 2014_05_28_11_44_43, (c) Data from 2014_05_28_12_25_46.

As mentioned above, for these experiments, the 780 nm trap light is turned off 1 μs before the start of the excitation pulse and turned back on 1 μs after the end of the pulse. The 780 nm light causes large ($\sim$ 1.5 MHz) Stark shifts on the ground-Rydberg transition. Any intensity noise in the 780 nm light will lead to dephasing. The traps can be turned off for $\sim$ 10 μs before the ground state atoms start to experience loss due to their finite temperature so the Rydberg Rabi flopping must be fast compared to $\sim$ 10 μs. One long term goal of this experiment is to be able to perform all excitations with the trap light on. Fig. 5.8 shows an example of a TPS and RFE with the traps turned on next to a regular trap off RFE taken immediately after for direct comparison.

5.4 Rydberg Coherence Time

Just as a ground state coherence time was measured in Chapter 4, and ground-Rydberg coherence time can be measured by measuring the decay of the Ramsey oscillations as the delay time between two $\pi/2$ Rydberg pulses is stepped. In addition, the frequency of these Ramsey oscillations are equal to the total differential Stark shift induced by the excitation beams. This will become an important factor is Chapter 6. Fig. 5.9 shows this measurement performed on the $82s_{1/2}$ state.

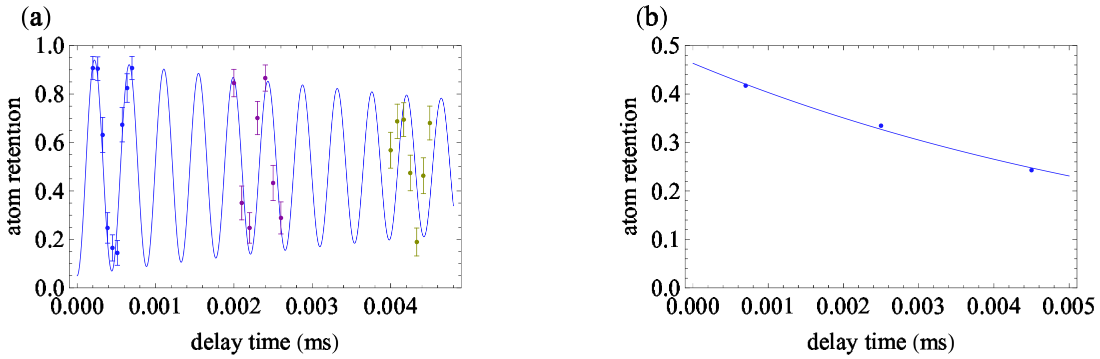

Figure 5.9: Ground-Rydberg T_2 measurement on $82s_{1/2}$ using parameters $\Omega_1 = 2\pi \times 70$ MHz, $\Omega_2 = 2\pi \times 31$ MHz, and $\Delta_1 = -2\pi \times 2.18$ GHz. The decay of the Ramsey signal gives T_2 time of 7 μs. The frequency of the signal gives a ground-Rydberg differential Stark shift of 2.26 MHz. Data from 2014_11_12_16_30_07, 2014_11_12_17_14_11 and 2014_11_12_18_11_49.

5.5 Rydberg Blockade

The mechanism used for creating two atom entanglement is called the Rydberg blockade. Theoretical details of this mechanism are found in Ref. [78]. Excitation of a control atom to a Rydberg level prevents subsequent excitation of a target atom in a neighboring site. We have demonstrated blockade in the array for neighboring sites separated by 3.8 μm, diagonally neighboring sites separated by 5.4 μm and next nearest neighbor sites separated by 7.6 μm. The latter is shown in Fig. 5.10 for the $82s_{1/2}$ Rydberg state. The doubly excited state is shifted off resonance by an amount $B \sim 15$ MHz. The blockade fails when a double-excitation occurs. This happens with probability

$$P_2 \approx \frac{\Omega_{Ryd}^2}{B^2}. \tag{5.24}$$

For $B \sim 15$ MHz and $\Omega_R = 2\pi \times 550$ kHz, $P_2 \approx 0.1\%$.

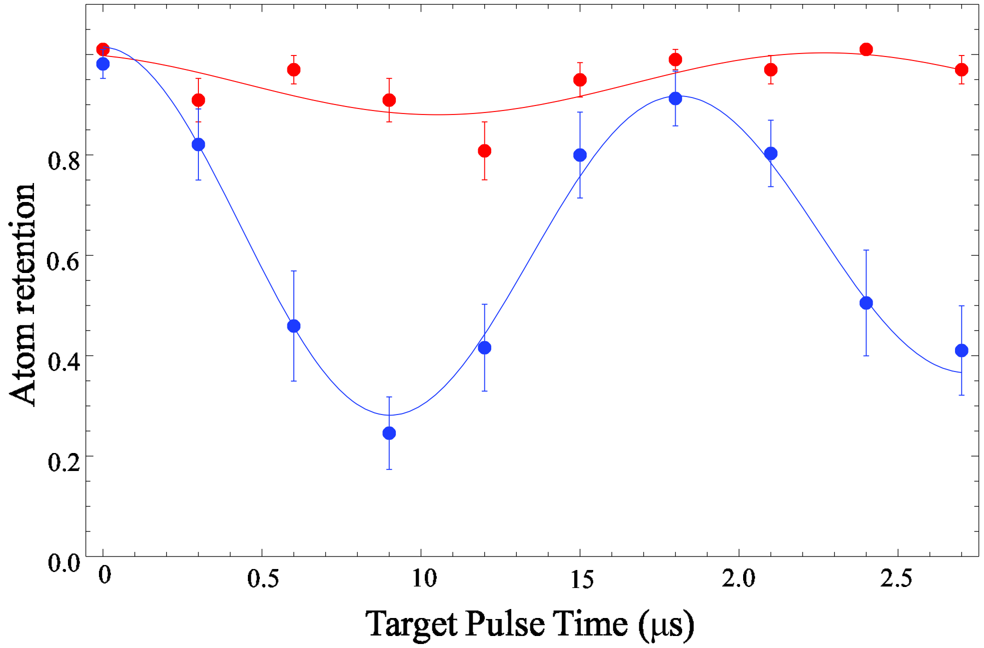

Figure 5.10: Rydberg Rabi flopping experiment on the target site with a Rydberg π pulse on the control site separated by 7.6μm. The target data is cut whether a control atom is present (red curve) or not (blue curve) and therefore represents the blockaded and non-blockaded cases, respectively. Data from 2014_08_18_10_41_40.

Chapter 6

Two Qubit Operations

The fourth DiVincenzo criterion [7] requires our quantum computer to have a universal set of gates. Our universal set of quantum gates is composed of the set of all single qubit gates described in Chapter 4 and the two qubit controlled NOT (CNOT) gate, the subject of this chapter. Two atoms are made to interact via the Rydberg blockade discussed in Chapter 5. Here we use the Rydberg blockade to make controlled phase gates which in turn can be used for CNOT gates and two atom entanglement.

The controlled phase, C_Z, is implemented by a total of three Rydberg pulses: a π pulse on the control, followed by a 2π on the target, followed by another π pulse on the control. When one of the atoms is in the $|1\rangle$ state, the Rydberg pulse is resonant and the atom makes a total 2π rotation picking up a π phase shift. An atom in the $|0\rangle$ state will be 9.2 GHz detuned from the Rydberg level and will therefore remain in $|0\rangle$ picking up zero phase. When the two atom state is $|11\rangle$, the control atom completes a 2π rotation while the target is blockaded and remains in the $|1\rangle$ state picking up zero phase. This constitutes the following two qubit unitary operation in the computational basis

$$C_Z = \begin{pmatrix} 1 & 0 & 0 & 0 \\ 0 & -1 & 0 & 0 \\ 0 & 0 & -1 & 0 \\ 0 & 0 & 0 & -1 \end{pmatrix}. \tag{6.1}$$

To implement the CNOT gate $\pi/2$ ground state pulses are added to the target before and after the C_Z operation. Here the target is flipped when the control is in $|1\rangle$

$$CNOT_1 = \begin{pmatrix} 1 & 0 & 0 & 0 \\ 0 & 1 & 0 & 0 \\ 0 & 0 & 0 & 1 \\ 0 & 0 & 1 & 0 \end{pmatrix}. \tag{6.2}$$

Changing the phase of the second $\pi/2$ by π results in a CNOT gate where the target bit is flipped when the control is $|0\rangle$

$$CNOT_2 = \begin{pmatrix} 0 & 1 & 0 & 0 \\ 1 & 0 & 0 & 0 \\ 0 & 0 & 1 & 0 \\ 0 & 0 & 0 & 1 \end{pmatrix}. \tag{6.3}$$

The example above assumes a simple two level system driven by a single field. In reality, we have a three level system driven by two fields. AC Stark shifts from the driving fields will cause additional phase accumulation on the ground states. The controlled phase operation is actually

$$C_\phi = \begin{pmatrix} e^{i\phi_{00}} & 0 & 0 & 0 \\ 0 & e^{i\phi_{01}} & 0 & 0 \\ 0 & 0 & e^{i\phi_{10}} & 0 \\ 0 & 0 & 0 & e^{i\phi_{11}} \end{pmatrix}. \tag{6.4}$$

6.1 Constructing the controlled phase gate

To calculate the elements of equation (6.4) we need to understand all of the different phase shifts that can occur. Along with the π phase shift expected from a 2π rotation there are additional phase shifts induced by the 459 nm light and the 1038 nm light, both resonant and non-resonant ac Stark shifts on both Rydberg and ground states. For the following measurements and calculations, it is assumed the 780 nm trapping light is off during any Rydberg excitation and therefore does not contribute to any additional shifts.

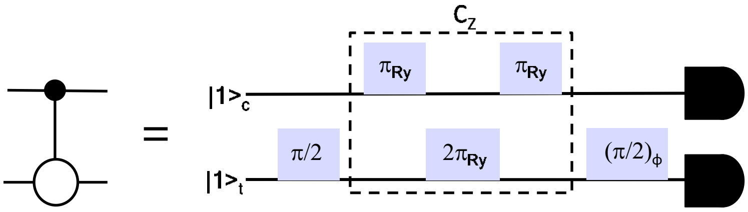

Figure 6.1: The CNOT gate using Rydberg blockade is implemented by sandwiching the C_Z operation with $\pi/2$-pulses on the target site. C_Z is implemented by a total of three Rydberg pulses. The phase of the second target $\pi/2$-pulse determines which CNOT gate is created.

6.1.1 Measuring beam intensities

In order to calculate all of the shifts induced by the Rydberg excitation beams we need to have good measurements of the beam intensities at the atoms. In principal, careful measurements of the beam waists and beam powers should give us accurate intensities. Not only are these measurements usually inaccurate but this also assumes the excitation beam waists are axially aligned perfectly to the atom when in reality this alignment could be $\sim 10 - 20$ μm off. A series of Ramsey and Rabi flopping experiments can be used to determine the single photon Rabi frequencies and thus the beam intensities experimentally. Recall from Chapter 4 that a two level system rotated to the equator by a $\pi/2$-pulse will precess at a frequency equal to the detuning. The detuning in this case is the differential Stark shift induced by the excitation beams. Measuring the frequency of the resulting Ramsey fringes is thus a direct measurement of the differential Stark shift from which the single photon Rabi frequencies and intensities can be inferred. A microwave Ramsey sequence is used to measure Ω_1, as defined in Fig. 6.2, by turning 459 nm light on in between two microwave $\pi/2$-pulses. This sequence measures the differential Stark shift of the ground state which is equal to the difference between the resonant Stark shift on $|1\rangle$ and $|0\rangle$ which are separated by the hyperfine frequency, ω_q,

$$\Delta_1^{\text{diff},g} = \frac{1}{8\pi}\left(\frac{\Omega_1^2}{\Delta_1} - \frac{\Omega_1^2}{\Delta_1 - \omega_q}\right). \tag{6.5}$$

In general, the hyperfine splitting of the intermediate level needs to be included into this equation as was discussed in section 4.3 and section 5.1.1. For simplicity here I will use the fine structure

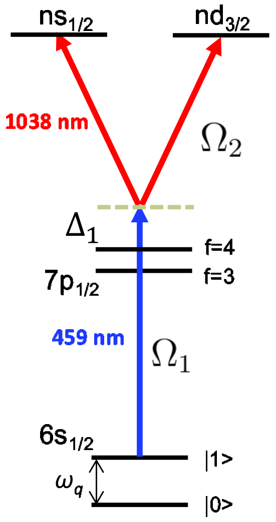

Figure 6.2: Rydberg Level Diagram

approximation as the detunings used in the experiments in this chapter are large enough for the approximation to be valid but in general the equations of section 4.3 and section 5.1.1 should be used. Through the Ramsey experiment we measure this frequency, $\Delta_1^{\text{diff},g}$, from which we can infer Ω_1 since Δ_1 and ω_q are known. In principal the same method can be used to extract Ω_2 but the differential shift on the ground state from the 1038 nm beam is small, about 200 Hz. Instead a Rydberg Rabi flopping experiment is performed, as was discussed in Chapter 5. The two photon Rydberg Rabi frequency in the fine structure limit is equal to

$$\Omega_R = \frac{\Omega_1 \Omega_2}{2\Delta_1}. \tag{6.6}$$

Since Ω_1 is now known and Ω_R is measured, Ω_2 can be inferred. As a consistency check, a measurement of the ground-Rydberg differential shift, $\Delta_{\text{ac},r} - \Delta_{\text{ac},g}$, via a Rydberg Ramsey measurement is also performed. Note this is the same measurement that gave us the ground-Rydberg coherence time in Chapter 5.

Fig. 6.3 shows the experiments that are done in order to determine the parameters needed for calculating the gate phases using the Rydberg $82s_{1/2}$ state with a detuning, $\Delta_1 = -2\pi \times 2.2$ GHz, measured from the center of mass of the $7p_{1/2}$ level. From Fig. 6.3(a) the frequency of the 459 nm

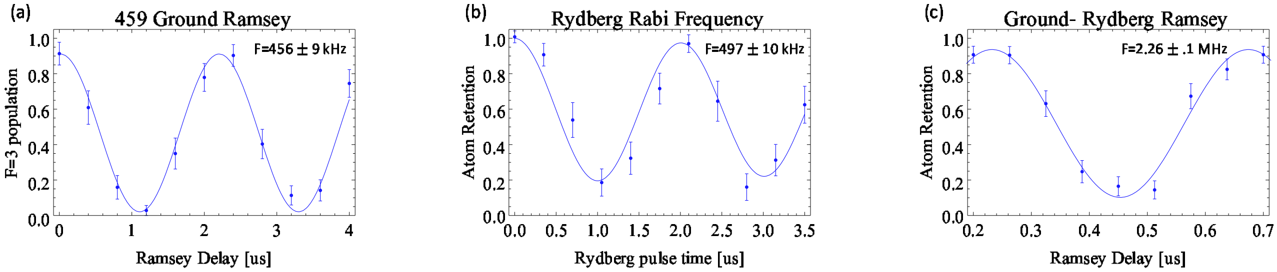

Figure 6.3: Example of the experiments used to find the relevant parameters for calculating the gate phases. (a) 459 Ground Ramsey experiment used to extract Ω_1. Experimental data from 201_10_27_11_08_20. (b) Rydberg Rabi flopping experiment used to extract Ω_2 once Ω_1 is known. Data from 2014_11_03_17_05_32. (c) Ground-Rydberg Ramsey experiment used to measured the differential shift of the ground-Rydberg transition due to the Stark shifts from the excitation beams. This measurement is used as a consistency check. Data from 2014_11_12_16_30_07.

ground state Ramsey gives $\Delta_1^{\text{diff},g} = 2\pi \times 456$ kHz. From this we can calculate a value for $\Omega_1 = 2\pi \times 70$ MHz and thus $|E_1|$ can be inferred. Fig. 6.3 (b) shows a measurement of the two photon Rydberg Rabi frequency found to be $\Omega_R = 2\pi \times 497$ kHz. This value allows us to calculate $\Omega_2 = 2\pi \times 31$ MHz and thus $|E_2|$. We can now use these parameters to calculate all of the relevant Stark shifts that will contribute to the phases of equation (6.4). The frequency extracted from ground-Rydberg Ramsey experiment as seen in Fig.6.3(c) should be consistent with the sum of the shifts which are calculated in the following section 6.1.2.

6.1.2 Calculating Stark shifts

The ground state experiences a resonant ac Stark shift from the 459 nm light and a non-resonant shift from the 459 nm and 1038 nm light. Table 6.1 summarizes and calculates the shifts using as an example the parameters found in section 6.1.1, which represent typical parameters used in our gate experiments.

Resonant 459 shift on $\|1\rangle$	$\frac{1}{4}(\frac{\Omega_1^2}{\Delta_1})$	$-2\pi\times560$ kHz
Resonant 459 shift on $\|0\rangle$	$\frac{1}{4}(\frac{\Omega_1^2}{\Delta_1-\omega_q})$	$-2\pi\times110$ kHz
Non-resonant ground 459 shift	$-\frac{1}{4\hbar}\alpha_{\mathrm{g},1}\|E_1\|^2$	$2\pi\times1$ kHz
Non-resonant ground 1038 shift	$-\frac{1}{4\hbar}\alpha_{\mathrm{g},2}\|E_2\|^2$	$-2\pi\times1.2$ MHz
Total ground shift on $\|1\rangle$		$-2\pi\times1.8$ MHz
Rydberg free electron shift 459	$-\frac{1}{4\hbar}\alpha_{r,1}\|E_1\|^2$	$2\pi\times1.5$ kHz
Rydberg free electron shift 1038	$-\frac{1}{4\hbar}\alpha_{r,2}\|E_2\|^2$	$2\pi\times500$ kHz
Rydberg shift Resonant 1038	$\frac{1}{4}(\frac{\Omega_2^2}{\Delta_1})$	-$2\pi\times110$ kHz
Total Rydberg shift		$2\pi\times392$ kHz
Total Differential Shift		$2\pi\times2.2$ MHz

Table 6.1: Summary of the different Stark shifts for the parameters: $\Omega_1 = 2\pi \times 70$ MHz, $\Omega_2 = 2\pi \times 31$ MHz, and $\Delta_1 = -2\pi \times 2.2$ GHz, $82S_{1/2}$. The fine structure approximation is used here. Adding in the hyperfine structure of the intermediate level will change these numbers by less than 0.5%.

Here $\alpha_{\mathrm{g},1(2)}$ are the non-resonant ground state polarizabilities at 459(1038) nm. Non-resonant Rydberg polarizabilities are calculated using the free electron polarizability

$$\alpha_{rj} = -\frac{e^2}{m_e\omega_j^2}, \tag{6.7}$$

where e and m_e are the electron charge and mass, respectively and ω_j is the driving field frequency. Here we also include the resonant 1038 nm shift on the Rydberg state. The relevant non-resonant polarizabilities in CGS units are

$$\begin{aligned}\alpha_{\mathrm{g},1} &= -11.6\text{Å}^3,\\ \alpha_{\mathrm{g},2} &= 188.81\text{Å}^3,\\ \alpha_{r,1} &= -15\text{Å}^3,\\ \alpha_{r,2} &= -76.90\text{Å}^3.\end{aligned} \tag{6.8}$$

From Table 6.1 we can see for the given parameters, the ground state experiences a net shift down while the Rydberg state is shifted up. The sum of these shifts results in a positive differential shift on the ground-Rydberg transition of $2\pi \times 2.3$ MHz which agrees with what was measured in Fig. 6.3(c).

6.1.3 Shift from a 2π rotation

In the case of a two level system driven by a single field the ground state accumulates a shift of $e^{i\pi} = -1$ during a resonant 2π-pulse. The situation is complicated for the three level system driven by two fields. The laser frequencies are tuned to give full population transfer from the ground state to the excited state. This means the detuning includes the Stark shifts from each of the excitation beams. Derived in Chapter 5, the resonance condition occurs when

$$\Delta_+ = \Delta + \frac{|\Omega_1|^2}{2\delta} - \frac{|\Omega_2|^2}{2\delta} = 0, \tag{6.9}$$

for $\delta = \Delta_1 - \Delta_2$ and $\Delta = \Delta_1 + \Delta_2$. This resonance condition can be rewritten as

$$\Delta(2\Delta_1 - \Delta) + \frac{|\Omega_1|^2}{2} + \frac{|\Omega_2|^2}{2} = 0. \tag{6.10}$$

In the limit where Δ is small as to be close to resonance but Δ_1 is large to minimize spontaneous emission from the intermediate level we can take $\delta \approx 2\Delta_1$ and the above equation is solved for Δ

$$\Delta \approx \frac{|\Omega_2|^2 - |\Omega_1|^2}{4\Delta_1} \equiv \Delta_{\rm ac}. \tag{6.11}$$

Using $\Delta = \Delta_{\rm ac}$ as our operational detuning we can calculate, using results from Chapter 5, the phase accumulated by the ground state during a 2π Rydberg pulse

$$\begin{aligned} \phi_{\rm Ryd} &= \pi + \frac{\Delta - \Delta_-}{2} 2t_\pi \\ &\approx \pi - \frac{|\Omega_1|^2}{2\Delta_1}\frac{\pi}{|\Omega_{\rm R}|} \\ &= \pi\Big[1 - \Big|\frac{\Omega_1}{\Omega_2}\Big| {\rm sign}(\Delta_1)\Big]. \end{aligned} \tag{6.12}$$

This gives the counterintuitive result that there is exactly 0 (2π) phase shift in the balanced situation when $\Omega_1 = \Omega_2$.

We must also include in this calculation the non-resonant shifts discussed in section 6.1.2. The solutions found for the probability amplitudes in Chapter 5 are still valid provided we use modified detunings, Δ_1' and Δ_2', which now include the non-resonant shifts

$$\begin{aligned}\Delta_1' &= \Delta + \frac{|\Omega_1|^2}{\delta} + 2\Delta_{g1}^{\rm nr} + 2\Delta_{g2}^{\rm nr},\\ \Delta_2' &= \Delta - \frac{|\Omega_2|^2}{\delta} - 2\Delta_{r1}^{\rm nr} - 2\Delta_{r2}^{\rm nr}.\end{aligned} \tag{6.13}$$

The non-resonant shifts on the ground (Rydberg) states, $\Delta_{g(r)}^{\rm nr}$, are the same as in tables 6.1:

$$\begin{aligned}\hbar\Delta_{g1}^{\rm nr} &= -\frac{1}{4}\alpha_{\rm g,1}|E_1|^2\\ \hbar\Delta_{g2}^{\rm nr} &= -\frac{1}{4}\alpha_{\rm g,2}|E_2|^2\\ \hbar\Delta_{r1}^{\rm nr} &= -\frac{1}{4}\alpha_{r,1}|E_1|^2\\ \hbar\Delta_{r2}^{\rm nr} &= -\frac{1}{4}\alpha_{r,2}|E_2|^2\end{aligned} \tag{6.14}$$

The modified resonance condition then becomes

$$\Delta \approx \frac{|\Omega_2|^2 - |\Omega_1|^2}{4\Delta_1} + \Delta_{r1}^{\rm nr} + \Delta_{r2}^{\rm nr} - \Delta_{g1}^{\rm nr} - \Delta_{g2}^{\rm nr}. \tag{6.15}$$

Including non-resonant shifts the phase acquired by the ground state during a 2π resonant Rydberg pulse is

$$\phi_{\rm Ryd} = \pi\Big[1 - \Big|\frac{\Omega_1}{\Omega_2}\Big|{\rm sign}(\Delta_1)\Big] - 2(\Delta_{g1}^{\rm nr} + \Delta_{g2}^{\rm nr})t_\pi. \tag{6.16}$$

6.1.4 Phase accumulation on the computational basis states

Now we understand where all the various shifts can come from let us construct the C_ϕ gate by considering how these shifts affect the computational basis states, $|ct\rangle = |00\rangle, |01\rangle, |10\rangle, |11\rangle$.

For the $|00\rangle$ state the excitation beams are 9.2 GHz detuned for both sites so both remain in the $|00\rangle$ state. The beams do, however, induce an off-resonant Stark shift on each atom for a time, $2t_\pi = 2\pi/|\Omega_R|$. This shift will be denoted as $\phi_{{\rm hf},c(t)}$. From Table 6.1, the shifts on $|0\rangle$ include the resonant 459 nm shift and the non-resonant 459 nm and 1038 nm shifts. In other words

$$\phi_{00} = \phi_{{\rm hf},c} + \phi_{{\rm hf},t}, \tag{6.17}$$

where

$$\phi_{{\rm hf},c(t)} = -2[\frac{|\Omega_{1,c(t)}|^2}{4(\Delta_1 - w_q)} + \Delta_{g1,c(t)}^{\rm nr} + \Delta_{g2,c(t)}^{\rm nr}]t_\pi. \tag{6.18}$$

For the $|01\rangle$ state, the control experiences the off-resonant Stark shift, $\phi_{\mathrm{hf},c}$, while the target picks up a phase shift from the resonant Rydberg 2π-pulse, ϕ_{Ryd} from equation (6.16)

$$\phi_{01} = \phi_{\mathrm{hf},c} + \phi_{\mathrm{Ryd},t}. \tag{6.19}$$

The $|10\rangle$ state is different than the $|01\rangle$ state because the control atom is held in the Rydberg state for a time $2t_\pi$ during the target pulse. This adds yet an additional phase denoted as ϕ_{gap} which includes the ground-Rydberg differential Stark shift

$$\phi_{\mathrm{gap}} = -2\Big[\big(\frac{|\Omega_{2,c}|^2}{4(\Delta_1)} + \Delta^{\mathrm{nr}}_{r1,c} + \Delta^{\mathrm{nr}}_{r2,c}\big) - \big(\frac{|\Omega_{1,c}|^2}{4(\Delta_1)} + \Delta^{\mathrm{nr}}_{g1,c} + \Delta^{\mathrm{nr}}_{g2,c}\big)\Big](t_{\mathrm{gap}} + t_\pi). \tag{6.20}$$

Here t_{gap} is the extra time in between pulses which, experimentally, is the minimum time it takes to switch sites limited by the AOMs in the beam scanner. In total the shift on the $|10\rangle$ state is

$$\phi_{10} = \phi_{\mathrm{Ryd},c} + \phi_{\mathrm{gap}} + \phi_{\mathrm{hf},t}. \tag{6.21}$$

Finally the $|11\rangle$ state experiences an additional shift due to the blockade, ϕ_{B}, for a time $2t_\pi$ which includes the resonant Stark shift of 459 nm beam plus the non-resonant shifts on the $|1\rangle$ state

$$\phi_{\mathrm{B}} = -2\Big[\frac{|\Omega_{1,t}|^2}{4\Delta_1} + \Delta^{\mathrm{nr}}_{g1,t} + \Delta^{\mathrm{nr}}_{g2,t}\Big] t_{\pi,t}, \tag{6.22}$$

giving the final expression for the phase accumulation on the $|11\rangle$ state during the gate sequence

$$\phi_{11} = \phi_{\mathrm{Ryd},c} + \phi_{\mathrm{gap}} + \phi_{\mathrm{B}}. \tag{6.23}$$

As an example, to show that the result of these shifts are not equal to the ideal C_Z of equation (6.1), plugging in the parameters extracted from section 6.1.1 the resulting two qubit operator is

$$C_\phi = \begin{pmatrix} e^{i0.28\pi} & 0 & 0 & 0 \\ 0 & e^{-i0.87\pi} & 0 & 0 \\ 0 & 0 & e^{-i0.5\pi} & 0 \\ 0 & 0 & 0 & e^{-i0.35\pi} \end{pmatrix}. \tag{6.24}$$

Sandwiching C_ϕ in between two $\pi/2$ ground state pulses on the target atom will not result in a CNOT$_1$ or CNOT$_2$. However, by controlling the phase of the second ground state pulse we

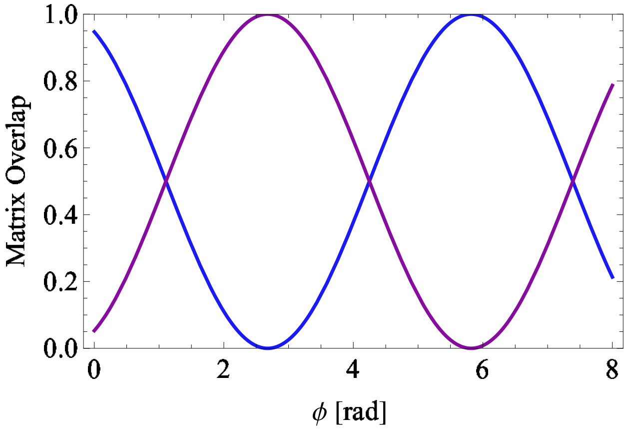

Figure 6.4: Simulated CNOT matrix overlap, $\frac{1}{4}\sum\limits_{elements}(\mathrm{CNOT_{ideal}}|\mathrm{CNOT}_\phi|)^2$, as a function of the phase of the second ground state pulse for parameters extracted from 6.1.1: $\Omega_1 = 2\pi \times 70$ MHz, $\Omega_2 = 2\pi \times 31$ MHz, and $\Delta_1 = -2\pi \times 2.2$ GHz, $82s_{1/2}$.

can maximize the matrix overlap with the ideal CNOT where the matrix overlap is computed as $O(\mathrm{CNOT_{ideal}}, \mathrm{CNOT}_\phi) \equiv \frac{1}{4}\sum\limits_{elements}(\mathrm{CNOT_{ideal}}|\mathrm{CNOT}_\phi|)^2$. Defining

$$\mathrm{CNOT}_\phi \equiv R_t(\pi/2, \phi)C_\phi R_t(\pi/2, 0), \tag{6.25}$$

where $R_{c(t)}(\theta, \phi)$ is a ground state rotation on the control(target) by an angle, θ, with phase, ϕ, we find unity overlap with CNOT_1 and CNOT_2 for phase angles defined above

$$\begin{aligned} O(\mathrm{CNOT}_1, \mathrm{CNOT}_{\phi_{11}-\phi_{10}}) &= 1, \\ O(\mathrm{CNOT}_2, \mathrm{CNOT}_{\phi_{01}-\phi_{00}}) &= 1. \end{aligned} \tag{6.26}$$

Note that this overlap is not a gate fidelity and does not contain any phase information. For example, using the C_ϕ found in equation (6.24) we find

$$\mathrm{CNOT}_{\phi_{11}-\phi_{10}} = \begin{pmatrix} e^{i0.28\pi} & 0 & 0 & 0 \\ 0 & e^{-i0.86\pi} & 0 & 0 \\ 0 & 0 & 0 & e^{i\pi} \\ 0 & 0 & e^{i0.85\pi} & 0 \end{pmatrix}. \tag{6.27}$$

Fig. 6.4 shows the overlap of CNOT_ϕ created with C_ϕ with the two different ideal CNOT gates as a function of the ground state phase, ϕ. For Fig. 6.4, the parameters from section 6.1.1 are used. The free parameters are the beam powers and waists, P_1, P_2, w_1, w_2 for each of the sites, the detuning Δ_1, the Rydberg level and the gap time between pulses, $t_{\rm gap}$. If we leave these parameters undefined we can always find the phase of the second pulse that gives a matrix overlap with an ideal CNOT equal to 1. The difference between the phases of the two CNOT gates independent of their parameters is always

$$\begin{aligned} \phi_{11} - \phi_{10} - (\phi_{01} - \phi_{00}) &= -\phi_{{\rm Ryd},t} + \phi_{\rm B} \\ &= -\pi. \end{aligned} \tag{6.28}$$

6.2 CNOT gate-experimental results

6.2.1 Next nearest neighbors, $82s_{1/2}$

From section 6.1.4 it is clear that setting the correct phase of the second ground state pulse is crucial to running the gate. This is found experimentally by using the sequence seen in Fig. 6.5(a). A global ground state π-pulse is added at the end in order to make a $|1\rangle$ measurement. The data in Fig. 6.5(b) was run with parameters extracted from section 6.1.1 using a control and target that are two sites away so that their separation is 7.6 μm. The plot in Fig. 6.5(b) shows the single atom data of the target atom which is cut on whether a control atom is present or not. The red curve shows the data when a control atom is present and therefore the Rydberg blockade occurs. While this is only single atom data, this curve can be thought of as representing the $|11\rangle$ input state and if we wish to run the CNOT$_1$ gate, we choose the phase where this curve is minimum so that $|11\rangle$ goes to $|10\rangle$. The blue curve shows the data when a control atom is not present when no blockade occurs. These two curves should always be shifted from on another by a relative phase equal to π.

For the data presented in Fig. 6.5(b), the two $\pi/2$-pulses are executed using the Stark shifting microwave pulse method described in Chapter 4. The parameters are the same as in the previous section.

The data of Fig. 6.5(b) should agree with the simulations of Fig. 6.4. There appears, however, to be a phase shift between the experimental and theoretical case of approximately 1.24 radians. In the case of the CNOT$_1$ the phase we are concerned with is $\phi_{11} - \phi_{10}$. In terms of experimental

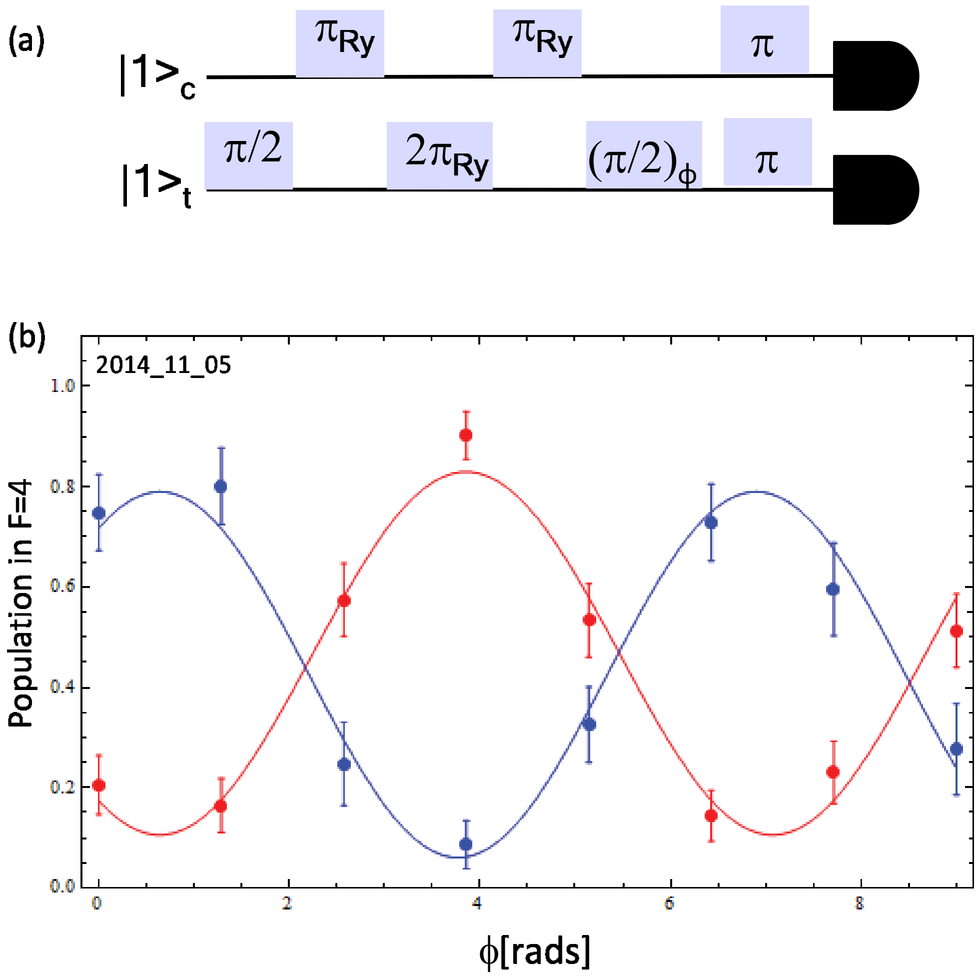

Figure 6.5: (a) Sequence for CNOT eye diagram experience which is used to find the phase at which to run the gate. (b)Experimental CNOT eye diagram for parameters $\Omega_1 = 2\pi \times 70$ MHz, $\Omega_2 = 2\pi \times 31$ MHz, and $\Delta_1 = -2\pi \times 2.2$ GHz, $82s_{1/2}$, next nearest neighbors. The red data is the results of the target cut on there being a control atom loaded and represents the blockaded data set. The blue is cut on there being no control loaded. The two curves should always have a π phase shift with respect to one another. The phase offset from 0 is a result of the Stark shifts described earlier in this chapter. The phases which give the minimum for the red curve are the phases which give the CNOT$_1$ operation and should be equal to $\phi_{11} - \phi_{10}$. Experimental data from 2014_11_05_10_01_13

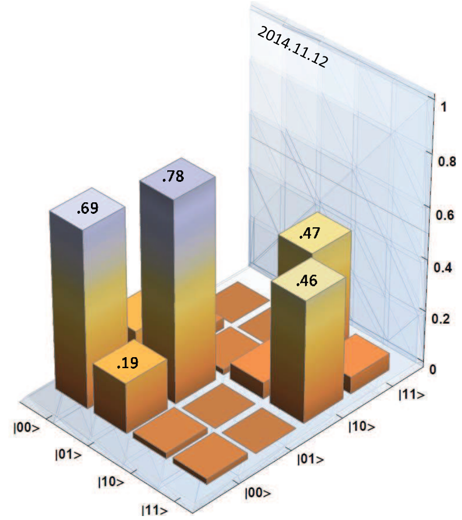

Figure 6.6: CNOT gate populations on next nearest neighbor sites with parameters $\Omega_1 = 2\pi \times 70$ MHz, $\Omega_2 = 2\pi \times 31$ MHz, and $\Delta_1 = -2\pi \times 2.2$ GHz, $82s_{1/2}$. Data from 2014_11_12_09_42_24, 2014_11_12_10_08_11, 2014_11_12_10_36_18 and 2014_11_12_11_03_14.

parameters this phase occurs at

$$\begin{aligned}\phi_{11} - \phi_{10} &= \phi_{\rm B} - \phi_{\rm hf,t} \\ &= \pi \left|\frac{\Omega_1}{\Omega_2}\right| \text{sign}(\Delta_1) \frac{\omega_q}{\Delta_1 - \omega_q}.\end{aligned} \tag{6.29}$$

If the two beam intensities and the detuning are adjusted by 15% the measured phase is recovered.

To measure the CNOT gate population matrix, each of the computational states are prepared and measured. This result is seen in Fig. 6.6. Note that the sum of the fidelities in a given row or column is not equal to one as expected. This loss is currently not well understood and is the main factor limiting our fidelity at the moment. This will be discussed further in section 6.5.

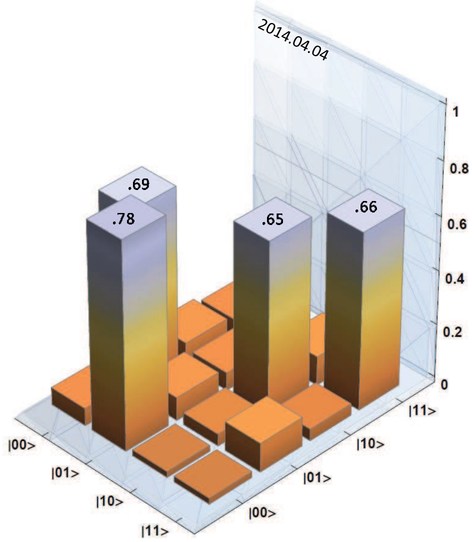

Figure 6.7: CNOT gate populations on diagonally neighboring site for parameters $\Omega_1 = 2\pi \times 41$ MHz, $\Omega_2 = 2\pi \times 101$ MHz and $\Delta_1 = -2\pi \times 2.42$ GHz, $70d_{3/2}$. Data from 2014_04_05_00_27_11, 2014_04_05_00_14_30, 2014_04_05_00_01_34 and 2014_04_04_23_32_15.

6.2.2 Diagonal neighbors, $70d_{3/2}$

Similar results were observed for two diagonally neighboring sites, 5.4 μm apart, using the $70d_{3/2}$ Rydberg state. The approximate parameters give $\Omega_1 = 2\pi \times 41$ MHz, $\Omega_2 = 2\pi \times 101$ MHz and $\Delta_= -2\pi \times 2.42$ GHz. This results in an $\Omega_R = 2\pi \times 850$ kHz with a ground-Rydberg differential shift of $2\pi \times 2.8$ MHz. The CNOT population matrix is shown in Fig. 6.7. This is an example of the CNOT$_2$ gate. It should be emphasized that the contrast between the high and low states is quite good. The overall loss in population is currently limiting the gate as opposed to errors in the operations.

6.3 Bell states and Entanglement

The CNOT gate is used to create Bell states and thus two qubit entanglement. To create a Bell state, a ground state $\pi/2$-pulse is added to the control at the beginning of the sequence shown in

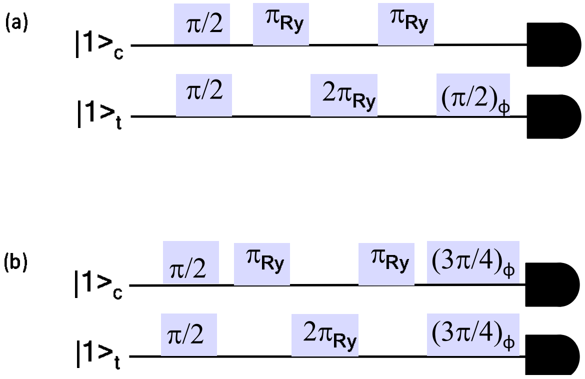

Figure 6.8: The two methods used for creating Bell states. (a) The standard method involves only $\pi/2$ ground state pulses. For the last ground state pulse single site addressing on the target is needed therefore this is called the“Stark method”. (b) Replacing the last ground state $\pi/2$ pulse with a global $3\pi/4$ pulse allows all ground state pulses to be implemented globally. This is denoted as the “$3\pi/4$ method”.

Fig. 6.8 (a). Alternatively, the Bell states can be created using the circuit seen in Fig. 6.8, by replacing the last ground state target $\pi/2$-pulse with a global $3\pi/4$-pulse. This method allows all ground state pulses to be executed using the global microwaves only.

The next step after the Bell state creation is entanglement verification. To verify entanglement one must measure the complex coherences of the density matrix of the entangled state. In general, a two qubit density matrix has the following form

$$\rho = \begin{pmatrix} P_{00} & B_1 & A_1 & C_1 \\ B_1^* & P_{01} & C_2 & A_2 \\ A_1^* & C_2^* & P_{10} & B_2 \\ C_1^* & A_2^* & B_2^* & P_{11} \end{pmatrix}. \tag{6.30}$$

Here the diagonal elements represent the real populations and the off diagonal elements are the complex coherences. To see the importance in measuring the coherences consider, for example, the Bell state $|B_1\rangle = \frac{|00\rangle+|11\rangle}{\sqrt{2}}$. The density matrix, $|B_1\rangle\langle B_1|$, for the state is

$$\rho_B = \begin{pmatrix} 1/2 & 0 & 0 & 1/2 \\ 0 & 0 & 0 & 0 \\ 0 & 0 & 0 & 0 \\ 1/2 & 0 & 0 & 1/2 \end{pmatrix}. \tag{6.31}$$

Now consider the separable state which is a classically correlated mixture of both atoms being in $|0\rangle$ with 50% probability and both atoms being in $|1\rangle$ with 50% probability,

$$\rho_M = \frac{1}{2}\rho_{00} + \frac{1}{2}\rho_{11} = \begin{pmatrix} 1/2 & 0 & 0 & 0 \\ 0 & 0 & 0 & 0 \\ 0 & 0 & 0 & 0 \\ 0 & 0 & 0 & 1/2 \end{pmatrix}. \tag{6.32}$$

Both density matrices look identical when looking only at the populations, P_{00} and P_{11}. This demonstrates the importance of measuring the coherences when verifying entanglement. Furthermore, the criterion for entanglement can be derived. An arbitrary separable pure state for two atoms labeled C and T can be written as

$$|\psi\rangle = (c_0|0\rangle + c_1|1\rangle)_C \otimes t_0|0\rangle + t_1|1\rangle)_T. \tag{6.33}$$

This state must satisfy both normalization conditions $|c_0|^2 + |c_1|^2 = 1$ and $|t_0|^2 + |t_1|^2 = 1$ which combine to give

$$|c_0|^2 + |c_1|^2 + |t_0|^2 + |t_1|^2 = 2. \tag{6.34}$$

This condition is rearranged to

$$(|c_0| - |c_0|)^2 + (|t_1| - |t_1|)^2 + 2|c_0||t_0| + 2|c_1||t_1| = 2. \tag{6.35}$$

Since the first two terms are always positive or zero we can derive the condition

$$|c_0||t_0| + |c_1||t_1| \leq 1, \tag{6.36}$$

and

$$(|c_0||t_0| + |c_1||t_1|)^2 \leq 1. \tag{6.37}$$

Expanding this out and noting that $|c_i|^2|t_j|^2 = P_{ij}$ and $|c_0||t_0||c_1||t_1| = |C_1|$ we derive the condition necessary for a density matrix to represent a separable state

$$P_{00} + P_{11} + 2|C_1| \leq 1. \tag{6.38}$$

Define the entanglement fidelity as $F = \frac{1}{2}(P_{00} + P_{11}) + |C_1|$. If $F > 1/2$ the state is entangled. Similarly one can derive the condition for the other bell states: $F = \frac{1}{2}(P_{01} + P_{10}) + |C_2| > 1/2$. To verify entanglement and measure the fidelity of the entangled state we created we need to measure the populations and the coherence terms C_1 or C_2.

One can do this by fully reconstructing the density matrix via two qubit quantum state tomography. This involves taking measurements in the x and y basis. State tomography on a single qubit involves six measurements. The two qubit state tomography needed for entanglement verification involves 36 measurements. This procedure takes a long time and will give us more information than we necessarily need for entanglement verification.

Alternatively, the coherence can be measured by observing parity oscillations. Applying a rotation, $R_{c(t)}(\theta, \phi)$, to each of our qubits C and T will evolve the density matrix to $\rho' \rightarrow R\rho R^\dagger$ where $R = R_c \otimes R_t$. Define a parity signal $P = P_{00} + P_{11} - P_{01} - P_{10}$. After the rotation, R, the parity signal become $P' = P'_{00} + P'_{11} - P'_{01} - P'_{10}$. Choosing the rotation angle as $\theta = \pi/2$ and allowing ϕ to vary, this signal simplifies to

$$P' = C_2 + C_2^* - C_1^* e^{-2i\phi} - C_1 e^{2i\phi} = 2Re[C_2] - 2|C_1|\cos(2\phi + \xi). \tag{6.39}$$

for $C_1 = |C_1|e^{i\xi}$. The parity signal oscillates with an amplitude of $2|C_1|$. By preparing a Bell state then applying a $\pi/2$ pulse with varying phase, ϕ, parity oscillations are observed. From this the coherence can be extracted and thus, in combination with the populations, the entanglement fidelity is found.

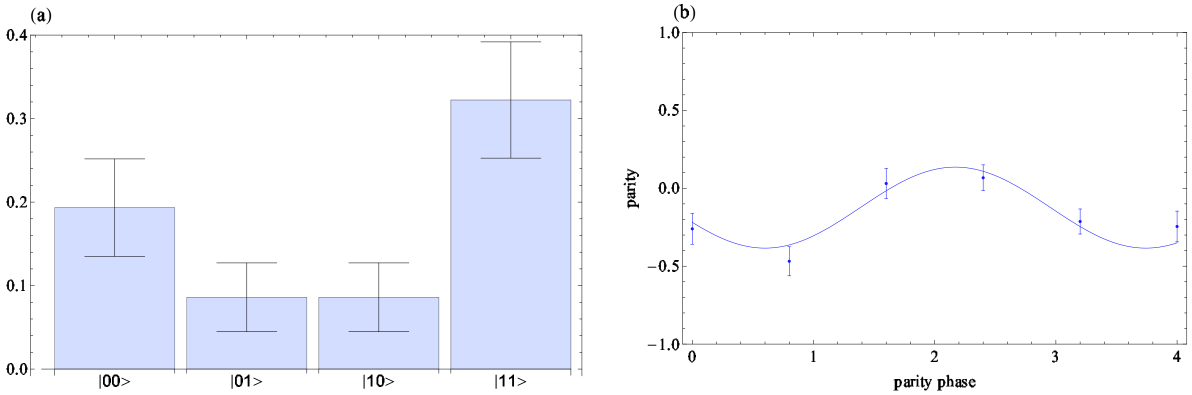

Figure 6.9: (a) Bell state population measurement and (b) parity oscillation measurement using next nearest neighbor sites separated by 7.9 μm with the parameters $\Omega_1 = 2\pi \times 70$ MHz, $\Omega_2 = 2\pi \times 31$ MHz, and $\Delta_1 = -2\pi \times 2.2$ GHz, $82s_{1/2}$. For (a) the populations measured for the Bell state are $|00\rangle$: 0.18 ± 0.05, $|01\rangle$: 0.08 ± 0.04, $|10\rangle$: 0.08 ± 0.04, $|11\rangle$: 0.3 ± 0.06 Data from 2014_11_05_10_48_10. The fit to the parity curve in (b) gives a value $C_1 = 0.13 \pm 0.04$. Data from 2014_11_05_18_28_53. This gives an entanglement fidelity $F = 0.37 \pm 0.06$ which is under threshold for entanglement. This data has not been corrected for any type of atom loss.

6.3.1 Experimental results: $82s_{1/2}$

The Bell state population and parity experiment described above is executed with the parameters found in section 6.1.1 using the $3\pi/4$ method. This data is taken on next nearest neighbors, separated by 7.9 μm, using the $82s_{1/2}$ Rydberg state. The results of Fig. 6.9 clearly shows evidence of the $|00\rangle + |11\rangle$ state with parity oscillations, but still gives an entanglement fidelity below threshold at $F = 0.37 \pm 0.06$.

With the estimated parameters we can calculate the expected Bell state populations and parity oscillations. Define $|B_{\rm Stark}\rangle$ as the Bell state created using the circuit from Fig. 6.8 (a) and $|B_{3\pi/4}\rangle$ from circuit (b). The Bell state fidelities are calculated as the overlap with the desired state

$$F = |\langle B_{ideal}|B\rangle|^2. \tag{6.40}$$

Using the Stark shifting method and equation (6.24) we find a Bell state fidelity equal to $F = 0.988$ with $|B_{ideal}\rangle = \frac{1}{\sqrt{2}}(|00\rangle - |11\rangle)$. For the $3\pi/4$ method this overlap is only $F = 0.64$ with

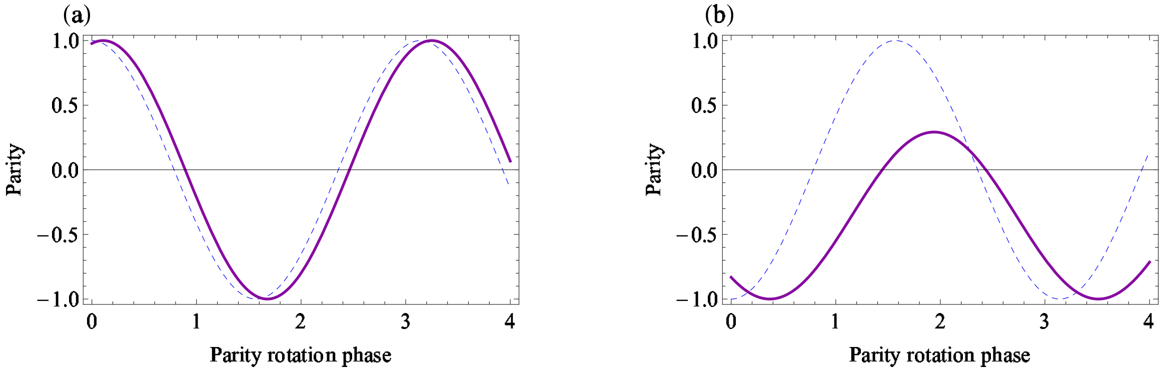

Figure 6.10: Parity oscillation simulations using the Bell states created using the C_Z gate from equation (6.24) using the experimental parameters found in section 6.1.1. Simulations are done for both Bell states created using the (a) single site Stark shifting method and (b) the global microwave $3\pi/4$ method. In both cases the ideal case is represented by the dashed curve.

$|B_{ideal}\rangle = \frac{1}{\sqrt{2}}(|00\rangle + |11\rangle)$. Fig. 6.10 shows simulated parity oscillations given these Bell states created using the C_Z gate of equation (6.24), where the dashed curve in each case is the ideal case. In both cases a small phase shift is observed but only for the $3\pi/4$ method is the amplitude significantly reduced and the offset from zero shifted. This implies this method is not good for the chosen set of parameters. All simulations ignore finite blockade effects, spontaneous emission, atom loss, dephasing and assume both atoms use exactly the same parameters. The effect of using $3\pi/4$ method as simulated in Fig. 6.10 (b) was unknown at the time data from Fig. 6.9 was taken. This could contribute to the infidelity. Also the fidelity should be limited by the atom loss as the populations of the Bell state only add up to 0.69.

Close attention should be paid to the parameter t_{gap}. The simulations (and experiments) above have t_{gap} set to 500 ns. According to Fig. 6.11, scanning t_{gap} recovers an ideal Bell state, $F = 1.0$, in the Stark shifting method. However, t_{gap} must be changed by 7 ns from its nominal value which is below the 25 ns resolution of digital I/O which controls the pulse timings. Using the $3\pi/4$ method, if an additional phase shift of $-\phi_{\text{gap}}$ is added to the second ground state pulse, a Bell state with $F = 0.998$ can be recovered if t_{gap} is changed to 438 ns.

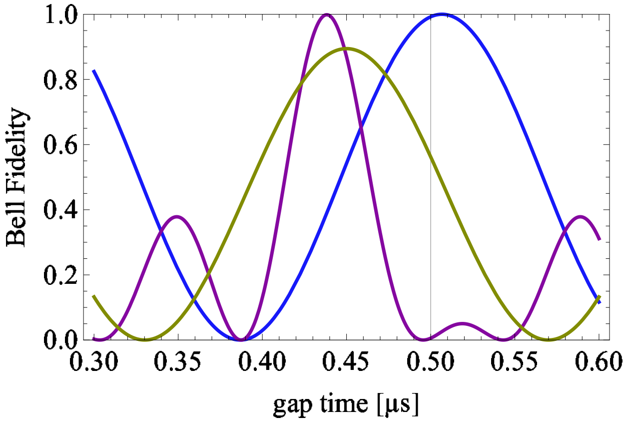

Figure 6.11: Bell state fidelity simulations as a function of t_{gap} using the different methods. Parameters used for simulations are $\Omega_1 = 2\pi \times 70$ MHz, $\Omega_2 = 2\pi \times 31$ MHz, and $\Delta_1 = -2\pi \times 2.2$ GHz, $82s_{1/2}$. The vertical line represents the nominal value of t_{gap} equal to 500 ns. The blue curve represents the Stark shifting method. The gold curve is the $3\pi/4$ method and the pink curve is the $3\pi/4$ method with an additional phase of $-\phi_{\text{gap}}$ added to global $3\pi/4$ pulse.

In section 6.4 we will show how to set the parameters including, t_{gap}, to recover and ideal C_Z and thus ideal entanglement fidelities.

6.3.2 Experimental results: $70d_{3/2}$

Bell state population and parity measurements are also done on diagonally neighboring sites separated by 5.4 μm using the $70d_{3/2}$ state. Fig. 6.12 shows these results using both Stark and $3\pi/4$ implementations for creating the Bell states. For the Stark shifting method, the entanglement fidelity is $F = 0.52 \pm 0.07$, above the threshold for entanglement. The $3\pi/4$ method gives an entanglement fidelity of $F = 0.47 \pm 0.06$, just at the threshold for entanglement. While the C_1 values from the parity oscillation is bigger for the $3\pi/4$ method, the larger loss in population, particularity in the $|11\rangle$ state results in a lower entanglement fidelity compared to the Stark shift method. Using these parameters, the expected Bell state populations and parity oscillations can be calculated as was done in the previous section. The calculated Bell state fidelity is found to be $F = 0.97$ using the Stark shifting method and $F = 0.70$ using the $3\pi/4$.

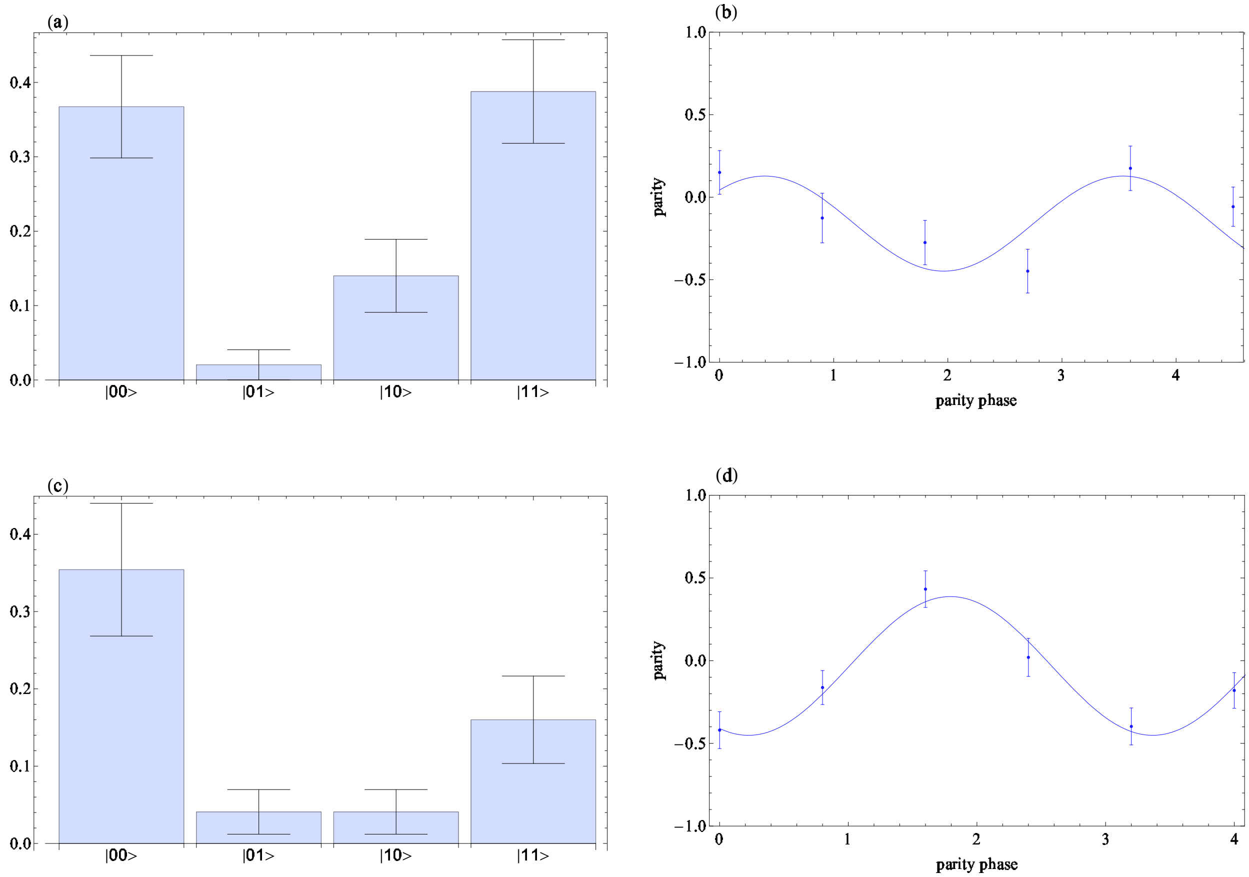

Figure 6.12: Bell state population and parity measurements using diagonal neighbors with parameters $\Omega_1 = 2\pi \times 41$ MHz, $\Omega_2 = 2\pi \times 101$ MHz and $\Delta_1 = -2\pi \times 2.42$ GHz,$70d_{3/2}$. The results using the different implementations are shown. (a) Bell state populations using the Stark shifting method. Measured populations are $|00\rangle$: 0.36±0.07, $|01\rangle$: 0.02±0.02, $|10\rangle$: 0.14±0.05, $|11\rangle$: 0.39±0.07. Data from 2014_04_04_21_07_34. (b) Resulting parity measurement fits $C_1 = 0.14 \pm 0.05$ giving an entanglement fidelity of $F = 0.52 \pm 0.07$. Data from 2014_04_04_22_33_01. (c) The $3\pi/4$ method is also used to create the same Bell state. Measured populations are $|00\rangle$: 0.35 ± 0.09, $|01\rangle$: 0.04 ± 0.02, $|10\rangle$: 0.04 ± 0.02, $|11\rangle$: 0.16 ± 0.06. Data from 2014_04_03_15_12_20. (d) Resulting parity measurement fits $C_1 = 0.21 \pm 0.04$ giving an entanglement fidelity equal to $F = 0.47 \pm 0.06$. Data from 2014_04_03_15_12_20.

6.4 Fine tuning parameters to recover ideal Cz

It is possible to find parameters for Ω_1, Ω_2, t_{gap}, and Δ_1 which perfectly recover the ideal C_Z gate of equation (6.1). Assume Ω_1 and Ω_2 are the same for both control and target atoms. If $\phi_{\text{Ryd}} = n\pi$ and $\phi_{\text{B}} = n'\pi$ where n is even and n' is odd, or vice versa, then the equations in section 6.1.4 become

$$\begin{aligned}
\phi_{00} =& 2\phi_{\text{hf}}, \\
\phi_{01} =& \phi_{\text{hf}} + n\pi, \\
\phi_{10} =& \phi_{\text{hf}} + n\pi + \phi_{\text{gap}}, \\
\phi_{11} =& \phi_{\text{gap}} + n\pi + n'\pi.
\end{aligned} \tag{6.41}$$

Note that $\phi_{\text{Ryd}} - \phi_{\text{B}} = \pi$ for any choice of parameters. Next it is possible to choose a time t_{gap} which makes $\phi_{\text{gap}} = 2\pi n''$ for any integer n''. Then the phases become

$$\begin{aligned}
\phi_{00} =& 2\phi_{\text{hf}}, \\
\phi_{01} =& \phi_{\text{hf}} + \pi, \\
\phi_{10} =& \phi_{\text{hf}} + \pi, \\
\phi_{11} =& \pi,
\end{aligned} \tag{6.42}$$

for n odd and n' even and

$$\begin{aligned}
\phi_{00} =& 2\phi_{\text{hf}}, \\
\phi_{01} =& \phi_{\text{hf}}, \\
\phi_{10} =& \phi_{\text{hf}}, \\
\phi_{11} =& \pi,
\end{aligned} \tag{6.43}$$

for n even and n' odd. The ϕ_{hf} phases can be corrected by applying global Z rotations with $\theta = -\phi_{\text{hf}}$. Then up to an overall phase, the ideal C_Z of equation (6.1) is recovered.

The questions is if we can find values for Ω_1, Ω_2, and t_{gap} which satisfy the above conditions and exist within our reachable parameter space. At a fixed detuning Ω_1 and Ω_2 are limited by available laser power. A lower limit for t_{gap} is set by the switching times of the scanners, around 500 ns. An upper limit is set by the fact that the traps are turned off during the gate sequence which can eventually lead to loss of ground state atoms due to their finite temperature. The condition, $\phi_{\mathrm{B}} = n'\pi$, can be rewritten as

$$r^2\mathrm{sign}(\Delta_1) - \hbar|\Delta_1|\Big(\frac{\alpha_{\mathrm{g},1}}{|d_{eg}|^2}r^2 + \frac{\alpha_{\mathrm{g},2}}{|d_{re}|^2}\Big) = n'r, \tag{6.44}$$

where $r = \frac{\Omega_1}{\Omega_2}$ and we have used the fact that $\Delta_g^{\mathrm{nr}} = -\frac{1}{4}\alpha_g|E_1|^2$ and $\Omega_1 = \frac{d_{eg}E_1}{\hbar}$. This equation can be solved for r given Δ_1 and a chosen Rydberg level. Once r and thus all intensity parameters are chosen, t_{gap} is chosen such that $\phi_{\mathrm{gap}} = 2\pi n$. Solutions occur at

$$t_{\mathrm{gap}} = \frac{n\pi}{\Big(\frac{|\Omega_{2,c}|^2}{4(\Delta_1)} + \Delta_{r1,c}^{\mathrm{nr}} + \Delta_{r2,c}^{\mathrm{nr}}\Big) - \Big(\frac{|\Omega_{1,c}|^2}{4(\Delta_1)} + \Delta_{g1,c}^{\mathrm{nr}} + \Delta_{g2,c}^{\mathrm{nr}}\Big)} - t_\pi, \tag{6.45}$$

for $t_\pi = \frac{\pi}{|\Omega_R|}$.

For example, starting with the parameters found in section 6.1.1, the single photon Rabi frequency ratio is equal to $r = 2.295$ which is just 0.27% off from a solution to equation (6.44). If r value is fine-tuned and then $t_{\mathrm{gap}} = 423$ ns the above conditions are met which recover the ideal C_Z. How accurately do we need to know these parameters and how sensitive are we to fluctuations? To answer this, the overlap fidelity with an ideal Bell state, $F = |\langle B_{ideal}|B_{\mathrm{Stark}}\rangle|^2$ is calculated as the parameters are varied from their optimum point. For example, Fig. 6.13 shows how the Bell state fidelity changes as t_{gap} is changed. This parameter will not fluctuate in time but the accuracy to which we can set it is around 50 ns, the rise/fall time of the switching AOMs. Fig. 6.14 plots the Bell state fidelity, $F = |\langle B_{ideal}|B_{\mathrm{Stark}}\rangle|^2$ as two parameters are varied. These plots demonstrate the accuracy at which we need to be able to measure and set these parameters and what sort of fluctuations we can withstand. Based on the measurements in section 6.1.1 and on our ability to stabilize long term fluctuations using a DC noise eater device (see section A.2), we can place an upper limit on the measurement accuracy and fluctuations around 2%. Based on the plots of Fig.6.14, 2% is tolerable.

6.5 Two qubit gate limitations and future improvements

As mentioned throughout this chapter, the main factor limiting our CNOT and entanglement fidelity is the apparent atom loss during the gate sequence. Specifically, the loss occurs on the control atom after the sequence of Rydberg pulses. As opposed to the target atom which executes

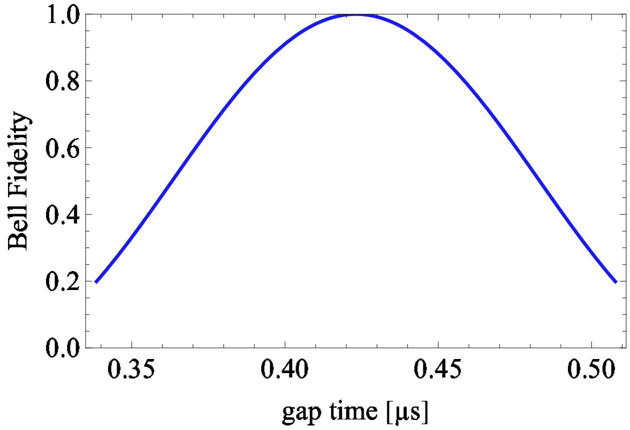

Figure 6.13: The Bell state fidelity, $F = |\langle B_{ideal}|B_{\mathrm{Stark}}\rangle|^2$, is plotted as a function of gap time, t_{gap}, using parameters which were found to give an ideal C_Z gate.

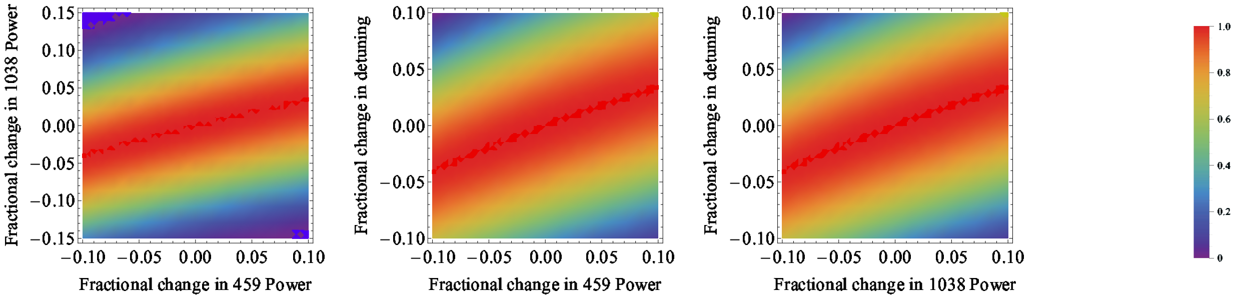

Figure 6.14: The Bell state fidelity, $F = |\langle B_{ideal}|B_{\mathrm{Stark}}\rangle|^2$, is plotted as a function of two different parameters. The center point of each plot uses the parameters which were found to give an ideal C_Z gate.

a 2π Rydberg rotation in one pulse, the control atom has some gap time in between Rydberg π rotations where the excitation beam is switched off, moved to the target site, then moved back to the control and switched back on for the final Rydberg π rotation. This gap time is equal to ~ 3 μs which is must shorter than the lifetime of the Rydberg state. Fig. 6.15 shows a series of experiments which demonstrate this loss on the control. State detection is turned off so both

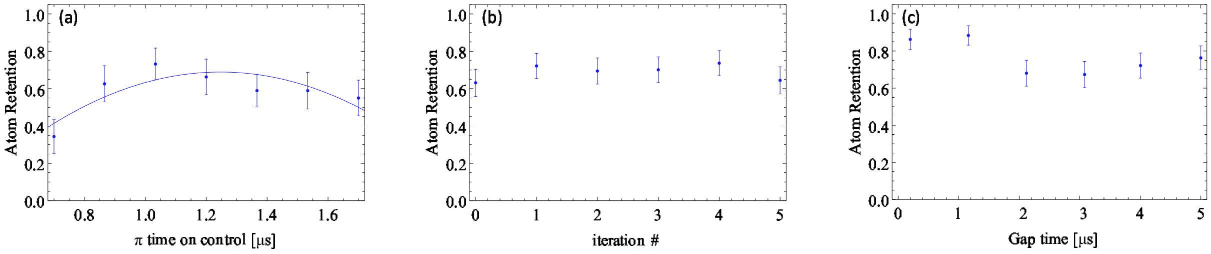

Figure 6.15: Some tests looking at the loss of the control atom after the Rydberg pulse sequence. No state detection is done so both ground states are measured. Parameters used: $\Omega_1 = 2\pi \times 70$ MHz, $\Omega_2 = 2\pi \times 31$ MHz, and $\Delta_1 = -2\pi \times 2.2$ GHz, $82s_{1/2}$. (a) To carefully tune in the proper timings, the π-pulse time is scanned while looking at the atom retention on the control. Here the target pulse is removed to minimize the gap time to 1 μs. The beams are still moved off of the control site during this gap time. Data from 2014_11_11_12_45_44. (b) The retention on the control after the full Rydberg pulse sequence with target pulse added making the gap time 3 μs. The same sequence is repeated six times. Data from 2014_11_11_13_25_33. (c) With the control pulse set to the best π time found in (a), the gap time is varied to show the loss as a function of time. Data from 2014_11_13_08_49_55.

$|f = 3\rangle$ and $|f = 4\rangle$ are measured. The cause of this loss is currently unknown. The large differential shift between the ground and the Rydberg states could be a problem due to finite atom temperatures, pointing stability issues, long term intensity drifts and the fact that our pulses are not perfectly square. All of these issues coupled with a large differential Stark shift could cause off-resonant rotations. One solution to this problem is to change the detuning, Δ_1. By changing the detuning to $\Delta_1 = 2\pi \times 0.8$ GHz by tuning the 918 nm laser over a cavity FSR, we can find some values for Ω_1 and Ω_2 that are easily reachable within our parameter space that give fast two photon Rabi frequencies and a very small ground-differential shift. For example, by halving the powers in each of the 1038 nm and 459 nm beams, we can achieve an Ω_R of 750 kHz with a differential Stark shift of 20 kHz. Note that at this detuning, the hyperfine structure of the intermediate level must be included for all calculations. This approach is currently being explored.

Other issues could be due to Rydberg interaction with stray electric fields. We are currently working on upgrading our vacuum cell to include electrodes for the purpose of cancelling any stray fields.

In addition, we will soon implement pulse shaping techniques to try and improve the two qubit gate[79].

Chapter 7

Future Outlook

In this thesis I have described how we have built an array of 49 single atom qubits and how we have used this array to perform single qubit and two qubit operations. Currently we are limited by our ability to do two qubit operations. Improving this is our most urgent short term goal. Despite this shortcoming we still have an array of 49 qubits on which we can perform high fidelity single qubit gates as well as two qubit entangling gates on nearest neighbors and beyond. Here I will describe some of this interesting things we can do with such a system moving forward.

7.1 Beyond two qubits

Having a universal set of gates means that any operation can be broken down and implemented by that set which in our case is composed of single qubit rotations and the CNOT gate. However, this procedure is not always the most efficient way to do the operation. For example, the Toffoli gate sometimes called the C_2NOT gate inverts a target bit conditional on two control bits. The Toffoli gate requires six CNOT gates if it is decomposed into CNOT gates and single qubit operations [62]. A useful feature of Rydberg blockade interaction is that a single control atom can simultaneously interact with many atoms that exist inside the "blockade radius". This can be used to implement more efficient C_kNOT gates [80]. In the reference, the authors proposed two distinct ways of implementing C_kNOT gates taking advantage of this feature of the blockade radius. In the sequentially addressed approach, which would be the most straight forward to implement in our array, Rydberg π-pulses are applied to the control atoms individually in order 1 to k. This is followed by a sequence of three π-pulses on the single target atom which swaps its state in the absence of blockade. Then the control qubits are returned to their original state using a series of

π-pulses in reverse order, k to 1. When in state $|0\rangle$ the first control qubit blocks the excitation of the remaining control qubits and prevents the state swap on the target. This means the target will only swap states if all control atoms are in the $|1\rangle$ state. This sequence is implemented in just $2k+3$ pulses. The other protocol calls for a simultaneous excitation of the controls into a non-interacting Rydberg level $|s\rangle$, following by the swapping on the target via a different Rydberg level $|r\rangle$ that is blockaded by any control that is in $|s\rangle$. Remarkably this procedure can be done with just five π-pulses independent of k.

A similar pulse sequence was proposed in reference [81] as an efficient way to execute a Grover search [82].

One can also imagine using a single control atom with k target atoms lying within the blockade radius. This would create a so called CNOT^k gate.

7.2 Dissipative entanglement

Recent proposals have suggested using long range Rydberg interactions together with dissipation to create high fidelity entangled states [83, 84]. The authors in [83] describe an optical pumping process with asymmetric Rydberg interactions where the dark state is the two atom Bell singlet state. They found that using the dissipative approach it is possible to prepare the Bell state with a fidelity greater than 0.998 using a Rydberg interaction 1500 times smaller than that needed for the coherent Rydberg blockade gate. This means that entanglement can be created at much larger distances and we can imagine entangling atoms across our array.

7.3 Quantum Error Correction

Quantum error correction (QEC) will most likely be a necessary tool of any implementation of fault-tolerant quantum computation [62]. By encoding information of one logical qubit onto many physical qubits certain errors can be detected and corrected without destroying the state thus protecting the quantum information. With our array of 49 physical qubits it will be possible to demonstrate operations on logical qubits. A three qubit error correcting code has been demonstrated in NMR [85], ions [86, 87], and superconductors [88] but the three qubit code only corrects for phase flip (Z-gate) or bit flip (X-gate) errors and not both simultaneously. More recently, a 9 qubit code was used to protect against bit flip errors [89], which is a step towards implementation of a surface code [90].

To protect against general one qubit errors a minimum of five qubits are needed [6]. The set of logical Clifford gates cannot be realized transversally with the five qubit code and for this reason many prefer the seven qubit Steane code [5].

To illustrate the power of error correction assume we have a system where each physical qubit experiences either a phase flip (Z error) and/or a bit flip (X error) independently with probability, p, per gate operation. Following the example presented in [91], assume we encode a logical qubit using the Steane code and logical gate operations can be performed fault tolerantly. A cycle of error correction is performed after every logical gate that will correct for a single error. If an error is introduced during a logical gate operation it will not propagate through out the code and will be corrected after an error correction cycle. With a single level of error correction, the error correction will fail if two errors occur during a logical gate operation. This happens with a failure rate

$$p_L^1 = cp^2, \tag{7.1}$$

for a constant c. Next we can add a second level of error correction by concatenating the same code. For example, if using the Steane code, seven physical qubits are encoded as one level-1 logical qubit. If we now take seven of these level-1 qubits[1] we can use them to encode a level-2 logical bit. Now the failure rate is equal to

$$p_L^2 = (p_L^1)^2 = c^3p^4. \tag{7.2}$$

One can iterate this concatenation process indefinitely for g times. The level-g logical qubit will be made up of 7^g physical qubits and protect against $\frac{3^g-1}{2}$ individual errors. The failure rate for a level-g encoded qubit is

$$p_L^g = (p_L^1)^g = \frac{(cp)^{2g}}{c}. \tag{7.3}$$

---

[1] Coincidentally this becomes 49 physical qubits!

If p is small enough such that $cp < 1$ the failure rate of a level-g encoded qubit can be made arbitrarily small and thus the error threshold is born:

$$p_{th} < 1/c. \tag{7.4}$$

This means any arbitrarily large quantum circuit can be successfully implemented to arbitrary accuracy once the physical error rate is below this threshold. We leave calculations of p_{th} to the theorists but many estimates put it between 10^{-4} and 10^{-6} [91]. These estimates depend heavily upon architectural considerations, assumed error models, geometric constraints, and the QEC code that is used.

This method of concatenation is straight forward in theory but in practice involves entangling a huge number (7^g) of qubits and the predicted error thresholds are difficult to achieve. The active field of QEC theory is constantly looking for new and better ways to protect qubits and increase the error threshold. Topological quantum computing encodes quantum information in global properties of many-particle systems in a way that provides protection against local noise sources [92]. Topological quantum computing promises predicted error thresholds as high as 1%. Topological color codes [93] are of particular interest as the logical Clifford gates are implemented transversally within them. The smallest instances of a 2D topological color code involves seven qubits which form a 2D triangular planar code structure of three plaquettes with one physical qubit placed at each vertex of the plaquettes. Such a code was recently demonstrated experimentally using a system of seven trapped ions [94]. Demonstration of a code such as this would be relatively straight forward in our 2D qubit array.

Bibliography

[1] D. A. Steck, *Cesium D Line Data*

[2] M. J. Piotrowicz *et al.*, *Two-dimensional lattice of blue-detuned atom traps using a projected gaussian beam array*, Phys. Rev. A **88**, 013420 (2013)

[3] P. W. Shor, *Polynomial-Time Algorithms for Prime Factorization and Discrete Logarithms on a Quantum Computer*, SIAM J. Comput. **26**, 1484 (1997)

[4] Peter W. Shor, *Scheme for reducing decoherence in quantum computer memory*, Phys. Rev. A **52**, R2493–R2496 (Oct 1995)

[5] A. M. Steane, *Error correcting codes in quantum theory*, Phys. Rev. Lett. **77**, 793–797 (Jul 1996)

[6] Raymond Laflamme, Cesar Miquel, Juan Pablo Paz, and Wojciech Hubert Zurek, *Perfect quantum error correcting code*, Phys. Rev. Lett. **77**, 198–201 (Jul 1996)

[7] D. P. DiVincenzo, *The Physical Implementation of Quantum Computation*, Fortschr. Phys. **48**, 771 (2000)

[8] R. Blatt and D. Wineland, *Entangled states of trapped atomic ions*, Nature **453**, 1008 (2008)

[9] John Clarke and Frank K. Wilhelm, *Superconducting quantum bits*, Nature **453**, 1031–1042 (June 2008)

[10] Daniel Loss and David P. DiVincenzo, *Quantum computation with quantum dots*, Phys. Rev. A **57**, 120–126 (Jan 1998)

[11] Jeremy L. O'Brien, *Optical quantum computing* **318**, 1567–1570 (2007)

[12] Markus Greiner *et al.*, *Quantum phase transition from a superfluid to a mott insulator in a gas of ultracold atoms* **415**, 39–44 (2007)

[13] W. S. Bakr, A. Peng, S. Folling, and M. Greiner, *A quantum gas microscope for detecting single atoms in a Hubbard-regime optical lattice*, Nature **462**, 74 (2009)

[14] Gavin K. Brennen, Carlton M. Caves, Poul S. Jessen, and Ivan H. Deutsch, *Quantum logic gates in optical lattices*, Phys. Rev. Lett. **82**, 1060–1063 (Feb 1999)

[15] D. Jaksch *et al.*, *Entanglement of atoms via cold controlled collisions*, Phys. Rev. Lett. **82**, 1975–1948 (1999)

[16] T. Pellizzari, S. A. Gardiner, J. I. Cirac, and P. Zoller, *Decoherence, continuous observation, and quantum computing: A cavity qed model*, Phys. Rev. Lett. **75**, 3788–3791 (Nov 1995)

[17] L. You and M. S. Chapman, *Quantum entanglement using trapped atomic spins*, Phys. Rev. A **62**, 052302 (Oct 2000)

[18] J. Mompart *et al.*, *Quantum computing with spatially delocalized qubits*, Phys. Rev. Lett. **90**, 147901 (Apr 2003)

[19] D. Jaksch *et al.*, *Fast Quantum Gates for Neutral Atoms*, Phys. Rev. Lett. **85**, 2208 (2000)

[20] W Happer, *Optical pumping*, Rev. Mod. Phys. **44**, 169–249 (Apr 1972)

[21] C. Deutsch *et al.*, *Spin self-rephasing and very long coherence times in a trapped atomic ensemble*, Phys. Rev. Lett. **105**, 020401 (Jul 2010)

[22] Thad G. Walker and Mark Saffman, *Entanglement of two atoms using rydberg blockade*, Adv. At. Mol. Opt. Phys. **61**

[23] T. A. Johnson *et al.*, *Rabi Oscillations between Ground and Rydberg States with Dipole-Dipole Atomic Interactions*, Phys. Rev. Lett. **100**, 113003 (2008)

[24] E. Urban *et al.*, *Observation of Rydberg blockade between two atoms*, Nature Phys. **5**, 110 (2009)

[25] A. Gaëtan *et al.*, *Observation of collective excitation of two individual atoms in the Rydberg blockade regime*, Nature Phys. **5**, 115 (2009)

[26] L. Isenhower *et al.*, *Demonstration of a Neutral Atom Controlled-NOT Quantum Gate*, Phys. Rev. Lett. **104**, 010503 (2010)

[27] X. L. Zhang *et al.*, *Deterministic entanglement of two neutral atoms via Rydberg blockade*, Phys. Rev. A **82**, 030306 (2010)

[28] T. Wilk *et al.*, *Entanglement of Two Individual Neutral Atoms Using Rydberg Blockade*, Phys. Rev. Lett. **104**, 010502 (2010)

[29] Y.-Y. Jau *et al.*, *Entangling Atomic Spins with a Strong Rydberg-Dressed Interaction* (2015), arXiv:1501.03862 [quant-ph]

[30] A. L. Migdall *et al.*, *First Observation of Magnetically Trapped Neutral Atoms*, Phys. Rev. Lett. **54**, 2596 (1985)

[31] Steven Chu, J. E. Bjorkholm, A. Ashkin, and A. Cable, *Experimental Observation of Optically Trapped Atoms*, Phys. Rev. Lett. **57**, 314 (1986)

[32] E. L. Raab *et al.*, *Trapping of Neutral Sodium Atoms with Radiation Pressure*, Phys. Rev. Lett. **59**, 2631 (1987)

[33] P. D. Lett *et al.*, *Optical molasses*, J. Opt. Soc. Am. B **6**, 2084 (1989)

[34] C. J. Foot, *Atomic Physics* (OUP, Oxford, 2005)

[35] H. J. Metcalf and P. van der Straten, *Laser Cooling and Trapping* (Springer-Verlag, 2002)

[36] C. S. Adams and E. Riis, *Laser Cooling and trapping of neutral atoms*, Prog. Quant. Electron. **21**, 1 (1997)

[37] S. J. M. Kuppens *et al.*, *Loading an optical dipole trap*, Phys. Rev. A **62**, 013406 (2000)

[38] K. Dieckmann, R. J. C. Spreeuw, M. Weidemüller, and J. T. M. Walraven, *Two-dimensional magneto-optical trap as a source of slow atoms*, Phys. Rev. A **58**, 3891 (1998)

[39] K. B. MacAdam, A. Steinbach, and C. Wieman, *A narrow-band tuneable diode laser system with grating feedback, and a saturated absorption spectrometer for CS and Rb*, Am. J. Phys. **60**, 1098–1100 (92)

[40] F. G. Major, V.N. Gheorghe, and G. Werth, *Charged particle traps: physics and techniques of charged particle field* (Springer, Berlin, 2005)

[41] R. Grimm, M. Weidemuller, and Y. B. Ovchinnikov, *Optical dipole trap for neutral atoms*, Adv. At. Mol. Opt. Phys. **42**, 170 (2000)

[42] J. D. Miller, R. A. Cline, and D. J. Heinzen, *Far-off-resonance optical trapping of atoms*, Phys. Rev. A **47**, R4567 (1993)

[43] S. Zhang, F. Robicheaux, and M. Saffman, *Magic-wavelength optical traps for Rydberg atoms*, Phys. Rev. A **84**, 043408 (2011)

[44] N. Schlosser, G. Reymond, and P. Grangier, *Collisional Blockade in Microscopic Optical Dipole Traps*, Phys. Rev. Lett. **89**, 023005 (2002)

[45] T. Grünzweig, M. Hilliard, M. McGovern, and M.F. Andersen, *Near-deterministic preparation of a single atom in an optical microtrap*, Nature Phys. **6**, 951 (2010)

[46] R. Dumke *et al.*, *Micro-optical Realization of Arrays of Selectively Addressable Dipole Traps: A Scalable Configuration for Quantum Computation with Atomic Qubits*, J. Opt. Soc. Am. B **89**, 1889 (2002)

[47] Silvia Bergamini *et al.*, *Holographic generation of microtrap arrays for single atoms by use of a programmable phase modulator*, Phys. Rev. Lett. **21**, 097903 (2004)

[48] C. Knoernschild *et al.*, *Independent individual addressing of multiple neutral atom qubits with a micromirror-based beam steering system*, Applied Physics Letters **97**, 134101 (2010)

[49] P. S. Jessen and I. H. Deutsch, *Optical Lattices*, Adv. Atom. Mol. Opt. Phys. **37**, 95 (1996)

[50] P. A. Franken, A. E. Hill, C. W. Peters, and G. Weinreich, *Generation of Optical Harmonics*, Phys. Rev. Lett. **7**, 118 (1961)

[51] J. Dalibard and C. Cohen-Tannoudji, *Laser cooling below the Doppler limit by polarisation gradients: simple theoretical models*, J. Opt. Soc. Am. B **6**, 2023 (1989)

[52] D. D. Yavuz *et al.*, *Fast ground state manipulation of neutral atoms in microscopic optical traps*, Phys. Rev. Lett. **96**, 063001 (2006)

[53] T. Xia *et al.*, *Randomized benchmarking of single-qubit gates in a 2d array of neutral-atom qubits*, Phys. Rev. Lett. **114**, 100503 (Mar 2015), `http://link.aps.org/doi/10.1103/PhysRevLett.114.100503`

[54] D. Schrader *et al.*, *Neutral atom quantum register*, Phys. Rev. Lett. **93**, 150501 (2004)

[55] C. D. Wallace *et al.*, *Measurements of temperature and spring constant in a magneto-optical trap*, J. Opt. Soc. Am. B **11**, 703 (1994)

[56] A.V. Carpentier *et al.*, *Preparation of a single atom in an opticalmicrotrap*, Laser Physics Letters **10**, 125501 (2013), `http://stacks.iop.org/1612-202X/10/i=12/a=125501`

[57] C. Tuchendler *et al.*, *Energy distribution and cooling of a single atom in an optical tweezer*, Phys. Rev. A **78**, 033425 (2008)

[58] S. Friebel *et al.*, *CO_2-laser optical lattice with cold rubidium atoms*, Phys. Rev. A **57**, R20 (1998)

[59] A. G. Radnaev *et al.*, *A quantum memory with telecom-wavelength conversion*, Nature Physics **6**, 894–899 (2010)

[60] A. W. Carr and M. Saffman, *Doubly magic trapping for Cs atom hyperfine clock transitions* (2014), arXiv:1406.3560 [atom-ph]

[61] C. Zhang, S. L. Rolston, and S. Das Sarma, *Manipulation of single neutral atoms in optical lattices*, Phys. Rev. A **74**, 042316 (2006)

[62] M. A. Nielsen and I. L. Chuang, *Quantum Computation and Quantum Information* (CUP, Cambridge, 2005)

[63] E. Iskrenova-Tchoukovaa, M.S. Safronovaa, and U.I. Safronovab, *High-precision study of cs polarizabilities*, Journal of Computational Methods in Sciences and Engineering **7**

[64] S Kuhr *et al.*, *Analysis of dephasing mechanisms in a standing-wave dipole trap*, Phys. Rev. A **72** (2005)

[65] E Knill, R Laflamme, and W Zurek, *Accuracy threshold for quantum computation*, arXiv:9610011v3 [quant-ph]

[66] E. Knill *et al.*, *Randomized benchmarking of quantum gates*, Phys. Rev. A **77**, 012307 (2008)

[67] R. Freeman, *Spin Choreography* (Oxford University Press, 1997)

[68] S Wimperis, *Broadband, Narrowband, and Passband Composite Pulses for Use in Advanced NMR Experiments*, J. Magn. Reson., Ser. B **109**, 221–231 (1994)

[69] K Brown, A Harrow, and Chuang I, *Arbitrarily accurate composite pulse sequences*, Phys. Rev. A **70**, 052318 (2004)

[70] H.K. Cummins, G. Llewellyn, and J.A. Jones, *Tackling systematic errors in quantum logic gates with composite rotations*, Phys. Rev. A **67**, 042308 (2003)

[71] A. M. Hankin *et al.*, *Two-atom rydberg blockade using direct 6s to np excitation*, Phys. Rev. A **89**, 033416 (2014)

[72] T Manthey *et al.*, *Scanning electron microscopy of rydberg-excited boseeinstein condensates*, New Journal of Physics **16**, 083034

[73] C. Cohen-Tannoudji, J. Dupont-Roc, and G. Grynberg, *Atom-Photon Interactions* (Wiley-Interscience, New York, 1998)

[74] E Brion, L H Pedersen, and K Mølmer, *Adiabatic elimination in a lambda system*, J. Phys. A: Math. Theor. **40**

[75] K.-H. Weber and Craig J. Sansonetti, *Accurate energies of nS , nP , nD , nF , and nG levels of neutral cesium*, Phys. Rev. A **35**, 4650–4660 (Jun 1987), `http://link.aps.org/doi/10.1103/PhysRevA.35.4650`

[76] Eric D. Black, *An introduction to Pound–Drever–Hall laser frequency stabilization*, Am. J. Phys. **69**, 79–87 (2001)

[77] C. J. Lorenzen and K. Niemax, *Precise quantum defects of nS, nP and nD Levels in Cs I*, Z. Phys. A **315**, 127 (1984), `http://dx.doi.org/10.1007/BF01419370`

[78] T. G. Walker and M. Saffman, *Consequences of Zeeman degeneracy for the van der Waals blockade between Rydberg atoms*, Phys. Rev. A **77**, 032723 (2008)

[79] M. Saffman and F.K. Wilhelm, unpublished

[80] L. Isenhower, M. Saffman, and K. Mølmer, *Multibit cknot quantum gates via rydberg blockade*, Quant. Inf. Proc. **10**, 755 (2011)

[81] K. Mølmer, L. Isenhower, and M. Saffman, *Efficient grover search with rydberg blockade*, J. Phys. B: At. Mol. Opt. Phys. **44**, 184016 (2011)

[82] L. K. Grover, *Quantum Mechanics Helps in Searching for a Needle in a Haystack*, Phys. Rev. Lett. **79**, 325 (1997)

[83] A. W. Carr and M. Saffman, *Preparation of entangled and antiferromagnetic states by dissipative rydberg pumping*, Phys. Rev. Lett. **111**, 033607 (2013)

[84] D. D. Bhaktavatsala Rao and Klaus Mølmer, *Dark entangled steady states of interacting rydberg atoms*, Phys. Rev. Lett. **111**, 033606 (2013)

[85] D. G. Cory *et al.*, *Experimental quantum error correction*, Phys. Rev. Lett. **81**, 2152 (1998)

[86] J. Chiaverini1 *et al.*, *Realization of quantum error correction*, Nature **432**, 602–605 (2004)

[87] Philipp Schindler *et al.*, *Experimental repetitive quantum error correction* **332**, 1059–1061 (2011)

[88] M. D. Reed *et al.*, *Realization of three-qubit quantum error correction with superconducting circuits*, Nature **482**, 382385 (2012)

[89] J. Kelly *et al.*, *State preservation by repetitive error detection in a superconducting quantum circuit*, Nature **519**, 66–69 (2015)

[90] Austin G. Fowler, Matteo Mariantoni, John M. Martinis, and Andrew N. Cleland, *Surface codes: Towards practical large-scale quantum computation*, Phys. Rev. A **86**, 032324 (Sep 2012), `http://link.aps.org/doi/10.1103/PhysRevA.86.032324`

[91]

[92] *Fault-tolerant quantum computation by anyons*, Annals of Physics **303**, 2 – 30 (2003), ISSN 0003-4916

[93] H. Bombin and M. A. Martin-Delgado, *Topological quantum distillation*, Phys. Rev. Lett. **97**, 180501 (2006)

[94] D. Nigg *et al.*, *Quantum computations on a topologically encoded qubit*, Science **345**, 302–305 (2014)

[95] T. A. Savard, K. M. O'Hara, and J. E. Thomas, *Laser-noise-induced heating in far-off resonance optical traps*, Phys. Rev. A **56**, R1095–R1098 (1997)

DISCARD THIS PAGE

Appendix A: Laser Noise

Characterizing the noise of the lasers in our experiment is critical to understanding our error sources so we can work to improve them. Fast fluctuations in the intensity leads to decoherence and possibly heating of the atoms. Slow intensity drifts lead to systematic errors due to miscalibrations.

A.1 Fast Noise

Power fluctuations within a fixed geometry are characterized by the relative intensity noise (RIN) value which is defined by

$$\mathrm{RIN} = \frac{\sqrt{\langle(\delta I)^2\rangle}}{\langle I\rangle} = \frac{\sqrt{\langle(\delta P)^2\rangle}}{\langle P\rangle}(\sqrt{\mathrm{Hz}})^{-1}. \tag{A.1}$$

$\langle(\delta P)^2\rangle$ is the mean square fluctuation of the power per unit bandwidth. The RIN level can be expressed in dB by using the definition

$$\mathrm{RIN}_{\mathrm{dB}} = 10\log(\mathrm{RIN})(\sqrt{\mathrm{Hz}})^{-1}. \tag{A.2}$$

The power fluctuations from a laser beam are measured on a photodetector which outputs a current, J, proportional to the optical power such that we measure

$$\mathrm{RIN}_{J,\mathrm{dB}} = 10\log(\mathrm{RIN}_J)(\sqrt{\mathrm{Hz}})^{-1}. \tag{A.3}$$

The ultimate goal is to reduce the RIN to the fundamental limiting level set by shot noise. For a current J the RMS shot noise current in a bandwidth Δf is

$$\tilde{\sigma}_J = \sqrt{2eJ\Delta f}(\mathrm{A}/\sqrt{\mathrm{Hz}}), \tag{A.4}$$

where e is the electronic charge. The RMS noise densities per $\sqrt{\mathrm{Hz}}$ are

$$\sigma_{J,\mathrm{sn}} = \sqrt{2eJ}(\mathrm{A}/\sqrt{\mathrm{Hz}}), \tag{A.5}$$

and so the shot noise RIN is equal to

$$\mathrm{RIN}_{\mathrm{sn}} = \sqrt{\frac{2e}{J}}. \tag{A.6}$$

Inserting the numerical values for e and converting to dB, the shot noise is expressed as

$$\mathrm{RIN}_{\mathrm{sn,dB}} = -77.5 - 5\log\left(J_{\mathrm{mA}}\right)(\mathrm{dB}/\sqrt{\mathrm{Hz}}). \tag{A.7}$$

Reducing the noise down to the shot noise limit is technically challenging. What is a more realistic goal? We can estimate the accuracy of a rotation due to a Rabi oscillation with a laser assuming a certain RIN value. The Rabi pulse causes a rotation $\theta = \Omega_0 I t$ where Ω_0 is a constant and I is the laser intensity with a pulse time t. Adding in some laser power fluctuations, $I = I_0 + \delta I$, then

$$\theta = \theta_0 + \Omega_0 \int_0^t dt' \delta I(t'), \tag{A.8}$$

for $\theta_0 = \Omega_0 I_0 t$. The relative RMS error in the pulse area is

$$\frac{\sqrt{\langle(\delta\theta)^2\rangle}}{\langle\theta\rangle} = \frac{\sqrt{\langle(\delta\theta)^2\rangle}}{\theta_0}, \tag{A.9}$$

with

$$(\delta\theta)^2 = \Omega_0^2 \int_0^t dt' \delta I(t') \int_0^t \delta t'' \delta I(t''). \tag{A.10}$$

The pulse area is sensitive to intensity noise with a bandwidth $1/t$ and

$$\frac{\sqrt{\langle(\delta\theta)^2\rangle}}{\theta_0} = \frac{\langle\mathrm{RIN}\rangle}{\sqrt{t}}. \tag{A.11}$$

$\langle\mathrm{RIN}\rangle$ is the RIN level averaged over the bandwidth $1/t$. For example, if we want the relative RMS error to be 0.1% then we would require

$$\langle\mathrm{RIN}\rangle = 0.001\sqrt{t}. \tag{A.12}$$

Then taking $t = 1\ \mu$s gives

$$\langle\mathrm{RIN}\rangle = 10^{-6}\sqrt{\mathrm{Hz}}, \tag{A.13}$$

or -60 $\mathrm{dB}\ \sqrt{\mathrm{Hz}}$ at frequencies below 1 MHz. This roughly gives us a goal to shoot for.

To measure the laser RIN, a beam is aligned to a photodetector (PD)[1] that is 50 Ω terminated. The signal is sent through a DC block[2] to a dynamic signal analyzer[3] with an additional BNC T-connector which is connected to a digital voltmeter used for measuring the DC value of the signal.

---

[1] e.g. Thorlabs PDA100A, 0 gain

[2] Minicircuits BLK-89

[3] Stanford Research SRS785

This set up allows for the signal analyzer's sensitivity to be sufficient for measuring shot noise levels. The shot noise limit at a given DC value can be measured by shining a flashlight directly onto the PD, matching the DC value that is measured with the laser signal. Measurements on the signal analyzer are made with the input scaling set to -50 dB $\mathrm{V_{pk}}$, in power spectrum mode with units of $\mathrm{dBV_{rms}}/\sqrt{(\mathrm{Hz})}$, taking 100 RMS averages. To convert the signal taken from the analyzer into $\mathrm{RIN_{dB}}$ calculate

$$\mathrm{RIN_{dB}} = 0.5 \times \mathrm{dB}(V_{\mathrm{rms}}/\sqrt{\mathrm{Hz}}) - 10\log_{10}(V_{\mathrm{dc}}), \tag{A.14}$$

where $\mathrm{dB}(V_{\mathrm{rms}}/\sqrt{\mathrm{Hz}})$ is the measured signal and V_{dc} is the DC value taken from the digital voltmeter. To calculate the shot noise given a V_{dc} measurement, the gain of the PD must be known. For example, for the measurements below a Thorlabs PDA100A with a gain setting of 0 was used. Consulting the PDA100A manual gives a gain, G = 750V/A, for a 50 Ω terminated PD set to 0 gain. Then the shot noise is calculated as

$$\mathrm{RIN_{sn}}(V_{\mathrm{dc}}, G) = 10 \times \log_{10}(\sqrt{2e/(V_{\mathrm{dc}}/G)}). \tag{A.15}$$

A.1.1 Rydberg A measurements

The Rydberg A laser is measured in various locations along the laser path in order to diagnose the source of the noise. Referring to Figs. 5.3 and 5.5 the PD is placed right before the TA in order to measure the master laser alone, right after the TA, and after the SHG cavity.

From Fig. A.1 it is clear that the SHG adds the most noise. This could be mediated by better lock electronics, better piezo drivers driving the piezo in the SHG cavity, or better fast intensity noise stabilization. There is currently a noise eater system in place as shown in Fig. A.2. A separate PD[4] sees a fraction of the SHG light which is picked off from the main beam path with a window. The signal from this PD is sent to an analog noise eater electronics box which outputs a voltage to a voltage controlled attenuator (VCA) depending on the signal. The VCA in turn modulates the RF power that is sent to an AOM which modulates the diffraction efficiency of the AOM and thus the intensity in the main beam. The data in Fig. A.1 is taken with this feedback loop on. Currently the noise eater only works at low frequencies and only eats noise by a couple dB. Improving this

---

[4] Thorlabs PDA36A, gain 40

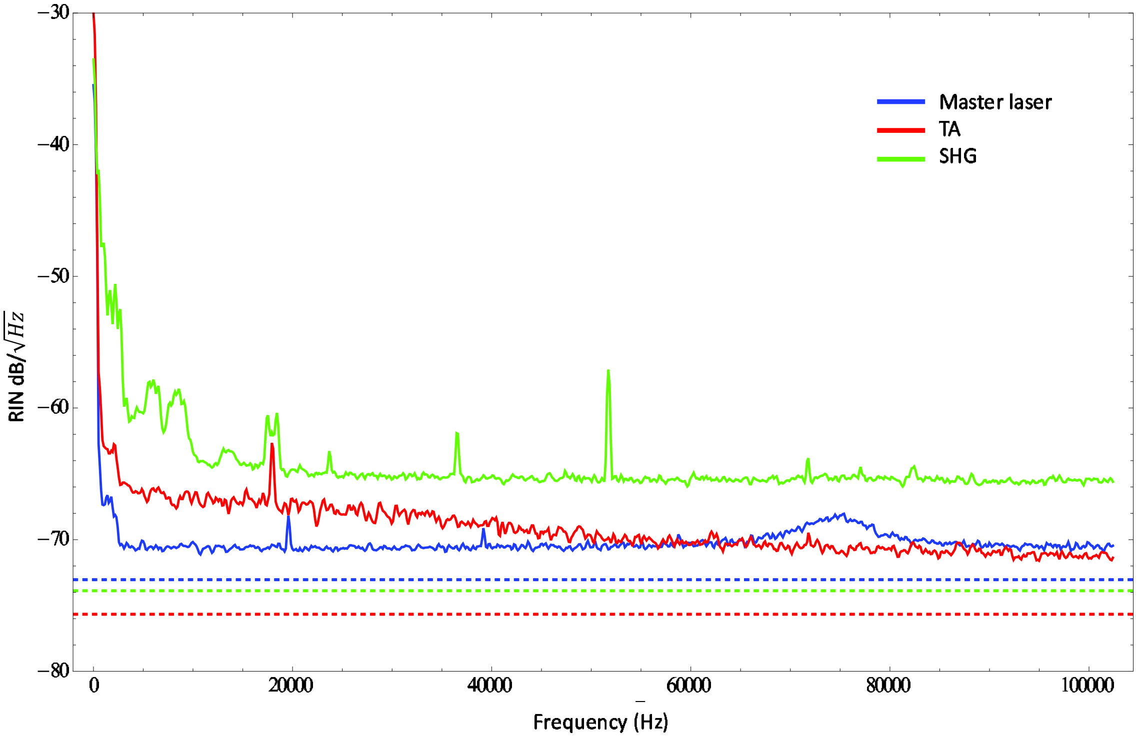

Figure A.1: RIN for various locations in the Rydberg A laser. The master laser noise spectrum is measured with a PD located before the TA. The DC value is 97.5 mV. The TA noise spectrum is measured right after the TA and had a DC values of 327 mV. The SHG spectrum which is the final light that is sent to the experiment was measured before the fiber with a DC value of 144 mV. Shot noise RIN is calculated and plotted as the dashed lines for the respective signals.

noise eating system with a quieter PD as well as new and improved feedback electronics is an on going process and will be essential to improving the experiment moving forward.

A.1.2 1038 nm Laser

Similar measurements are done for the 1038 nm laser as seen in Fig. A.3. The 1038 nm laser is considerably quieter than the Rydberg A laser. A system identical as that of Fig. A.2 is used to stabilize the 1038 nm noise.

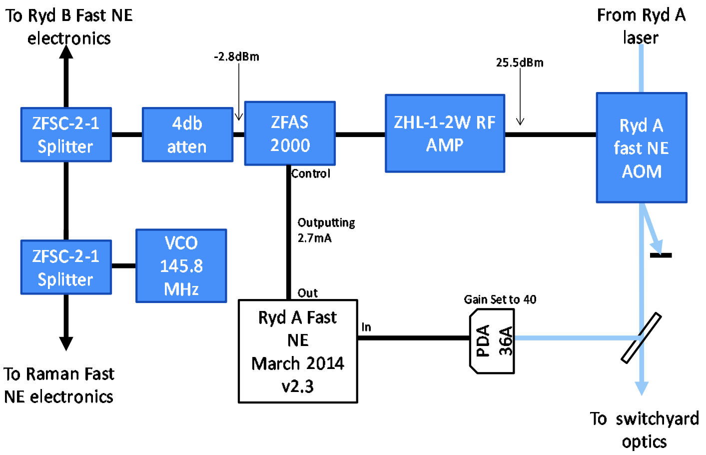

Figure A.2: Schematic for the electronic system used to stabilize fast intensity noise of the Rydberg A laser. RF components are all from Mini-circuits.

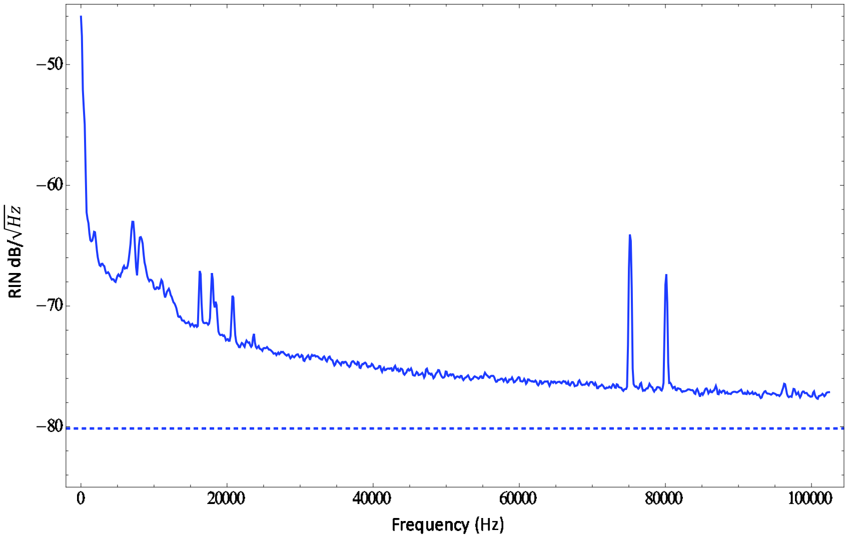

Figure A.3: RIN measurement for 1038 nm laser after the TA. Dashed line is the calculated shot noise for the DC value 2.65 V, G = 750 V/A.

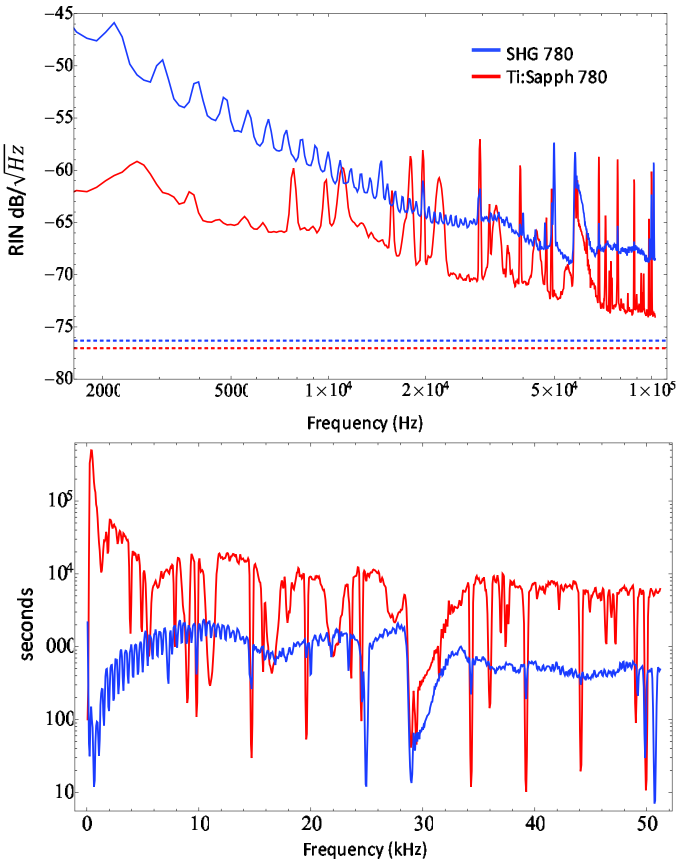

Figure A.4: (top) RIN measurement for each of the 780 nm trapping lasers with the dashed lines representing the calculated shot noise for the DC value 0.615 V and 0.441 V, G = 750 V/A. (bottom) From the RIN, heating rates in the trap due to parametric heating at twice the trap frequency and thus lifetimes can be calculated. Recall from Chapter 3 the measured trap frequencies of 9 kHz and 45 kHz.

A.1.3 780 nm Trap Lasers

The 780 nm trapping lasers are also measured individually on a PD placed after the hexagonal cell. The trapping lasers are less critical than the qubit control lasers but could still cause some dephasing or heating. A simple calculation converts the intensity noise into a heating rate in the trap due to parametric heating at twice the trap frequency[95]. The RIN along with the 1/e lifetime due to trap heating are shown in Fig. A.4. Our measurements of the trap lifetime are less than 10 s. Currently there is no intensity stabilization in place for the 780 nm systems.

A.2 Slow Noise

Slow noise amounts to long term drifts of the laser intensity. This is often caused by polarization drifts due to either improper input polarization to the fiber or some stress (stretching, heating) on the fiber. These polarization drifts translate into intensity drifts when there is a polarizer after the fiber. Because of the slow nature of the drifts, they manifest as systematic errors in the experiment. For example, say the intensity of the Rydberg A laser drifts by a fraction, ϵ, such that $I_{459} = I^0_{459}(1 + \epsilon)$. This will change the two photon Rabi frequency by an amount, $\Omega_{\mathrm{Ryd}} = \Omega^0_{\mathrm{Ryd}}\sqrt{1+\epsilon}$ which will show up as a rotation error. In addition, the change in intensity will also change the Stark shift by a factor of $(1 + \epsilon)$ which introduces a detuning error.

One can alleviate such errors by recalibrating the experiment on the time scale of the drifts or by employing composite pulse techniques described in Chapter 4. A better strategy is to minimize the error at the source then use feedback stabilization techniques similar to those described in the previous section but on a slower time scale. To do this a PD[5] is placed for each of the stabilized laser beams on the back of a mirror that is as close to the Hex cell as possible. This bare PD signal is sent to a DC noise eater (DCNE) electronics box[6]. At the end of every measurement in an experiment cycle, the light is switched on for a few ms. The DCNE reads the signal from the PD and outputs a voltage to a VCA which changes the RF power at an AOM with the goal of keeping the input signal at some set point. Electronic schematics of the slow noise eating system can be seen in Fig. A.5 for the 459 nm system which is similar to the 1038 nm system.

Fig. A.6 shows measurements of the Rydberg A light over 1000 measurements which corresponds to about 15 minutes. Each measurement is integrated for 450 μs. This data looks at a separate PD placed right after the fiber. The two data sets in this figure show before and after a shorter fiber with a more direct path to the experiment was installed. More drifts were seen when using a longer fiber. The longer fiber was taking a less direct path to the experiment which involved going up by the ceiling next to the lights and air conditioning system. We believe temperature gradients on the fiber might have caused polarization drifts. Switching to a shorter fiber that went straight across the room at table height seems to have alleviated this issue.

---

[5] Thorlabs SM1 PD1B

[6] Details of the design and operation of the DCNE can be found is the thesis of Alex Gill

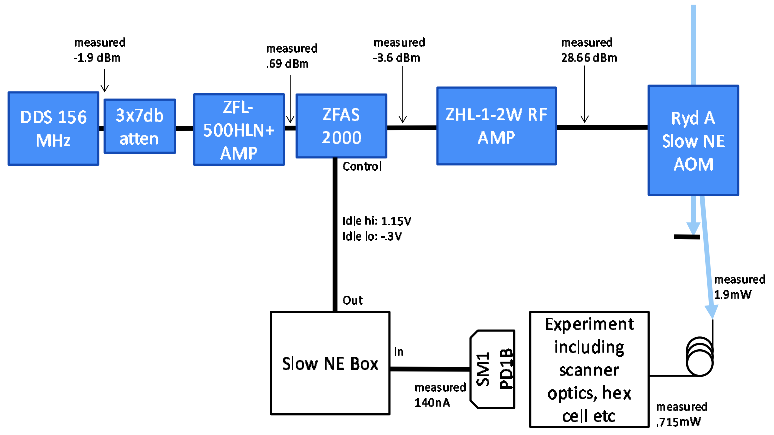

Figure A.5: Schematic for the electronic system used to stabilize slow intensity drifts of the Rydberg A laser. See appendix A for measurements.

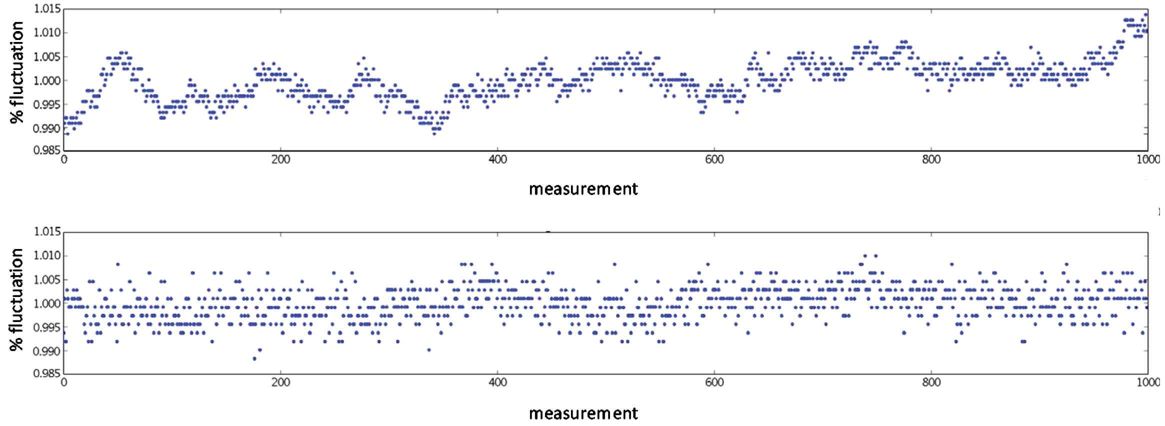

Figure A.6: (top) Long term stability (∼ 15 minutes) of Rydberg A laser looking right after the fiber, before a shorter fiber was installed. (bottom) Long term stability of Rydberg A laser looking right after the fiber after a shorter fiber was installed that had a more direct path to the experiment. The slow noise feedback is not on for there measurements, they these measurements demonstrate the type of drifts that need correcting.

Appendix B: Alignment to the Hex Cell

Alignment to the Hexagonal cell through the JenOptik lenses is difficult. The JenOptik lenses do not work well off-axis so the beams should be both centered and normal to the lenses which should be centered and normal with the Hex cell. This is complicated by the fact that the Hex cell is slightly tilted. This means all of the beams need to be slightly tilted as well. The following is an alignment procedure for lenses to the Hex cell. It is probably not the most optimal but it has been tested and it works. The 780 nm trap light is used as the primary light. All other light is aligned to this. All light should be aligned to their respective optics and then well centered in the cage leading up to the periscopes on either side.

1. Remove the broadband mirror on top of the periscope on the 459 side from its mount, allowing the 780 beam to pass through the mount, hitting the paper target set up on the other side. Move the paper target so that the beam is centered on it.

2. Remove both JenOptik lenses.

3. Place the one inch cage target so that is hanging on the top periscope mount on the 780 side. The back reflection from the cell should be visible on the target (using an IR viewer or Sony CCD). Use the top mirror to align the back reflection onto the incoming beam.

4. Use the hexagonal cell paper target to align the position of the beam, steering it to the center of the hex cell using the bottom periscope mirror.

5. Iterate between steps 3 and 4 until the beam is both centered on the Hex cell and its back reflection is aligned to itself. This should ensure the correct position and angle of the incoming beam with respect to the cell. The beam should not be running parallel to the table as the cell is tilted.

6. Reposition the target from step 1 so that it is centered on the beam. The lenses should not changed the position of the beam when they are positioned properly. Make sure the target is fixed and does not move for the remainder of the alignment.

7. Add on first JenOptik lens on 780 side.

   a) Eyeball its position in Z–the last surface of the lens should be 1.2 mm from the Hex cell.

   b) Use the target location to position the beam using the x and y actuators of the lens mount. The beam will be extremely big at this point but the center should be clear.

   c) Using a similar set up as step 3, align the back reflection to get the angle of the lens right, using the angle actuators.

   d) Iterate between b) and c) until angle and position are correct.

8. Add on second JenOptik on 459 side and repeat step 7 moving the second lens to get the correct position and angle.

9. Replace the top periscope mirror and align periscope so that the 780 beam is centered in the cage on the 459 side. The 780 trap array should image beautifully in the next imaging plane which is after the 300 mm lens. Now all other beams can be aligned to the 780 nm light and should be center and normal to the lenses and the cell.